Spring 1-1-2013

Physical Modeling of Coupled Water and Heat Flow Within a Borehole Heat Exchanger Array in the Vadose Zone

Krin Thierry Ousmane Traore
University of Colorado at Boulder, thierry.traore@colorado.edu

PHYSICAL MODELING OF COUPLED WATER AND HEAT FLOW WITHIN A BOREHOLE HEAT EXCHANGER ARRAY IN THE VADOSE ZONE

by

Krin Thierry Ousmane Traore

B.S., University of Colorado at Boulder

A thesis submitted to the

Faculty of the Graduate School of the

University of Colorado in partial fulfillment

of the requirement for the degree of

Master of Science

Department of Civil, Environmental, and Architectural Engineering

2013

This thesis entitled:

Physical Modeling of Coupled Water and Heat Flow

within a Borehole Heat Exchanger Array in the Vadose Zone

written by Krin Thierry Ousmane Traore

has been approved by the Department of Civil, Environmental, and Architectural Engineering

_____

Professor John McCartney (committee chair)

_____

Professor Kathleen Smits

_____

Professor Dobroslav Znidarčić

Date_____

The final copy of this thesis has been examined by the signatories, and we

find that both the content and the form meet the acceptable presentation standards

of scholarly work in the above mentioned discipline.

Krin Thierry Ousmane Traore (M.S. Civil Engineering, Department of Civil, Environmental, and Architectural Engineering)

Physical Modeling of Coupled Water and Heat Flow within a Borehole Heat Exchanger Array in the Vadose Zone

Thesis directed by Professor John S. McCartney

ABSTRACT

This thesis is focused on characterization of the heat transfer and water flow processes in a physical model of a borehole array in an unsaturated soil layer. The overall goal is to develop a dataset for validation of coupled thermo-hydraulic flow models used for simulating the efficiency of heat injection or extraction from soil-borehole thermal energy storage systems. The physical model consists of a layer of unsaturated silt compacted atop a layer of sand within an insulated, 0.53 m-tall, 0.6 m-diameter cylindrical tank. A water table was imposed at the top of the sand layer. Three steel "U"-tube pipes were inserted through the silt layer into the top of the sand layer to represent a triangular array of geothermal borehole heat exchangers, and several tests were performed with different heat exchanger spacings. Heated fluid was circulated through the steel pipes to inject heat into the unsaturated silt layer at a constant rate, during which time changes in volumetric water content and temperature were measured at different depths along the center of the silt layer using dielectric sensors. The thermal conductivity and specific heat of the silt were also monitored using a thermal probe at the center of the soil layer at mid-height. The temperature of the silt at different distances from the heat exchangers, the inlet and outlet temperatures of the fluid, as well as the temperature and relative humidity of the air at the soil surface were monitored.

Regardless of the heat exchanger spacing, the temperature of the unsaturated silt layer was observed to increase to a relatively steady-state value after a short period of time. Dielectric sensor

measurements initially show an increase in water content at all depths in the soil, indicating that that water is moving away from the heat exchangers, albeit at a slower rate than the heat flow process. Further, water was observed to condense at the soil surface, indicating that water vapor moved upward though the soil layer due to buoyancy. In the test with the smallest radial heat exchanger spacing of 80 mm, after the initial increase in water content, a sharp decrease in water content was observed. This indicates that water was driven from the center of the array into the surrounding soil, and that a convective cycle of water phase change did not occur for this small heat exchanger spacing. In the test with the greatest radial heat exchanger spacing of 300 mm, the soil in the center of the array did not experience a decrease in water content after the initial increase, which may indicate that a convective cycle was formed. In the case of the test with an intermediate heat exchanger spacing of 160 mm, an intermediate behavior was observed. In the tests, downward liquid water flow due to gravity could not be confirmed through evaluation of the water content data. This phenomenon, which is expected if a convective cycle of water phase change is observed in the array, may have been observed for longer testing times.

The thermal conductivity measured using the thermal probe was observed to increase significantly during the heating process, and was observed to be a function of both the degree of saturation of the soil and the temperature. In the case of the smallest radial borehole heat exchanger spacing, the thermal conductivity of the soil inside of the array was observed to decrease as the water content decreased, while the thermal conductivity outside of the heat exchanger array was observed to increase with increasing radial location. This confirms that the borehole spacing can have an important effect on the long-term heat storage in the vadose zone, and that small spacings may lead to an increase in thermal energy transfer to the soil outside of the array. In the case of the largest radial borehole heat exchanger spacing, a stable increase in thermal conductivity of the

soil within the array was observed. As expected, the heat storage in the unsaturated soil within the array increased with the spacing of the heat exchangers. However, the increase in water content in the array with the widest spacing also likely contributed to the increase in heat storage. A recommendation from this study is to use a geotechnical centrifuge to better simulate the role of capillary rise and downward liquid water flow on the coupled heat transfer and water flow process within a small-scale physical model. These features may be critical in establishing a convective cycle, which may enhance the efficiency of heat injection into a soil-borehole thermal energy storage system.

ACKNOWLEDGEMENT

Foremost, I would like to express my sincere gratitude to my advisor Professor John Scott McCartney for the continuous support of my Master's study and research, for his patience, motivation, enthusiasm, and immense knowledge. His guidance helped me in my research, analysis and writing of this thesis. I could not have imagined having a better advisor and mentor. Special thanks to Professors Kathleen Smits and Dobroslav Znidarčić for serving as part of my committee. Immense thanks to my colleague research student Tuğçe Baser for her fervent help both in preparing tests and discussing results leading to the completion of this project even during weekends and sleepless nights. Thanks to Woongju Mun for helping set up experimental equipment and for his help in preparing tests. Additional thanks to the geotechnical engineering students that worked with me and made learning fun and meaningful, especially, Ashkaan Hushmand, Zana Karimi, Theodore Deere, Cyrus Hoda, and everyone else from the department not mentioned.

Last but not least; I would like to thank my family: my parents Aoua and Lorcendy Traore, without whom I could not dream of getting this far, my sisters Emma Zohner and Appoline Traore and my brother in law Adam Zohner, and the big Zohner family for always unconditionally supporting in every way possible.

Funding provided by NSF grant 1230237 is much appreciated.

Table of Contents

ABSTRACT iii
ACKNOWLEDGEMENT vi
Table of Contents vii
List of Figures x
1. INTRODUCTION 1
1.1 Motivation 1
1.2 Problem Statement 1
1.3 Hypothesis 3
1.4 Objective and Approach 9
1.5 Scope 10
2. THEORETICAL BACKGROUND 11
2.1 History 11
2.2 Water Flow in Unsaturated Soils 12
2.2.1 Hydraulic Potential in Unsaturated Soils 12
2.2.2 Hydraulic Characteristics of Unsaturated Soils 13
2.3 Heat Transfer in Soils 20
2.3.1 Conductive Heat Transfer 21
2.3.2 Convective Heat Transfer 22
2.4 Coupled Heat and Water Flow 23
2.4.1 Water Flow due to Temperature Gradients 23
2.4.2 Heat Transfer with Water Flow 26
3. LITERATURE REVIEW 30
3.1 Variables Affecting the Thermal Properties of Unsaturated Soils 30
3.1.1 Temperature Effects 30
3.1.2 Combined Effects of Saturation and Temperature 32
3.2 Convective Cells in Unsaturated Soils 34
4. MATERIALS 36
4.1 Nevada Sand 36
4.2 Bonny Silt 36

4.2.1 Particle Size Distribution 37
4.2.2 Atterberg Limits 38
4.2.3 Specific Gravity 38
4.2.4 Compaction Characteristics 38
4.2.5 Hydraulic Conductivity and Soil-Water Retention Curve 39
4.2.6 Thermal Conductivity 40
5. EXPERIMENTAL SETUP 42
5.1 Overview 42
5.2 Temperature Probes 44
5.3 Temperature Control System 46
5.4 Instrumentation 50
5.4.1 Closed-Loop Heat Exchangers 50
5.4.2 Dielectric Sensors (Volumetric Water Content and Temperature) 51
5.4.3 Thermal Conductivity Sensor 52
5.4.4 Mariotte Bottle 55
6. PROCEDURES 57
6.1 Soil Placement Conditions 57
6.1.1 Preparation of the Physical Model 57
6.1.2 Sand Pluviation 58
6.1.3 Placement of Silt 59
6.2 Sand Saturation 62
6.3 Heating Procedures 63
7. RESULTS 65
7.1 Scope of Testing 65
7.2 Test 1 66
7.2.1 Time Series of Temperature, Water Content, and Soil Properties 68
7.2.2 Profiles of Temperature and Volumetric Water Content 75
7.3 Test 2 78
7.3.1 Time Series of Temperatures, Water Content and Soil Properties 79
7.3.2 Profiles of Temperature and Volumetric Water Content 84
7.4 Test 3 87
7.4.1 Time Series of Temperature, Water Content, and Soil Properties 88

7.4.2 Profiles of Temperature and Volumetric Water Content 94
7.5 Test 4 96
7.5.1 Time Series of Temperature, Water Content, and Soil Properties 97
7.5.2 Profiles of Temperature and Volumetric Water Content 102
7.6 Test 5 104
7.6.1 Time Series of Temperature, Water Content, and Soil Properties 104
7.6.2 Profiles of Temperature and Volumetric Water Content 108
8. ANALYSIS 112
8.1 Coupling between Soil Properties 112
8.2 Role of Array Spacing 118
8.3 Quantification of Heat Transfer 120
9. CONCLUSIONS 124
References 126

List of Figures

Figure 1.1 Heat exchange processes in a heat pipe 4

Figure 1.2 Heat pipe analogy within an array of soil-borehole heat exchangers 5

Figure 1.3 Heat transfer and water flow in an SBTES system in the vadose zone 7

Figure 1.4 Soil properties prior and during heating 8

Figure 2.1 WRCs for different geotechnical materials (McCartney 2007) 14

Figure 2.2 HCFs for different geotechnical materials (McCartney 2007) 17

Figure 2.3 Control volume for water flow in unsaturated soils 18

Figure 2.4 Steady state suction profiles during downward infiltration into an unsaturated soil layer (McCartney 2007) 20

Figure 2.5 Coupled heat and water transfer in soil, hydraulic conductivity (K), thermal liquid diffusivity (**DTl**), isothermal vapor diffusivity (**Dψv**), and thermal vapor diffusivity (**DTv**) as a function of soil liquid water content (**θl**). Transfer coefficients are based on the properties of a silt loam (Heitman et al. 2008) 28

Figure 3.1 Apparent thermal conductivity of saturated soil as a function of temperature (Philip and deVries 1957) 31

Figure 3.2 Thermal conductivity of Ottawa sand as a function of temperature (adapted from Flynn and Watson 1969) 31

Figure 3.3 Variation of thermal conductivity as a function of volumetric water content and temperature for dense (left) and loose (left) sand (Smits 2012) 32

Figure 3.4 Specific heat relation between gravimetric water content and temperature for a compacted soil (adapted from Duarte et al. 2006). 33

Figure 3.5 Profiles of gravimetric water content and temperature in a specimen of compacted bentonite in a thermal convection cell (Cleall et al. 2013) 35
Figure 4.1 Grain size distribution of Bonny silt 37
Figure 4.2 Compaction curves for Bonny silt. 39
Figure 4.3 Hydraulic conductivity as a function of void ratio for a variety of tests performed on Bonny silt 40
Figure 4.4 SWRCs for Bonny silt specimens having an initial void ratio of 0.69 under a range of net stresses (Khosravi 2011) 40
Figure 4.5 Thermal conductivity as a function of void ratio (McCartney et al. 2013) 41
Figure 5.1 Cross-section elevation and plan views of the soil container for a typical setup: (a) Instrumentation; (b) Expected heat and water transfer processes 42
Figure 5.2 Schematic of the overall experimental setup 43
Figure 5.3 (a) Picture of thermocouple profile probe; (b) Location of sensors in probe 44
Figure 5.4 Physical connection of thermal probe sensors to the data acquisition system. 45
Figure 5.5 (a) Pipe plug thermocouples; (b) Relative humidity and temperature gages 45
Figure 5.6 (a) Assembled temperature control cell, (b) Inside of temperature control cell 46
Figure 5.7 Schematic of thermal oedometer used as the temperature control cell (Vega 2012) .. 47
Figure 5.8 Temperature regulator 48
Figure 5.9 Dimensions and picture of the circulation pump 48
Figure 5.10 Closed loop heat exchanger: (a) Mechanism; (b) Picture 50
Figure 5.11 Plan view of heat exchanger setup with variables representing general instrumentation locations in the different tests 51
Figure 5.12 Decagon 5TE dielectric sensors with embedded thermistor. 52

Figure 5.13 KD2Pro thermal properties analyzer. 53
Figure 5.14 Mariotte bottle and mechanism 55
Figure 6.1 Experimental container with sensor level markings..... 58
Figure 6.2 Sand Placement in experimental container..... 59
Figure 6.3(a) Compacting rod, (b) Compaction of silt layer, (c) 5TE dielectric sensor placement 60
Figure 6.4 Volumetric water content calibration for the dielectric sensors 61
Figure 6.5 Pictures of the assembled experimental container in a typical test 64
Figure 7.1 Profiles of initial volumetric water content after compaction for Tests 1-4..... 66
Figure 7.2 Inlet and outlet heat exchange fluid temperatures in Test 1 67
Figure 7.3 Temperatures at the soil surface (under the hydraulic barrier) and in the laboratory for Test 1..... 69
Figure 7.4 Relative humidities at the soil surface (under the hydraulic barrier) and in the laboratory for Test 1..... 69
Figure 7.5 Time series data over time in Test 1from the dielectric sensors embedded at the center of the soil layer (a) Temperature; (b) Change in temperature 70
Figure 7.6 Average soil temperature with depth at four different horizontal distances from the center of the borehole heat exchanger array in Test 1 71
Figure 7.7 Time series data from the dielectric sensors embedded at different depths in Test 1: (a) Volumetric water content; (b) Change in volumetric water content 72
Figure 7.8 Time series data from dielectric sensors in Test 1: Degree of saturation at different depths in the center of the soil layer 73

Figure 7.9 Time series data from SH-1 sensor embedded in the middle of the unsaturated soil layer in Test 1: Thermal conductivity and specific heat 74
Figure 7.10 Post-test profile section of the unsaturated silt layer showing the drying zone within the heat exchanger array in Test 1 75
Figure 7.11 Dielectric sensor profiles for Test 1: (a) Temperatures; (b) Change in temperatures 76
Figure 7.12 Dielectric sensor profiles for Test 1: (a) Change in volumetric water content; (b) Degree of saturation 77
Figure 7.13 Dielectric sensor profiles for Test 1: Initial and final volumetric water contents 78
Figure 7.14 Inlet and outlet heat exchange fluid temperatures in Test 2 79
Figure 7.15 Temperatures at the soil surface (under hydraulic barrier) and in the laboratory for Test 2 80
Figure 7.16 Relative humidities at the soil surface (under hydraulic barrier) and in the laboratory for Test 2 80
Figure 7.17 Temperature data over time in Test 2 from the dielectric sensors embedded at the center of the soil layer (a) Temperature; (b) Change in temperature 81
Figure 7.18 Average soil temperature with depth at four different horizontal distances from the center of the borehole heat exchanger array in Test 2 82
Figure 7.19 Time series of dielectric sensors data for Test 2: Change in volumetric water content 83
Figure 7.20 Time series of dielectric sensor data for Test 2: Degree of saturation 83
Figure 7.21 Time series data from SH-1 sensor embedded in the middle of the unsaturated soil layer in Test 2: Thermal conductivity and specific heat 84

Figure 7.22 Dielectric sensor temperature profiles for Test 2: (a) Temperatures; (b) Change in temperatures 85
Figure 7.23 Dielectric sensor profiles for Test 2: (a) Change in volumetric water content; (b) Degree of saturation 86
Figure 7.24 Dielectric sensor profiles for Test 2: Initial and final volumetric water contents 87
Figure 7.25 Temperatures at the soil surface (under the hydraulic barrier) and in the laboratory for Test 3 88
Figure 7.26 Temperatures at the soil surface (under hydraulic barrier) and in the laboratory for Test 3 89
Figure 7.27 Relative humidities at the soil surface (under hydraulic barrier) and in the laboratory for Test 3 89
Figure 7.28 Time series of dielectric sensor data in Test 3: (a) Temperature; (b) Change in temperature 90
Figure 7.29 Average soil temperature with depth at four different horizontal distances from the outside of the borehole heat exchanger array in Test 3 91
Figure 7.30 Time series of dielectric sensor in Test 3: Change in volumetric water contentat different depths 92
Figure 7.31 Time series of dielectric sensor data in Test 3: Degree of saturation at different depths 92
Figure 7.32 Time series from SH-1 sensor embedded in the middle of the unsaturated soil layer in Test 3: Thermal conductivity and specific heat capacity 93
Figure 7.33 Post-test profile section of the unsaturated silt layer in Test 3 93
Figure 7.34 Dielectric sensor profiles in Test 3: (a) Temperatures; (b) Changes in temperature 94

Figure 7.35 Dielectric sensor profiles in Test 3: (a) Volumetric water content; (b) Degree of saturation 95
Figure 7.36 Dielectric sensor profiles: Initial and final volumetric water contents in Test 3..... 96
Figure 7.37 Inlet and outlet heat exchange fluid temperatures in Test 4 97
Figure 7.38 Temperatures at the soil surface (under hydraulic barrier) and in the laboratory for Test 4 98
Figure 7.39 Relative humidities at the soil surface (under hydraulic barrier) and in the laboratory for Test 4 98
Figure 7.40 Temperature data from the dielectric sensors embedded at the center of the soil layer (a) Temperature; (b) Change in temperature over time in Test 4 99
Figure 7.41 Average soil temperature with depth at four different horizontal distances from the center of the borehole heat exchanger array in Test 4 100
Figure 7.42 Time series of dielectric sensor data for Test 4: Change in volumetric water content 101
Figure 7.43 Time series of dielectric sensor data for Test 4: Degree of saturation 101
Figure 7.44 Dielectric sensors temperature profiles for Test 4: (a) Temperatures; (b) Change in temperatures 102
Figure 7.45 Dielectric sensor profiles for Test 4: (a) Change in volumetric water content; (b) Degree of saturation 103
Figure 7.46 Dielectric sensor profiles for Test 4: Initial and final volumetric water content..... 104
Figure 7.47 Time series of ielectric sensor data in Test 5: (a) Temperature; (b) Change in temperature 105

Figure 7.48 Time series of dielectric sensors data in Test 5: (a) Volumetric water content; (b) Change in volumetric water content 106
Figure 7.49 Time series of dielectric sensor data in Test 5: Degree of saturation at different depths 107
Figure 7.50 Time series from SH-1 sensor embedded in the middle of the unsaturated soil layer in Test 5: Thermal conductivity and specific heat capacity 108
Figure 7.51 Dielectric sensor profiles in Test 5: (a) Temperatures; (b) Change in temperatures 109
Figure 7.52 Dielectric sensor profiles in Test 5: (a) Volumetric water content; (b) Degree of saturation 110
Figure 7.53 Dielectric sensor profiles: Initial and final volumetric water content in Test 5 111
Figure 8.1 Apparent thermal conductivity and degree of saturation as a function of the change in during Test 1 112
Figure 8.2 Apparent thermal conductivity and degree of saturation as a function of the change in during Test 2 113
Figure 8.3 Apparent thermal conductivity and degree of saturation with temperature changes in Test 3 113
Figure 8.4 Thermal conductivity and specific heat capacity with degree of saturation in Test 1 114
Figure 8.5 Thermal conductivity and specific heat capacity with degree of saturation in Test 2 115
Figure 8.6 Thermal conductivity and specific heat capacity with degree of saturation in Test 3 115

Figure 8.7 Test 1 thermal profile probes data: Temperatures at diferent radial locations 116

Figure 8.8 Thermal conductivity inside and outside the borehole array in Test 1..... 117

Figure 8.9 Dielectric sensors time series: Degree of saturation with variations in borehole heat exchangers spacing 118

Figure 8.10 Total energy transferred for Tests 1, 2, 3 and 4..... 120

Figure 8.11 Energy transfer and storage over time in Test 3..... 123

1. INTRODUCTION

1.1 Motivation

Soil-borehole thermal energy storage systems (SBTES) are an approach to provide efficient renewable resource-based thermal energy for the heating and cooling of buildings (Sibbit et al. 2007; Zhang et al. 2012; McCartney et al. 2013a). They function by storing thermal energy in the subsurface soil or rock, then subsequently harvesting it at a later time. An example of a successful SBTES project is the Drake Landing Solar Community in Alberta, Canada (Sibbit et al. 2007). This project involves storage of heat collected from solar thermal panels in the summer within an array of closed-loop geothermal borehole heat exchangers. Heat is withdrawn from the array during the winter by circulating fluid through the heat exchangers and transferring it to the community of 52 houses. SBTES systems are similar to conventional ground-source heat exchange (GSHE) systems, where a fluid is circulated within a closed-loop pipe network installed in vertical boreholes to shed or absorb heat from the surrounding subsurface. However, they differ from conventional GSHE systems in that a heat pump may not be necessary, as the stored thermal energy can be used directly. SBTES systems are a convenient alternative to other energy storage systems such as batteries, brine tanks, or phase change fluids, as they are low cost, involve storage of renewable energy (solar thermal energy), and are space efficient.

1.2 Problem Statement

Zhang et al. (2012) analyzed the heat exchange processes at the Drake Landing site, and found that the efficiency of heat extraction is approximately 25%. Although this number is low, the Drake Landing site has been functional for several years and is able to provide 90% of the heating from the SBTES system (Sibbit et al. 2007). Although SBTES systems have been shown to be functional in practice, there is still an opportunity to improve the efficiency of heat transfer

into and out of the array of geothermal boreholes. In order to improve the heat exchange process in SBTES systems, one possibility is to take advantage of the mechanisms of coupled heat transfer and water flow in zone of unsaturated soil encountered near the ground surface. This zone of unsaturated soil above the water table is generally referred to as the vadose zone. During operation of a SBTES system in the vadose zone, the water content of unsaturated soils is expected to vary due to thermally induced water flow, and the thermo-hydraulic properties of the soil (e.g., hydraulic conductivity, specific heat, apparent thermal conductivity) may vary with temperature (Smits et al. 2012). Accordingly, it may be possible to engineer a SBTES system in the vadose zone to take advantage of phase change phenomena in the pore water to obtain greater heat injection and extraction rates, making the SBTES system more efficient (McCartney et al. 2013a). Specifically, the transfer of latent and sensible heat due to phase change of pore water in an unsaturated soil layer may lead to enhanced heat transfer due the formation of a convective cell in the ground between the borehole heat exchangers. Although the specific heat of water is greater than that of most soil grains, meaning that an unsaturated soil may have lower heat storage capabilities than a saturated soil, the rate of heat transfer to and from the ground is also important to the operation and efficiency of SBTES systems.

During heating of an array of soil-borehole heat exchangers, coupled heat transfer and water flow is expected to occur within the array, meaning that convection should be considered in simulating the movement of heat in unsaturated soils subject to a temperature gradient. When water in unsaturated soil is heated to the point that it vaporizes, it will move upward due to buoyancy and toward colder regions away from the heat source, releasing latent energy as it cools and condenses. After condensing to liquid form, the water will flow downward due to gravity and back toward the dry soil around the heat source due to capillarity. This process is referred to as a

convective cell for coupled water and heat flow. Sakaguchi et al. (2009) observed the formation of such a convective cell in an unsaturated soil layer, and observed an increase in apparent thermal conductivity with increasing temperature and justified this increase with latent heat transfer processes occuring in the soil. Lu (2001) found that the rate of heat transfer in a convective cell in an unsaturated soil layer may be up to 10 times faster than the case where heat conduction is the only means of heat transfer. In this study, the mechanisms of latent and sensible heat transfer associated with phase change of pore water are investigated to evaluate their impact on heat transfer within an array of geothermal heat exchangers in an unsaturated silt layer.

1.3 Hypothesis

The hypothesis of this research is that the formation of a convective cell with coupled heat and water flow will lead to an increase in the rate of heat transfer from the borehole heat exchangers into the soil. A common application that incorporates coupled heat and water flow to enhance heat transfer that has analogous aspects to the problem under investigation is a heat pipe. A heat pipe is a device that involves a closed system containing a fluid that changes in phase and flows in response to thermal can capillary gradients to enhance the transfer of heat from a source to a sink. The configuration of a heat pipe that is used to cool electronic devices along with the different flow processes are shown in Figure 1.1. The heat pipe in this figure consists of a casing (i.e., a closed system) filled with a working fluid (typically carbon dioxide or ammonia) that changes in phase from liquid to vapor in the range of temperatures experienced by the heat source. The casing has a heat source at one end and a heat sink at the other, connected by a wick that permits the working fluid to flow in liquid form from the cold end back to the hot end by capillarity. At point 1) in Figure 1.1, the working fluid absorbs thermal energy until reaching the required latent energy for vaporization. At point 2), the working fluid in vapor form travels through the cavity toward the

colder heat sink due to a vapor pressure gradient. When the working fluid in vapor form reaches point 3), it condenses and releases its latent heat adiabatically. The working fluid in liquid form then migrates back toward the heat source through the wick due to a capillary pressure gradient, after which then the process starts again.

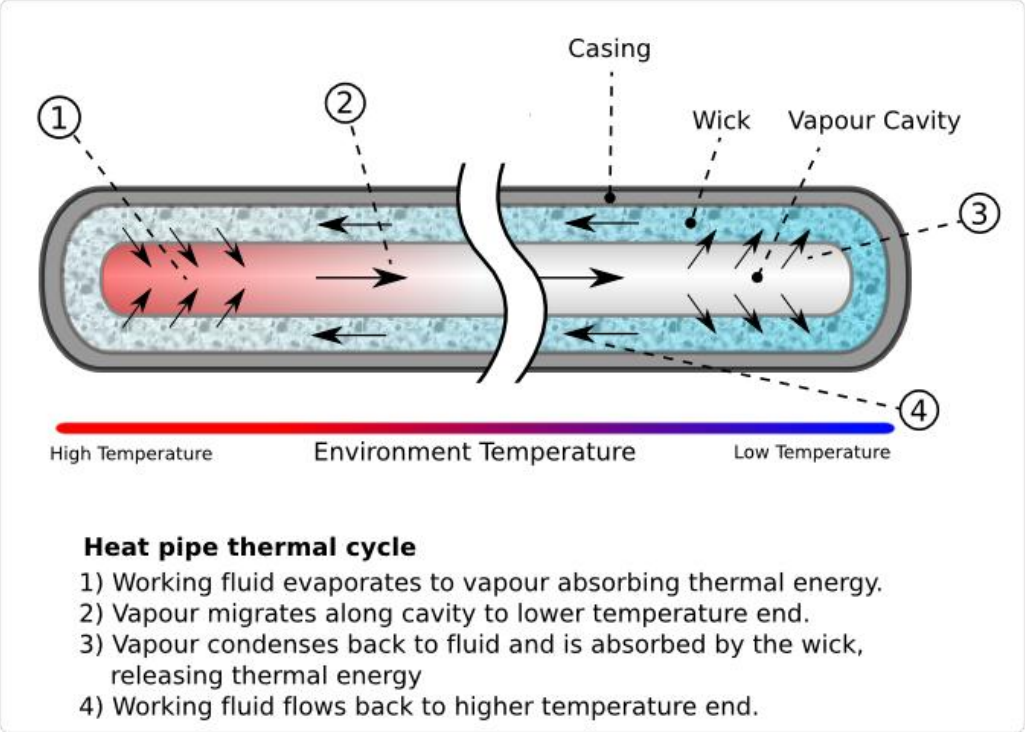

Figure 1.1 Heat exchange processes in a heat pipe

It is possible that similar coupled heat transfer and water flow processes will occur in the unsaturated soil layer within a soil-borehole heat exchanger array in which case water is the working fluid. One difference between the two systems is that the boreholes provide a cylindrical heat source, and the cooler soil within the array (or outside of the array) is the heat sink. Further, the soil-borehole array is not a completely closed system, as heat and water vapor will flow away from the borehole heat exchangers in all directions. The mechanisms of heat transfer and water flow in the analogous convective cell expected within a borehole heat exchanger array are shown in 2-dimensions in Figure 1.2. As water in the pores of the unsaturated soil around the heat

exchangers is heated, it will vaporize and decrease in density. The vapor flows through the pores away from the borehole heat exchanger heat source (i.e. upward and toward the middle of the heat exchanger array, or away from the array) due to buoyancy and thermally induced water flow. The water vapor will then condense after reaching the soil surface or the colder zone of soil between the heat exchangers. Accordingly, enhanced heat transfer will occur when latent energy is absorbed by the water during vaporization and released during condensation. This implies that heat will be transferred at a greater rate from the heat exchangers to the soil within the exchanger array, which in turn implies that greater heat exchanger spacings can be used to store heat in a larger zone of soil within the array. It is expected that the convective cycle may break down after the temperature of the soil within the array reaches a uniform temperature.

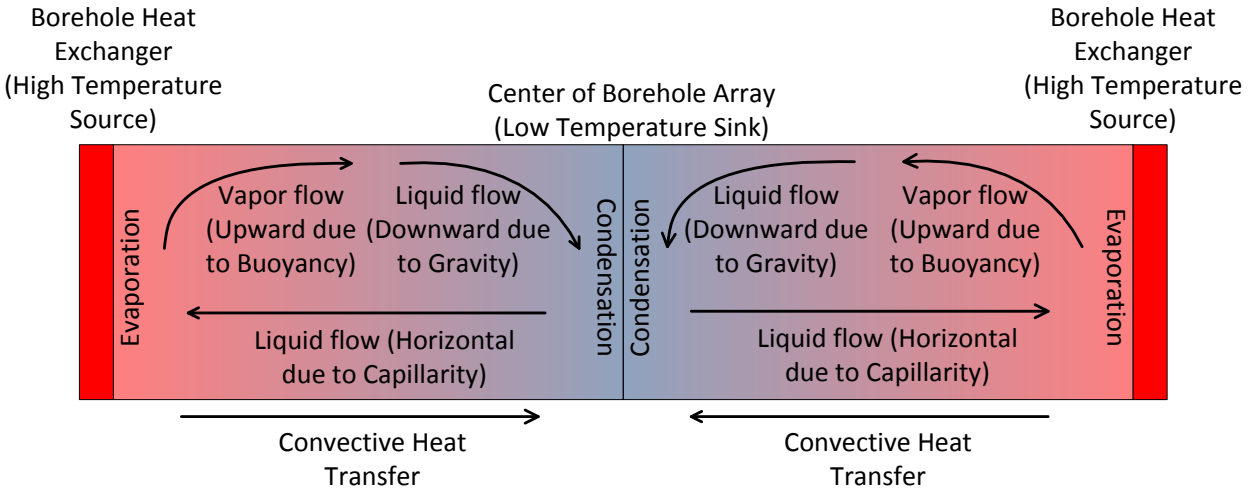

Figure 1.2 Heat pipe analogy within an array of soil-borehole heat exchangers

One issue with the heat pipe analogy in the unsaturated soil within an array of heat exchangers is that it is not a closed system. Water may be lost from the zone of soil within the array to the soil outside of the array. Further, the boundary conditions in the vertical direction are different than in the heat pipe shown in Figure 1.1, as most unsaturated soil layers have a water table at some depth where the temperature is relatively steady, and a relatively dry upper surface

that fluctuates in temperature with the ambient air temperature. However, the formation of a convective cell can be facilitated by installing a hydraulic barrier at the soil surface to prevent escape of water vapor, as well as an insulation layer to minimize loss of stored heat into the atmosphere.

A schematic of a hypothetical convective cell in a triangular SBTES that incorporates an insulated hydraulic barrier near the soil surface is shown in Figure 1.3. This hypothetical convective cell builds upon the concept developed by McCartney et al. (2013a), but clarifies how condensation and downward liquid water flow will occur within the center of the array. Although the heat transfer and water flow processes are not the same as in the heat pipe in Figure 1.1, the two-phase convective cell (Lu 2001) is similar to a heat pipe as the processes are expected to be similar to those shown in the soil element in Figure 1.2. During heating, water in the soil pores will absorb heat from the heat exchanger arrays and vaporize. The vapor will rise due to buoyancy toward the soil surface through the unsaturated soil body. When the water vapor reaches the hydraulic barrier near the ground surface (which has a relatively low temperature compared to the boreholes), the water will condense and release latent heat. The liquid water will form a saturated layer that will sink downward toward the water table under the pull of gravity and capillary forces. This convective cell is different from a heat pipe in that the goal is to increase the transfer of heat from the borehole heat exchangers into the soil rather than trying to move heat from one end of the to the other.

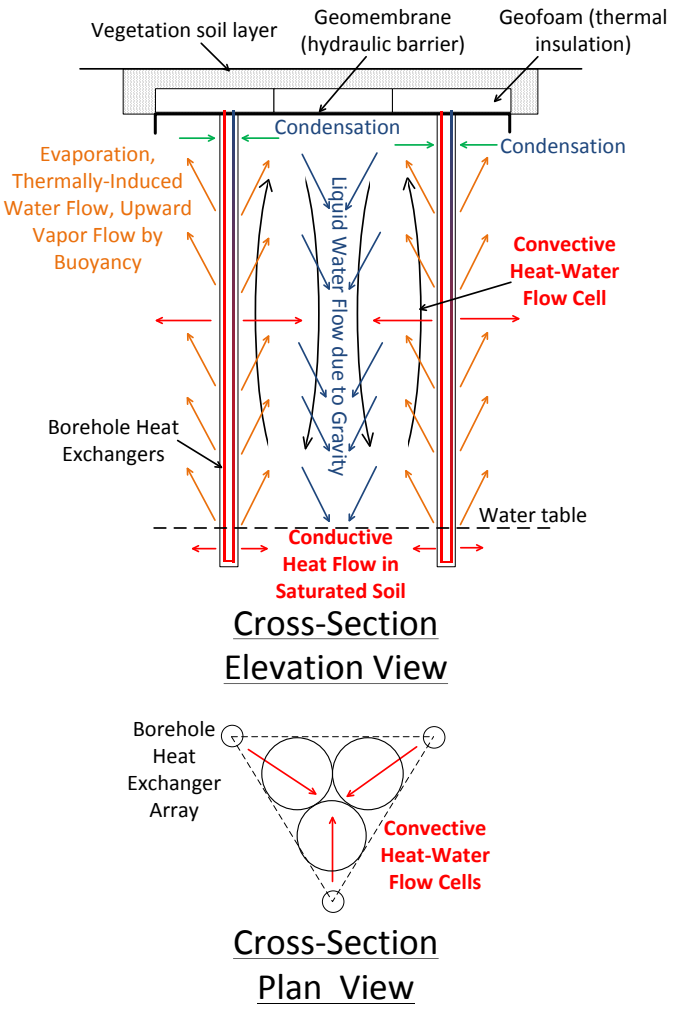

Figure 1.3 Heat transfer and water flow in an SBTES system in the vadose zone

In natural conditions, the thermo-hydraulic properties of unsaturated soil layers vary with depth due to gravity drainage and surface infiltration and evaporation. The air permeability and water permeability follow inverted trends with depth as the pores in the soil mass will either be filled with air or water. Thermal conductivity, specific heat and water content are expected to be higher in the bottom portion of the unsaturated soil layer due to its proximity to the water table. Smits et al. (2012) observed that the apparent thermal conductivity of an unsaturated sand increased with temperature due to the effects of thermally induced water flow. One of the hypotheses of this research is that the formation of a convective cell may result in a uniform

distribution in water content with height in the soil layer, which would subsequently lead to uniform, enhanced thermo-hydraulic properties of the unsaturated silt with depth. Specifically, coupled heat transfer, liquid water flow, and water vapor flow may cause these properties to become constant with depth during heating. Following this line of thought, schematics of the expected thermo-hydraulic properties of the unsaturated soil before and after heat exchange starts are shown in Figure 1.4. After a convective cycle forms, it is possible that heat transfer will be enhanced by the uniformity of the thermal and hydraulic properties of the soil. Further, it is also possible that the heat storage of the unsaturated soil may be increased as the specific heat becomes more uniform over the height of the layer.

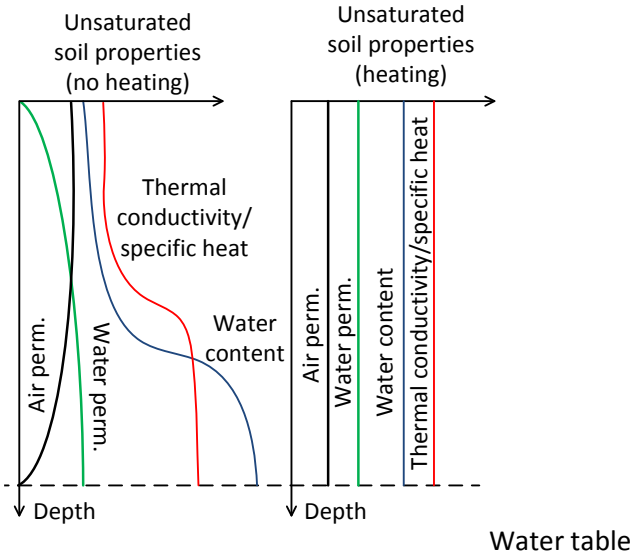

Figure 1.4 Soil properties prior and during heating

Another advantage of SBTES systems in the vadose zone is that the rate of lateral heat loss may be lower than in a SBTES system installed in a saturated soil layer. At room temperature conditions, unsaturated soils have lower thermal conductivity than water-saturated soils due to the effect of air filled pore spaces between the particles, which provide an insulating effect. This means that the rate of radial heat loss from a SBTES system in the vadose zone will be lower than that for a SBTES system installed in a saturated soil layer.

1.4 Objective and Approach

The primary objective of this study is to understand the mechanisms of coupled heat transfer and water flow in unsaturated soils during injection of heat into variably-spaced arrays of borehole heat exchangers. An improved understanding of these mechanisms can be used evaluate changes in the rate of heat transfer and energy storage in the vadose zone, and can be used to configure the geometry of heat exchanger arrays for energy storage in the subsurface. The data can also be used to calibrate analyses of coupled heat transfer and water flow with programs such as COMSOL (2008) or TOUGH2 (Pruess 1991; Pruess et al. 1999). After these programs are calibrated, they can be used for in-depth design of SBTES systems in the field.

The approach used in this study is to perform a series of physical modeling tests on a triangular array of three boreholes within an unsaturated silt layer. The physical model consists of a layer of unsaturated silt layer compacted atop a layer of sand in an insulated, 0.53 m-tall, 0.6 m-diameter cylindrical tank. A water table is imposed at the top of the sand layer. The heat exchangers are modeled using steel pipes bent into "U"-tube shapes that can be inserted into the soil layer. Tests are performed by circulating heated fluid through the steel pipes to apply a constant heat flux. The boundary conditions in the test are meant to simulate the behavior of the soil between the boreholes shown in Figure 1.3. A set of sensors are also incorporated into the silt layer to monitor changes in temperature, volumetric water content and thermal conductivity. This information can be used to evaluate coupling between the thermo-hydraulic properties of the soil and to infer mechanisms of coupled heat water and vapor heat transfer. This study involves several tests on borehole arrays having different spacing values in order to understand the effect of geometry on the formation of a convective cell in the unsaturated silt layer.

1.5 Scope

Chapter 2 includes an overview and explanation of the process involved in coupled heat water and vapor flow and a review of previously done studies. Chapter 3 includes a summary of properties of the materials used in the physical modeling experiments. An overview of the experimental setup along with information regarding the different instrumentation is given in Chapter 4. The methodology used to perform the different experiments are described in Chapter 5. This includes soil placement conditions, the process for saturation of the sand layer, and heating procedures. The results obtained from the different physical modeling experiments are presented in Chapter 6. The analysis of the data presented in Chapter 7 includes calculations of heat transfer and heat storage, an evaluation of the role of borehole spacing, and the relationship between coupled heat and water flow and the apparent thermal conductivity 7. The conclusions drawn from the physical modeling tests are presented in Chapter 8.

2. THEORETICAL BACKGROUND

2.1 History

Coupled heat transfer and water flow in unsaturated soils has been applied in many areas of engineering, including fluid transport in textile materials, wood drying, oil extraction, contaminant migration, drying of granular materials, heat exchangers, and heat transport in thermal insulation (Jahangir and Sadrnejad 2012). In agricultural engineering, the coupled flow of heat and water has been used in the prediction of the thermo-hydraulic interaction between surficial soils and the atmosphere. In geotechnical engineering, these concepts have been applied in the evaluation of geothermal heat exchange systems in the vadose zone and in predicting the behavior of compacted soils an understanding of the swelling and shrinkage of compacted clays used to encapsulate nuclear waste. Coupled heat and water flow has been studied through both physical experiments and theoretical models (Smith 1943; Philip and deVries 1957; Woodside and Kusmak 1958).

In the 1940s and 1950s, advancements in hydrology and agriculture lead to several new contributions to research on water flow in unsaturated soils, without taking into account soil deformation. An early study by Smith (1943) studied the movement of water in isothermal and nonisothermal conditions through unsaturated soils around a heating source. Smith (1943) discovered that in addition to water movement through unsaturated soils that are subject to temperature gradients, convective flux of dry air and pore water vapor will occur. Smith (1943) also discovered that water content gradients can also be affected by other convective currents in the pores of unsaturated soils.

Philip and deVries (1957) proposed the liquid island theory, which stated that when the pores between soil particles contain water and the soil is subject to a temperature gradient, latent

heat transfer will occur when both heat and vapor move from the a zone of high temperature to another of lower temperature. Their approach also considered liquid water flow in response to volumetric water content gradient rather than a hydraulic-head gradient. Their volumetric water content-based formulation may be applicable to the analysis of homogeneous and isotropic systems in horizontal flow conditions, which is usually not the case in real-life applications. There are controversies regarding the liquid island theory as it does not take into account the liquid flow from the colder side to the hotter side of the pore (Jahangir et al. 2012). Luikov (1996) derived a set of partial differential equations that considered the coupled heat and mass transfer in the determination of the total head distributions in porous media, using thermodynamic processes. These equations are directly related to the prediction of retention behavior in unsaturated media or coupled migration of heat and water in soils. All these studies indicated that the soil temperature regime strongly affects soil water dynamics and coupling multiple processes is a useful approach for explaining their mechanisms.

In this literature review, water flow through unsaturated soils will be reviewed, along with a discussion of relevant soil properties. Then heat flow processes in soils including conduction and convection in soils will be reviewed along with a discussion of relevant soil properties. Finally, the coupling between heat transfer, water flow, and vapor flow will be discussed.

2.2 Water Flow in Unsaturated Soils

2.2.1 Hydraulic Potential in Unsaturated Soils

In an unsaturated soil, water is partially bound to solid surfaces (adsorptive pressures) via electric fields and short-range attractive forces (van Der Waals forces) and partially at the interface with the gaseous phase (capillary pressures). Hence, the liquid phase is (compared to saturated flow) constrained to narrower and more tortuous channels. Water is a wetting fluid for most soil

particles, which implies that the air-water menisci between individual soil particles are convex, tensioned membranes (McCartney 2007). Thus, the air pressure is greater than the water pressure, so the water pressure has a negative magnitude when air is under atmospheric pressure. The adsorptive and capillary pressures together are referred to as matric suction ψ, which is expressed in terms of a pressure (units of kPa). Water flow in unsaturated soils is driven by the gradient in hydraulic energy of water per unit mass, quantified as:

$$\Phi = gz + \frac{1}{2}\left(\frac{v}{n}\right)^2 + \frac{P_w}{\rho_w} + \frac{P_o}{\rho_w} \tag{2.1}$$

where Φ is the hydraulic energy per unit mass, z is the vertical distance from a selected datum, v is the water discharge velocity, n is the porosity, and P_o is the osmotic pressure. In Equation (2.1), the four terms on the right hand side correspond to the potential energy, the kinetic energy, the energy due to the water pressure, and the energy due to the osmotic pressure. The water seepage velocity (v/n) is comparatively small in soils, leading to a negligible kinetic energy component. The osmotic pressure is typically considered constant for soils with different water contents, and consequently does not lead to a contribution to the gradient in hydraulic potential. Assuming that the pressure in the air phase is atmospheric (i.e., $P_a = 0$), $\psi = -P_w$, a simplified version Equation (2.1) can be written as follows:

$$\Phi = gz - \frac{\psi}{\rho_w} \tag{2.2}$$

2.2.2 Hydraulic Characteristics of Unsaturated Soils

2.2.2.1 Water Retention Curve (WRC)

An understanding of water storage in unsaturated soils is critical to interpreting their hydraulic behavior. Further, the amount of water storage in soils is closely related to the thermal conductivity of the soil. Water storage is quantified using the relationship between volumetric

water content and suction, referred to as the Water Retention Curve (WRC). WRCs for different geotechnical materials are shown in Figure 2.1, plotted in terms of the degree of saturation (which normalizes the curves to account for different porosities). The coarse-grained materials (sand and nonwoven geotextiles) show a significant decrease in degree of saturation over a narrow range in suction. The fine-grained materials (silt and clay) show a more gradual decrease in degree of saturation with increasing suction.

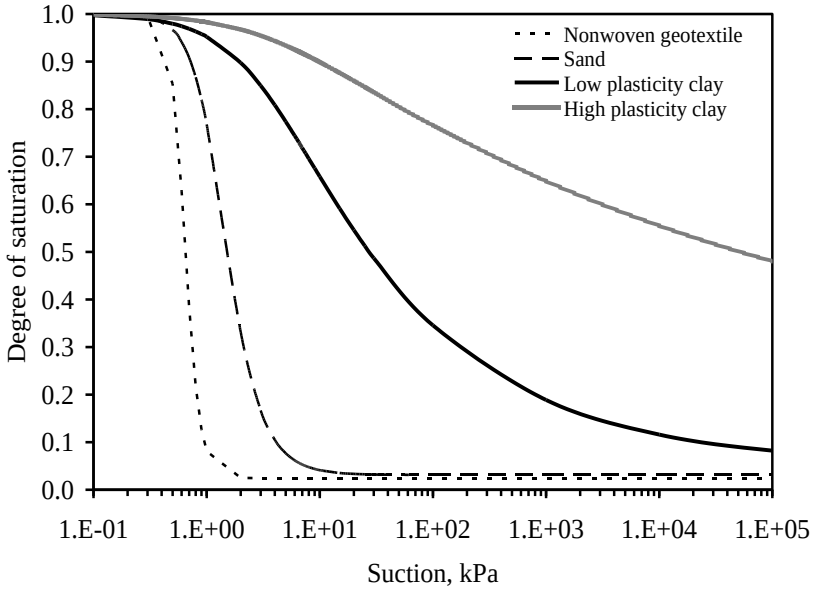

Figure 2.1 WRCs for different geotechnical materials (McCartney 2007)

The nonlinearity observed in these relationships is partially due to the range of pore size distributions for these materials. An important characteristic in a WRC is the air entry suction. During initial drying of a water-saturated specimen, the suction in the water increases, but air does not enter the specimen until the air entry suction is exceeded. Beyond the air entry suction, the degree of saturation decreases from 1.0 until reaching a value that remains constant with increasing suction. This degree of saturation is often referred to as the residual saturation. Residual saturation occurs when water only exists as films at particle contacts and cannot be extracted except in vapor form.

2.2.2.2 Hydraulic Conductivity Function (HCF)

In unsaturated soil, the available water flow pathways decrease as the degree of saturation decreases or as suction increases (McCartney 2007). This is quantified by the hydraulic conductivity function (HCF), which accounts for the decrease in conductivity with increasing suction or decreasing degree of saturation. The hydraulic conductivity (K) is the ratio between the discharge velocity through a soil and the total hydraulic gradient. Hydraulic conductivity can also be theoretically associated with the characteristics of the soil and fluid. For instance, K has been defined using the Hagen-Poisseuille law for viscous flow of water through a capillary tube, as follows (Mitchell 1979):

$$Q = \left(\frac{cd^2 \rho_w}{\mu_w} \right) Ag \left(\frac{H}{L} \right) \tag{2.3}$$

where Q is the flow rate over an area A, c is constant representing the pore shape, d is a characteristic pore diameter, ρ_w is the density of water, g is the gravitational constant, μ_w is the dynamic viscosity of water at a constant temperature and pressure, and H is the total head difference over a length L. The hydraulic conductivity of water in soil can then be defined as:

$$K = \frac{cd^2 \rho_w}{\mu_w} = \frac{\kappa \rho_w}{\mu_w} \tag{2.4}$$

where $\kappa = cd^2$ is the intrinsic permeability of the soil.

The hydraulic conductivity is considered constant with changes in pore water pressure for a saturated soil with a constant void ratio and environmental conditions (temperature, pH, etc.). However, the hydraulic conductivity is not constant with changes in suction for an unsaturated soil. The relationship between hydraulic conductivity and suction, also referred to as the HCF, is the function representing the change in the proportionality between the flow rate and gradient in an unsaturated soil. As the degree of saturation of a soil decreases, the total number of pathways

along which fluid can travel decreases. Accordingly, the HCF is a measure of the increased impedance to water flow with decreasing degree of saturation. The HCF can be represented as a function of volumetric water content (Θ) or suction (ψ), depending on the application. Experimental techniques based on outflow typically yield a HCF that is a function of Θ, while techniques based on suction gradients yield a HCF that is a function of ψ.

Early approaches to predict the HCF were empirical (Richards 1931; Wind 1955; Gardner 1958). For example, Gardner (1958) proposed an exponential model (linear in log-space):

$$K(\theta) = K_s e^{-\alpha\psi} \tag{2.5}$$

This model is particularly useful for analytical solution of Richards' equation. Statistical models based on pore size distributions were used later, with the goal of predicting the HCF from the WRC (Childs and Collis-George 1950; Burdine 1953; Mualem 1976). These approaches assume that the soil is an interconnected series of pores having a size distribution characterized by the shape of the WRC (Mualem 1986). Most of the models have the form:

$$\frac{K(\theta)}{K_s} = \left(\frac{\theta-\theta_r}{\theta_s-\theta_r}\right)^b \left(\frac{\int_0^{\Theta} \frac{dx}{\psi^{2-r}(x)}}{\int_0^{1} \frac{dx}{\psi^{2-r}(x)}}\right)^m \tag{2.6}$$

where b, r, and m are constants related to the pore size distribution, and x is an integration variable. The first term in Equation (2.6) is a correction factor used to account for tortuosity, while the second term is a ratio between the available, water filled fluid pathways and the total possible number of fluid pathways. Burdine (1953) suggested that b = 2, r = 0, and m = 1, while Mualem (1976) suggested that b = 0.5, r = 1, and m = 2. Mualem's assumption is considered to be more suitable for fine-grained soils (Leong and Rahardjo 1999). The HCF can be predicted from the macroscopic approach by inserting a WRC relationship into Equation (2.6). The most commonly

used predictive HCF is obtained by substituting the van Genuchten (1980) model into the Mualem (1976) model, although there are several other models available.

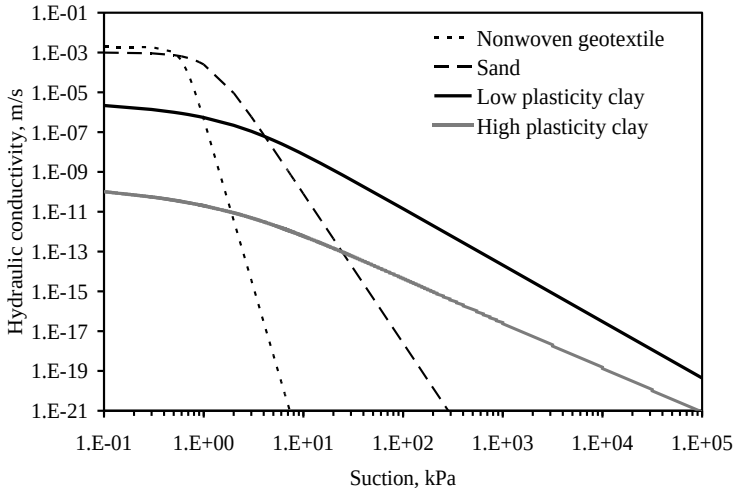

Figure 2.2 HCFs for different geotechnical materials (McCartney 2007)

The HCFs for different geotechnical materials predicted using the van Genuchten-Mualem model are shown in Figure 2.2. Near saturation, coarser-grained materials (sand and geotextiles) have high hydraulic conductivity, while finer-grained materials (silt and clay) have lower hydraulic conductivity (McCartney 2007). However, the coarse-grained materials are less conductive than the fine-grained materials after reaching residual saturation. As the fine-grained materials can retain more water in the pores as suction increases, there are available pathways for water flow even when unsaturated. An important consideration is the shape of the HCF at residual saturation. The curves in Figure 2.2 are shown over a wide range of hydraulic conductivity values to emphasize the relative difference between the materials.

2.2.2.3 Water Flow in Unsaturated Soils

The water seepage velocity through a soil in the vertical direction z can be estimated using Darcy's law and Equation (2.2), as follows:

$$v = \frac{Q}{A} = -\frac{K(\psi)}{g}\frac{\partial \Phi}{\partial z} = -K(\psi)\left(1 - \frac{1}{\rho_w g}\frac{\partial \psi}{\partial z}\right) \tag{2.7}$$

where Q is the volumetric flow rate, and A is the area of soil perpendicular to the flow direction.

The governing equation for water flow in unsaturated soils is referred to as Richards' equation. This equation is useful to define suction profiles for transient and steady-state water flow. A control volume of thickness *dz* is shown in Figure 2.3 to represent one-dimensional (1-D) water flow through a soil layer with thickness L. The datum is selected as the base of the soil layer.

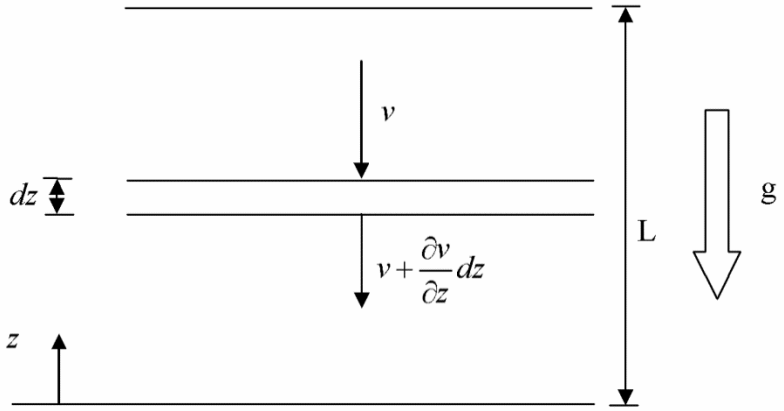

Figure 2.3 Control volume for water flow in unsaturated soils

The continuity principle in this control volume can be expressed as:

$$\frac{\partial \theta}{\partial t} = -\frac{\partial v}{\partial z} \tag{2.8}$$

where the left-hand side represents the change in water storage in the control volume, and the right hand side represents the change in flow rate across the control volume. Substitution of Equation (2.7) into Equation (2.8) leads to Richards' equation:

$$\frac{\partial \theta}{\partial \psi}\frac{\partial \psi}{\partial t} = \frac{\partial}{\partial z}\left[K(\psi)\left(1 - \frac{1}{\rho_w g}\frac{\partial \psi}{\partial z}\right)\right] \tag{2.9}$$

Richards' equation is a coupled, nonlinear, parabolic equation. For real flow situations, it is often solved numerically using finite differences or finite elements. Solutions can be challenging, as the

constitutive functions [K(ψ) and $\Theta(\psi)$)] are often nonlinear and may have undefined or zero derivatives. In addition, boundary conditions are rarely straightforward.

In simple situations, Richards' equation can be solved analytically. For instance, a useful analytical solution can be obtained for the suction profile in a soil layer during steady-state infiltration. Dell'Avanzi et al. (2004) developed an analytical solution for Richards' equation using Gardner's model to represent the HCF. The suction profile at steady state is:

$$\psi\left(z_p\right) = -\frac{1}{\alpha}\ln\left[e^{\left(\ln\left|\left(v_p/K_s\right)+e^{-\alpha\psi_0}\right|-\alpha\rho_w g z_p\right)} - \frac{v_p}{K_s}\right] \tag{2.10}$$

where v_p is the discharge velocity in a prototype, z_p is the height of a prototype, α is a soil-specific fitting parameter for Gardner's model, and ψ_0 is the suction value imposed at the base of the specimen. The suction profiles for different imposed discharge velocities on a soil layer with a saturated bottom boundary are shown in Figure 2.4. Measurements of hydraulic conductivity are usually made near the top of the soil layer, where a zone develops with a unit hydraulic gradient (i.e., constant suction). In this zone, the hydraulic conductivity of the soil is equal to the infiltration rate. Given the α parameter for Gardner's model, the limiting suction in the upper zone of the soil layer may also be predicted (Dell'Avanzi et al. 2004):

$$\psi_\infty = -\frac{1}{\alpha}\ln\left(-\frac{v_p}{K_s}\right) \tag{2.11}$$

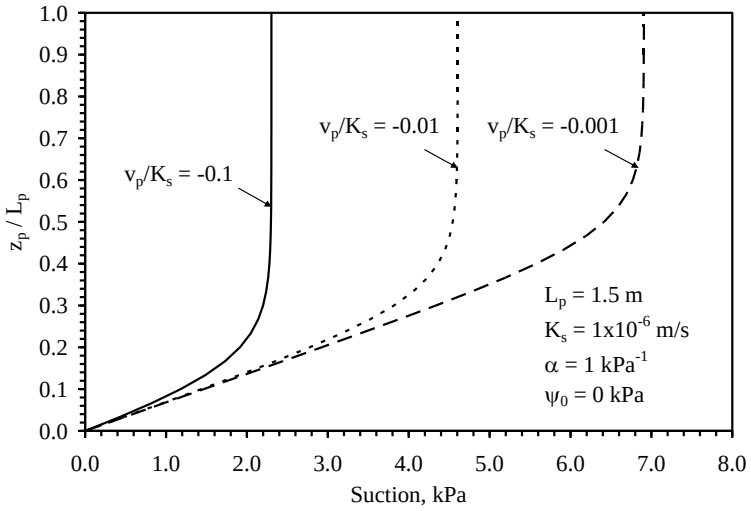

Figure 2.4 Steady state suction profiles during downward infiltration into an unsaturated soil layer (McCartney 2007)

2.3 Heat Transfer in Soils

This section discusses the mechanisms involved in heat transfer in soils. Soil is a multiple phase system with a complex heat transfer mechanism involving conduction, radiation, convection, vapor diffusion, vaporization and condensation processes and freezing-thawing processes (Carslaw and Yeager 1959; Brandl 2006). Brandl (2006) observed that radiation usually contributes only negligibly to heat transfer in soils, except near the surface. The energy absorbed during phase change (freezing and thawing, evaporation and condensation) are a large source of heat transfer, especially if the fluid moves away from the heat exchanger before changing phase. Hence, in this study, heat transfer in soils will be reduced to the processes of heat conduction, heat convection and latent heat transfer. The total heat transfer in soil can be then quantified as follows:

$$\dot{q}_{tot} = \dot{q}_{cond} + \dot{q}_{l,conv} + \dot{q}_{v,cond} + \dot{q}_{lat} \quad (2.12)$$

where $\dot{q}_{tot}$ is the total heat transfer, $\dot{q}_{cond}$ the heat transfer due to conduction, $\dot{q}_{l,conv}$ the heat transfer due to liquid convection, $\dot{q}_{v,cond}$ the heat transfer due to vapor convection and $\dot{q}_{lat}$ the latent heat transfer.

2.3.1 Conductive Heat Transfer

Conduction refers to one of the modes of heat transfer in which energy transfer occurs in the solid phase of the porous media and fluids which are at rest (Hermansson et al. 2008). The grains of a soil, typically, are in contact with each other at distinct contact points and pores between grains are filled with a mixture of air and water. When completely dry the heat flow passes mainly through the grains, but has to bridge the air-filled gaps around the contact points. At very low water contents, thin adsorbed water layers cover the grains. The thickness of these layers increases with increasing water content as discussed by deVries (1958). At higher water contents, rings of liquid water form around the contact points between the grains. From this point, the thermal conductivity increases rapidly with increasing water content. This behavior was observed by Smits (2010; 2012) at steady temperatures and with a temperature gradient. At even higher water contents, the pores are completely filled with water resulting in a further but slower increase in thermal conductivity Heat transfer can be quantified using Fourier's heat transfer equation. According to Fourier's law, the heat flux density ($\dot{q}_{cond}$), the heat flux for heat volume Q through an arbitrary area A during time t can be quantified by equation (Brandl 2006):

$$\dot{q}_{\text{cond}} = \frac{Q}{At} = \frac{\dot{Q}}{A} = -\lambda \frac{\partial T}{\partial n} \tag{2.12}$$

where λ is the thermal conductivity and $\partial T/\partial n$ is the temperature gradient in the direction n. The term $\partial T/\partial n$ can be rewritten:

$$\frac{\partial T}{\partial n} = \frac{\partial T}{\partial x} e_x + \frac{\partial T}{\partial y} e_y + \frac{\partial T}{\partial z} e_z = \nabla T = gradT \tag{2.13}$$

where ∇T or $gradT$ is the gradient in temperature with space, and λ is the thermal conductivity. Hence Equation (2.12) becomes:

$$\dot{q}_{\text{cond}} = -\lambda \left(\frac{\partial T}{\partial x} e_x + \frac{\partial T}{\partial y} e_y + \frac{\partial T}{\partial z} e_z \right) = -\lambda \nabla T = -\lambda gradT \tag{2.13}$$

Physically, the thermal conductivity (λ) represents the ability of a material to conduct heat by molecular excitation. Therefore, heat transfer occurs at a higher rate across materials of high thermal conductivity than across materials of low thermal conductivity. In the case that conduction is used to simulate a problem in which convective heat transfer may occur, the thermal conductivity is referred to as the apparent thermal conductivity.

2.3.2 Convective Heat Transfer

Convection is the transfer of internal energy into or out of an object by the physical movement of a surrounding fluid that transfers the internal energy along with its mass. Although the heat is initially transferred between the object and the fluid by conduction, majority of energy transfer comes from the motion of the fluid. Convection can arise naturally through the creation of convection cells or can be forced by pushing the fluid across the medium or by the medium through the fluid. In this study, convection will be studied through the creation of a convection cell as discussed in the introduction. There are two distinct types of convective heat transfers: liquid convection and vapor convection. Heat transfer by fluid convection and vapor convection can respectively be expressed by the following heat flux terms:

$$\dot{q}_{\text{l,conv}} = c_w \rho_w \bar{v}_w (T - T') \tag{2.14}$$

$$\dot{q}_{\text{l,conv}} = c_v \rho_v \bar{v}_v (T - T') \tag{2.15}$$

where c_w and c_v are the specific heat capacity of the soil water and vapor, respectively. ρ_w and ρ_v are the density of the soil water and vapor, respectively. $\bar{v}_w$ and $\bar{v}_v$ are the vector of water and vapor velocity, respectively ($\bar{v} = ki$), and T' is the temperature of the surrounding environment. Latent heat transfer occurs as a result of phase changes of water (vaporization and condensation. The latent heat flux term can be defined as follows:

$$\dot{q}_{\text{lat}} = L_0 \rho_v \bar{v}_v \tag{2.16}$$

The magnitude of latent heat flux greatly depends on the amount of vapor transfer occurring in the soil: It increases with decreasing water content (Brandl 2006).

2.4 Coupled Heat and Water Flow

Coupled heat and water transfer refers to the connected process of heat and water flow in and through the three phase (e.g. solid, liquid, and gas) soil system, where heat may be latent and/or sensible and water may be liquid and/or vapor (Heitman and Horton 2011). Philip and deVries (1957, 1958, 1963) are the pioneers of the theoretical description of coupled heat and water transfer. They assume that gradients in water content and temperature are the main drivers of liquid flow. Their theory assumes (1) the soil is rigid and inert; (2) hysteresis of water retention curves and transport coefficients can be neglected; (3) transfer of mass and energy occurs only in the vertical direction; (4) the driving forces for water are temperature and matric pressure head gradients and gravity; (5) osmotic potential is negligible; (6) there is local thermodynamic equilibrium within the soil; and (7) heat transfer occurs by conduction and by convection of latent heat and sensible heat.

2.4.1 Water Flow due to Temperature Gradients

The total water flow in soils subject to a temperature gradient occurs in two distinct components: liquid and vapor. Vapor transport is primarily a diffusive process resulting from the development of a vapor pressure gradient in response to a thermal gradient. In saturated soils, the vapor flow is negligible as there is no air space for the vapor to move. Unsaturated soils have enough pore spaces to allow vapor movement. In this study we will focus on the unsaturated soils case. Liquid water is observed to flow from areas of warm to cold due to the presence of a surface tension gradient, as the surface tension of water in contact with air decreases with increasing temperature. The total water flux in an unsaturated soil can be written as:

$$\dot{q}_w = \dot{q}_l + \dot{q}_v \tag{2.17}$$

where $\dot{q}_w$ is the total water flux, $\dot{q}_l$ is the water flux due to liquid flux and $\dot{q}_v$ is the water flux due to vapor flux. They are all in units of kg m^{-2} s^{-1}. Liquid flux can be broken into matric potential driven flow and thermal gradient driven flow. Liquid flux driven by a gradient in matric potential and elevation can be described using a form of Darcy's law, as follows:

$$\dot{q}_l/\rho_l = -K\left(\frac{\partial \psi}{\partial z} - 1\right) \tag{2.18}$$

where ρ_l (kg m^{-3}) is the liquid density of water, K (m s^{-1}) is the hydraulic conductivity, ψ (m) is the matric potential, z (m) is the depth in the direction of gravity. The water flux driven by a temperature gradient can be expressed as follows:

$$\dot{q}_l/\rho_l = -D_{Tl}\frac{\partial T}{\partial z} \tag{2.19}$$

where D_{Tl} (m^2 s^{-1} K^{-1}) is the liquid thermal diffusivity and T (K) is temperature. Thermal diffusivity is a measure of the ability of a substance to transmit a difference in temperature; expressed as the thermal conductivity divided by the product of specific heat capacity and density, as follows:

$$D = \frac{\lambda}{\rho c_p} - K \tag{2.20}$$

where c_p is the specific heat capacity and ρ the total density.

Combining Equations (2.18) and (2.19) yields the total liquid water flux within an unsaturated soil subject to temperature gradient, which can be defined as follows:

$$\dot{q}_l/\rho_l = -K\frac{\partial \psi}{\partial z} - K - D_{Tl}\frac{\partial T}{\partial z} \tag{2.21}$$

The water vapor flux $\dot{q}$v is treated as simple diffusion process and can be expressed as follows:

$$\dot{q}_l/\rho_l = -D\,\frac{\partial \rho_v}{\partial z} \tag{2.22}$$

where ρ_v (kg m^{-3}) is the water vapor density and D (m^2 s^{-1}) is the effective molecular diffusivity. In Equation (2.21), ρ_v can be expressed in terms of ψ and T. The term $\partial\rho_v/\partial z$ can be expanded to account for ψ and T, as follows:

$$\frac{\partial \rho_v}{\partial z} = \frac{\partial \rho_v}{\partial \psi}\frac{\partial \psi}{\partial z} + \frac{\partial \rho_v}{\partial T}\frac{\partial T}{\partial z} \tag{2.23}$$

Combining this equation with Equation 2.21, the heat flux due to vapor flux becomes:

$$\dot{q}_v = -D\,\frac{\partial \rho_v}{\partial \psi}\,\frac{\partial \psi}{\partial z} - D\eta\frac{\partial \rho_v}{\partial T}\frac{\partial T}{\partial z} \tag{2.24}$$

where η is a constant to account for increased vapor flux due to locally enhanced thermal gradients across air gaps within the soil mass (Cass et al. 1984). Equation (2.23) can then be simplified as follows:

$$\dot{q}_v/\rho_l = -D_{\psi v}\,\frac{\partial \psi}{\partial z} - D_{Tv}\,\frac{\partial T}{\partial z} \tag{2.25}$$

where according to Philip and deVries (1957), $D_{\psi v}$ (m^2 s^{-1}) and D_{Tv} (m^2 s^{-1} K^{-1}) are the matric vapor and thermal vapor diffusivities, respectively, defined implicitly by Equation (2.23). The vapor water flow $\dot{q}_v$ is divided by ρ_l so that $D_{\psi v}$ and D_{Tv} to provide volume fluxes equivalent to transport terms defined in Equation (2.20) for liquid water.

Similarly, as the total flux of water in the soil mass, the total mass of water within the soil mass can be expressed as follows:

$$\theta\rho = \theta_l\rho_l + \theta_v\rho_v \tag{2.26}$$

where θ_l (m^3 m^{-3}) and θ_v (m^3 m^{-3}) are the fractions of the soil mass occupied by liquid water and by vapor water, respectively, such that the sum of θ_l and θ_v corresponds to the volume of voids. By conservation of mass, the continuity equation can be expressed as follows:

$$\frac{\partial}{\partial t}(\theta_l \rho_l + \theta_v \rho_v) = \nabla \dot{q}_w \tag{2.27}$$

where t (s) is time, and $\nabla \dot{q}_w$ (kg m^{-2} s^{-1}) is the gradient in total water mass flux. Expanding the terms on the left side of Equation (2.27), using the dependency of ρ_v on ψ and T noted above and also the functional relationship between θ and ψ, the following governing equation can be defined as follows:

$$\rho_l \frac{\partial \theta_l}{\partial t} + \rho_v \frac{\partial \theta_v}{\partial t} + \theta_v \frac{\partial \rho_v}{\partial \psi}\frac{\partial \psi}{\partial \theta_l}\frac{\partial \theta_l}{\partial t} + \theta_v \frac{\partial \rho_v}{\partial T}\frac{\partial T}{\partial t} = \nabla \dot{q}_w \tag{2.28}$$

Finally, incorporating Equations (2.17), (2.21), and (2.25), and dividing all terms by ρ_l, a general partial differential equation to describe transient water flow for unsaturated, non-isothermal conditions can be obtained, as follows:

$$1 + \left(\frac{\theta_v}{\rho_l}\frac{\partial \rho_v}{\partial \psi}\frac{\partial \psi}{\partial \theta_l} - \frac{\rho_v}{\rho_l}\right)\frac{\partial \theta_l}{\partial t} + \frac{\theta_v}{\rho_l}\frac{\partial \rho_v}{\partial T}\frac{\partial T}{\partial t} = \nabla\left[\left(K + D_{\psi v}\right)\frac{\partial \psi}{\partial z} + \left(D_{Tl} + D_{Tv}\right)\frac{\partial T}{\partial z} + K\right] \tag{2.29}$$

It should be noted that the relation between θ_l and θ_v was used to replace $\partial\theta_v/\partial t$ with $-\left(\partial\theta_l/\partial t\right)$ in order to simplify the expression.

2.4.2 Heat Transfer with Water Flow

As explained at the beginning of this section, heat transfer in soils can be reduced to the processes of heat conduction, heat convection and latent heat transfer. The total heat flux in the soil mass can be expressed as follows:

$$\dot{q}_h = -\lambda \frac{\partial T}{\partial z} - \rho_l L D_{\psi v}\frac{\partial \psi}{\partial z} + c_l (T - T_0)\dot{q}_w \tag{2.30}$$

where $\dot{q}_h$ (W m^{-2}) is the total heat flux in the soil, λ (W m^{-1} K^{-1}) is the thermal conductivity of the soil, L (J kg^{-1}) is the latent heat of vaporization, c_l(J kg^{-1} K^{-1}) is the specific heat of liquid water, *T(K)* and $T_0(K)$ are the temperature of the soil at a given time and the initial or reference temperature, respectively. The first term on the right of the equation is from Fourier's law of

conductive heat transfer. Thermal conductivity λ is highly dependent on water content and temperature. The second term on the right is diffusion of water vapor, with associated latent heat from phase change, according to the matric potential gradient. The diffusion vapor flux is a component of the flux given in Equation (2.25). The rightmost term in Equation (2.30) is the convective transfer of sensible heat associated with the mass water flux. Because the water flux is on a mass rather than a volume basis, it is appropriate to consider the specific heat of the liquid to determine the associated heat transfer. However, the quantity of heat must be determined by specifying some reference state $c_l\ T_0$ (Heitman and Horton 2011).

When the soil is subject to a temperature gradient, the total heat stored is a combination of latent and sensible heat. This can be expressed as follows:

$$q_h = (c_s\rho_b + c_l\rho_l\theta_l + c_v\rho_v\theta_v)(T - T_0) + L\rho_v\theta_v \tag{2.31}$$

where c_s (J kg^{-1} K^{-1}) is the specific heat of the solid, ρ_b (kg m^{-3}) is the soil bulk density (mass of solid per total soil volume), and c_v (J kg^{-1} K^{-1}) is the specific heat of the vapor. By the conservation of energy, the change in the quantity of heat stored per volume of soil with time is equivalent to the gradient in total heat flux ∇q_h. This can be expressed as follows:

$$\nabla q_h = \frac{\partial}{\partial t}[(c_s\rho_b + c_l\rho_l\theta_l + c_v\rho_v\theta_v)(T - T_0) + L\rho_v\theta_v] \tag{2.32}$$

Combining Equations (2.30) and (2.32), the gradient of heat flux in an unsaturated soil mass subject to a temperature gradient can be expressed as follows:

$$\nabla\dot{q}_h = \nabla\left[-\lambda\frac{\partial T}{\partial z} - \rho_l L D_{\psi v}\frac{\partial\psi}{\partial z} + c_l(T - T_0)\dot{q}_w\right] \tag{2.33}$$

The theory of coupled heat flow indicates that gradients in ψ and T are the main drivers for heat flux. It is also important to recognize how the magnitudes of liquid and vapor fluxes vary with associated transfer coefficients, which greatly depend on, among other things, the soil water

content (Nassar and Horton, 1997). Heitman et al. (2008) investigated the water flow coefficients as a function of water content of the soil for a silt loam. Typical relationships between K (m s^{-1}), $D_{\psi v}$ (m s^{-1}), D_{Tl} (m^2 s^{-1} K^{-1}) and D_{Tv} (m^2 s^{-1} K^{-1}) and different values of water content defined by Heitman et al. (2008) for a silt loam are shown in Figure 2.5.

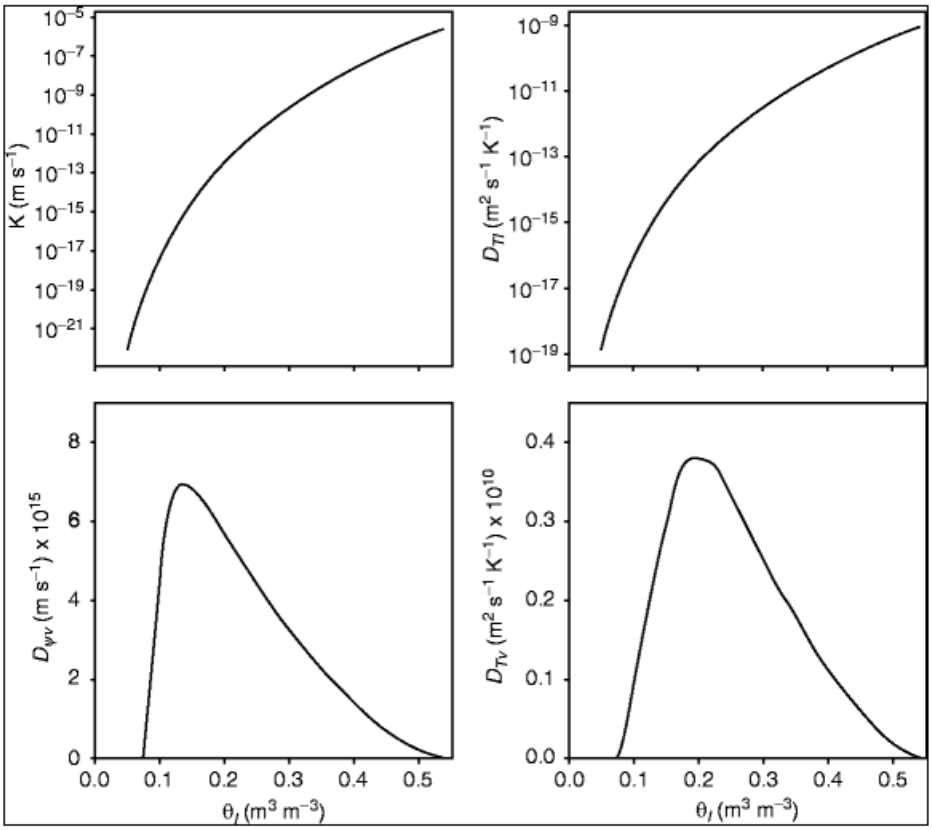

Figure 2.5 Coupled heat and water transfer in soil, hydraulic conductivity (K), thermal liquid diffusivity (D_{Tl}), isothermal vapor diffusivity ($D_{\psi v}$), and thermal vapor diffusivity (D_{Tv}) as a function of soil liquid water content (θ_l). Transfer coefficients are based on the properties of a silt loam (Heitman et al. 2008)

Several conclusions can be drawn from evaluation of the trends in Figure 2.5. At very low water contents, convection through either liquid or vapor is minimal, as evidenced by the small magnitudes of all four transfer coefficients. When liquid water is absent or water content is very small, conduction must be the dominant mechanism for heat transfer. As water content begins to increase, all transfer coefficients increase, but the most pronounced increase is for vapor

coefficients $D\psi_v$, and D_{Tv}. In this range, air-filled porosity remains high so as to readily allow diffusion (with rate also depending on drivers). Hence, while conduction may remain important, heat transfer may also occur with convection via vapor, particularly latent heat. As liquid water content continues to increase and air-filled porosity is diminished, $D_{\psi v}$, and D_{Tv} then decline. However, liquid transfer coefficients K and D_{Tl} continue to increase over the whole range in θ_l. Because liquid water carries with it only sensible heat, and because the vapor flux is limited, convection in wet soil occurs primarily as sensible heat alone.

3. LITERATURE REVIEW

3.1 Variables Affecting the Thermal Properties of Unsaturated Soils

Farouki (1981) presented a thorough literature review on thermal conductivity, and found that heat conduction is mainly influenced by the composition, structure, packing, density, porosity, grain and pore size structure, as well as by contacts and binding effects. Brandon and Mitchell (1989) presented results of experiments that were conducted on sand by the thermal needle method to measure the thermal conductivity. Experimental observations indicate that the thermal conductivity of sand is strongly influenced by mineralogy, dry density, water content and temperature. Experiments in this study will focus on the effect of temperature and water content (or degree of saturation) on an unsaturated compacted silt.

3.1.1 Temperature Effects

Previous studies (Philip and deVries 1957; Hopmans and Dane 1986; Campbell et al. 1994; Smits 2012) have indicated that thermal conductivity is varies due to temperature changes.

deVries (1957) studied the transfer mechanisms in soils. In particular, he investigated the effect of temperature gradient on the thermal conductivity of liquid water. The values of apparent saturated thermal conductivity are shown in Figure 3.1. The results of their experiments implied that the thermal conductivity of water vapor increases drastically for higher temperatures. The value of λ for air is unaffected and the value of λ for water increases gradually with temperature.

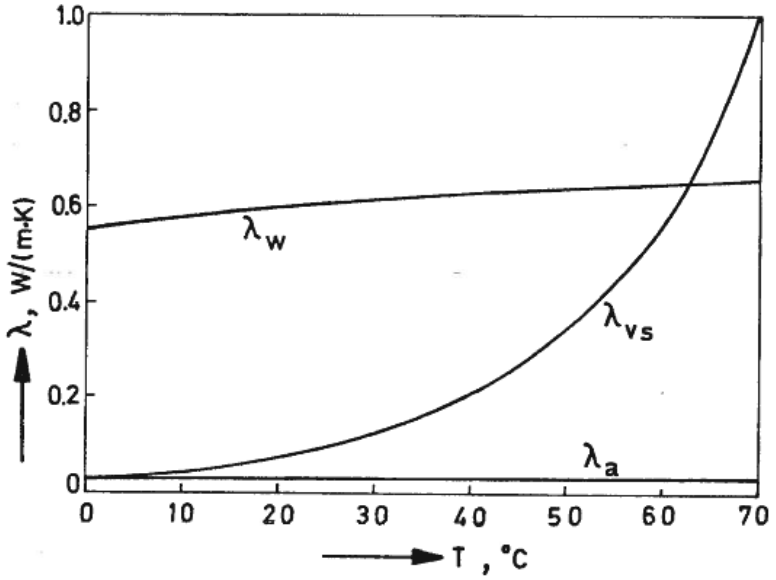

Figure 3.1 Apparent thermal conductivity of saturated soil as a function of temperature (Philip and deVries 1957)

Campbell et al. (1994) stated that λ increases dramatically with temperature in soils with high water content, reaching values up to three to five times higher at 90 °C than those at ambient temperature. The relationship between temperature and thermal conductivity for Ottawa sand at very high temperatures is shown in Figure 3.2. This graph was adapted from Flynn and Watson (1969) and covers a very wide range of temperatures.

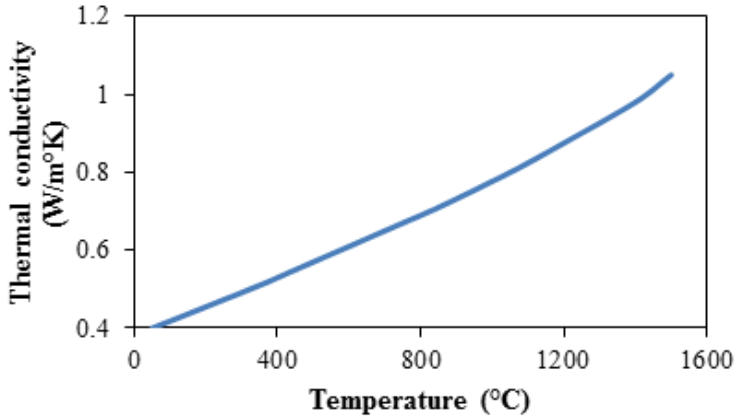

Figure 3.2 Thermal conductivity of Ottawa sand as a function of temperature (adapted from Flynn and Watson 1969)

3.1.2 Combined Effects of Saturation and Temperature

Smits et al. (2012) explored the combined effect of temperature and degree of saturation on the thermal properties of sands over a range of temperatures using a modified pressure plate apparatus with an embedded tensiometer, dielectric sensor, and thermal needle. Results from their tests on dense and loose 30/40 sands are shown in Figures 3.3(a) and 3.3(b), respectively. They observed that the apparent thermal conductivity of sand varies with both the degree of saturation (S) and temperature.

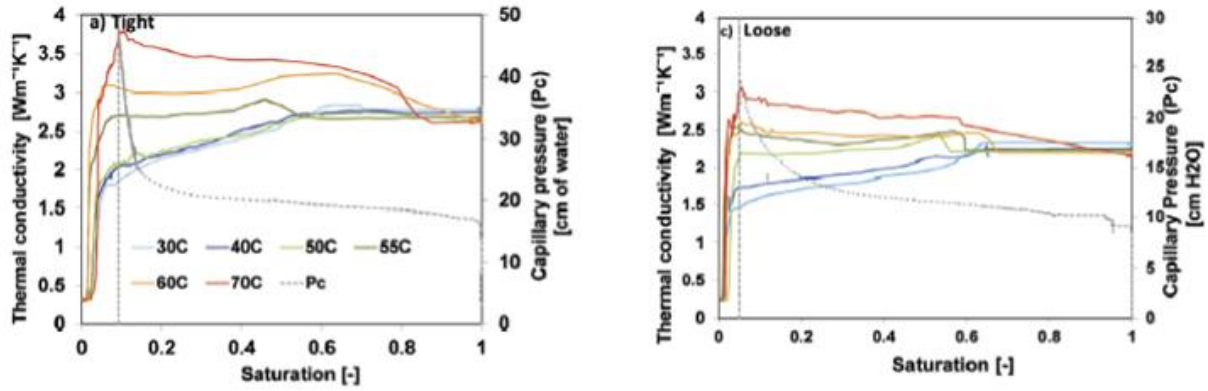

Figure 3.3 Variation of thermal conductivity as a function of volumetric water content and temperature for dense (left) and loose (left) sand (Smits 2012)

Below 50 °C, temperature does not have a significant effect on the λ-S plots is insignificant, but has a greater effect for temperatures ranging from 30 to 70 °C. At very low degrees of saturation and very high degrees of saturation the change in thermal conductivity is very small. The apparent thermal conductivity varies more widely for intermediate degrees of saturation. The increase in thermal conductivity at mid-range degrees of saturation may be due to the additional heat transfer in the form of evaporation and condensation between the "liquid islands" (Philip and deVries 1957). That is the reason why in unsaturated soils, coupled flow of heat, liquid water and water vapor occurs because there are both air pores and liquid islands present in the soil (Salomone et al. 1984). The explanation for this is that the effective contact areas between particles and water

are increased, which leads to an increase in the apparent thermal conductivity of the soil. When the degree of saturation of the soil approaches 1, the effective contact area no longer increases with increasing volumetric water content. Consequently, the significant increase in thermal conductivity with increasing volumetric water content is not evident when more water is added to fill the pore spaces.

Duarte et al. (2006) presented the experimental results for the impact of temperature on the thermal conductivity and specific heat of compacted residual soil. According to their findings, thermal conductivity of compacted soil at 25% gravimetric water content is two times greater than when the soil is almost dry. Results from literature have the same increasing trend as well. For a given temperature, the specific heat will increase as the water content increases, as shown in Figure 3.4. Since the thermal diffusivity of soils is a ratio of thermal conductivity and specific heat, it will not change with temperature and water content as both the other variables typically change by similar amounts. The trends in Figure 3.4 contradict the observations of Mitchell (1993) and Farouki (1986), who observed that specific heat is not sensitive to temperature changes. Their argument is that as the temperature within the soil body increases, its capacity to store more heat will decrease.

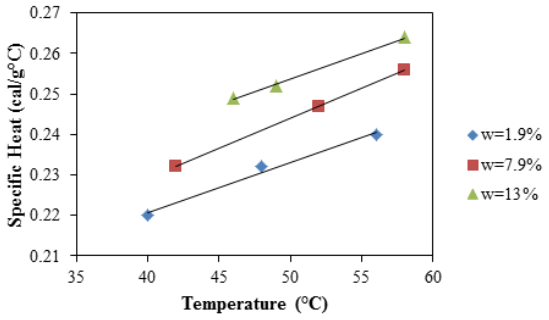

Figure 3.4 Specific heat relation between gravimetric water content and temperature for a compacted soil (adapted from Duarte et al. 2006).

3.2 Convective Cells in Unsaturated Soils

A convention cell is a self-contained convective zone in which a fluid, in its liquid or a gas phase is heated from below by a warm surface; the increase in temperature results in a decrease in density of the fluid, causing the hotter fluid to rise and cooler fluid to flow inward to replace it. As the warmer fluid rises, it loses its stored latent heat to the surroundings, becoming denser and heavier than the fluid below. When the fluid condenses in the cooler section, it spreads horizontally before drawn toward its starting point. Thermal convection in fluids heated from below is a classical problem and has been addressed extensively in both pure fluids and porous media (Lu 2001). As water in an unsaturated soil body is heated, it becomes less dense. By natural convection, the fluid flows upward through the unsaturated soil, where it cools down and condenses at the colder boundary. Cleall et al. (2013) developed a new cell to evaluate coupled heat and water flow within a specimen of compacted bentonite. The profiles of gravimetric water content and temperature at different times during heating the base of the specimen are shown Figure 3.5. Water was observed to move away from warm regions and accumulate in cool regions. They also observed that water subsequently moved back from the cooler regions to the warmer regions by capillarity, indicating the formation of a convective cell. In this study, an impervious insulation at the top of the specimen (colder boundary) was used to prevent water and heat loss to the surroundings.

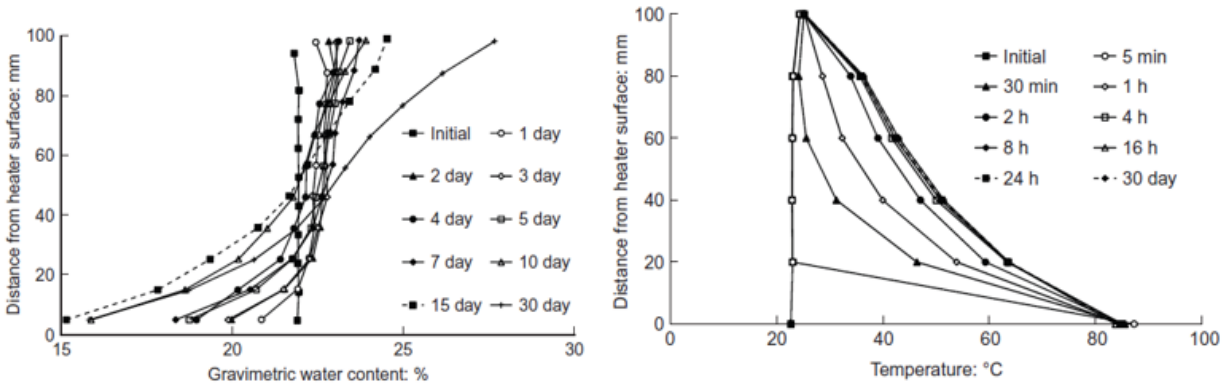

Figure 3.5 Profiles of gravimetric water content and temperature in a specimen of compacted bentonite in a thermal convection cell (Cleall et al. 2013)

Numerous studies have been performed to understand convection in porous media. Lu (2001) studied the onset of air convection in mine wastes covered with low-permeability covers, and used a dimensionless number called the "Rayleigh number" (R_a) to predict the onset of convection. The Rayleigh number is expressed as follows:

$$R_a = \frac{\Delta\rho g \kappa L}{\mu k} \tag{3.1}$$

where $\Delta\rho$ (kg m^{-3}) is the density difference between the air at the top and bottom of the soil over a length L (m), μ (kg m^{-1} s^{-1}) is the dynamic viscosity of air, g (m s^{-2}) is gravity, κ (m^2 s) is the thermal diffusivity, and k (m^2) is the permeability (m^2). Nield (1982) defined the critical Rayleigh number at which convection starts as $R_{a_{critical}} = 4\pi^2$, with the assumption that air is an ideal gas. Once the Rayleigh number reaches that threshold, convection is initiated within the soil body.

4. MATERIALS

The physical modeling experiments in this study were performed on a layered system involving a thin layer of sand overlain by a thick layer of compacted silt. The sand used in this study is referred to as "Nevada sand" and the silt used in this study is referred to as "Bonny silt". The physical properties of these soils are presented in this section.

4.1 Nevada Sand

A 62 mm-thick layer of Nevada sand with a dry density of 1518 kg/m^3 was used as the saturated layer beneath the vadose zone. For a relative density of 60%, it has a void ratio of 0.746 (Goode 2012). The sand was placed first in the container by dry pluviation from a height of 600 mm above the container level. To saturate the sand, a Mariotte bottle was placed at one of the bottom entry hole of the container and vacuum was applied on the other bottom entry hole. Physical properties of Nevada sand are shown in Table 4.1.

Table 4.1 Properties of Nevada Sand along with Relevant Placement Conditions.

Property	Value	Units
Relative density, D_r	60	%
Specific gravity, G_s	2.65	
Minimum void ratio, e_{min}	0.586	
Maximum void ratio, e_{max}	0.852	
Placement void ratio, e	0.746	
Placement dry density, γ_d	1518	kg/m^3

4.2 Bonny Silt

Bonny silt from the Bonny dam site in Yuma County located in eastern Colorado was used in this experiment as the unsaturated soil within the vadose zone. This soil has been characterized in previous experimental studies at the University of Colorado Boulder (Khosravi 2011; Coccia and McCartney 2012; Vega 2012; Khosravi et al. 2012; Alsherif and McCartney 2012). The findings from these previous studies include the physical properties of Bonny silt such as particle-

size distribution, Atterberg limits, specific gravity, compaction properties and thermal conductivity. These results are presented in this section.

4.2.1 Particle Size Distribution

The soil particle-size distribution of the Bonny silt was measured in previous experiments in accordance to ASTM D 422. The distribution of particle sizes larger than 75 μm (retained on the No. 200 sieve) was determined with a sieve analysis while that of particle sizes finer than 75 μm was determined using a hydrometer analysis (Vega 2012). The particle-size distribution curve is shown in Figure 4.1 and characteristic values from the distribution are summarized in Table 4.2. Because of the high fines content, the silt is expected to behave as a low-permeability soil.

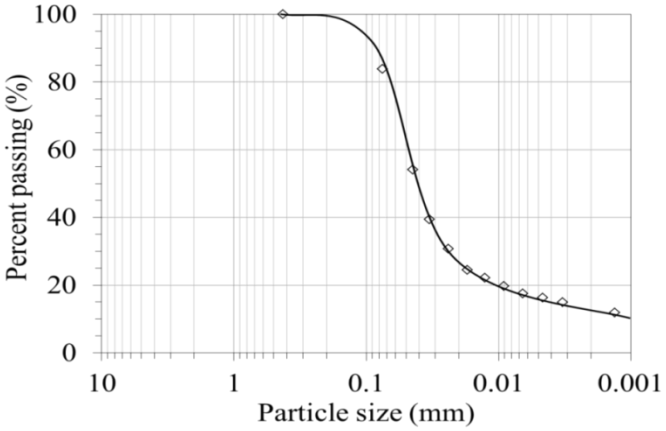

Figure 4.1 Grain size distribution of Bonny silt

Table 4.2 Characteristic values from the Bonny silt grain size distribution.

Parameter	Value
D_{10}	< 0.0013 mm
D_{30}	0.022 mm
D_{50}	0.039 mm
% Passing No. 200 Sieve	83.9 %
% Clay Size	14.0 %
% Silt Size	69.9 %
% Sand Size	16.1 %

4.2.2 Atterberg Limits

The Atterberg limits, which include the liquid limit (LL), plastic limit (PL), and plasticity index (PI), were measured for Bonny silt according to ASTM D 4318. LL, PL and PI values of this soil are 25, 21 and 4, respectively. Based on the Atterberg limits and the shape of the particle size distribution, Bonny silt is classified as CL-ML (inorganic silt) according to the Unified Soil Classification System (ASTM D 2487).

4.2.3 Specific Gravity

The specific gravity of Bonny silt was determined by means of a water pycnometer in accordance to ASTM D 854. The value of specific gravity for most soils is usually in the range of 2.6 to 2.9. Three tests were performed in previous experiments and the results yielded an average G_s value for Bonny silt of 2.63.

4.2.4 Compaction Characteristics

The standard Proctor compaction test (ASTM D 698) and the modified Proctor compaction test (ASTM D1557) were performed on Bonny silt to define the relationship between compaction water content and dry unit weight for different compaction energies. The standard and modified Proctor compaction curves for Bonny silt are presented in Figure 4.2. The standard Proctor compaction test revealed that the optimum water content and the maximum dry unit weight for Bonny silt are 16.3 kN/m^3 and 13.6%, respectively.

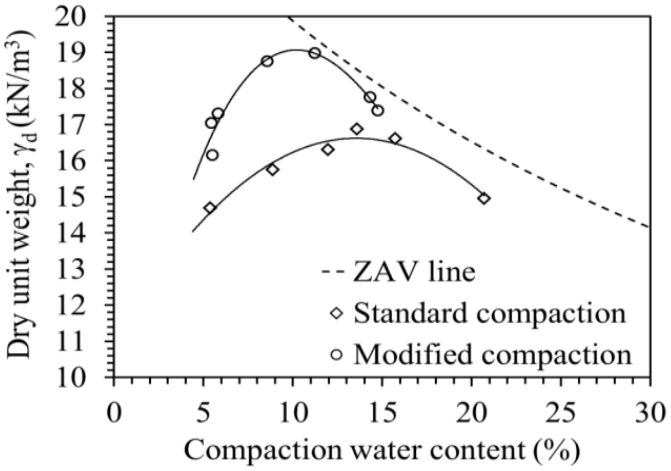

Figure 4.2 Compaction curves for Bonny silt.

4.2.5 Hydraulic Conductivity and Soil-Water Retention Curve

The hydraulic properties of Bonny silt were measured using the flow pump technique developed by Aiban and Znidarcic (1989). This technique was used to define the saturated hydraulic conductivity using a constant flow rate approach, and was later combined with the axis-translation technique to measure the soil-water retention curve (SWRC) and hydraulic conductivity function (HCF) of unsaturated soils.

A plot of saturated hydraulic conductivity for a variety of void ratios is presented in Figure 4.3. The data for this plot was taken from previous literature published using this technique. The hydraulic conductivity of saturated specimens having initial void ratios ranging from 0.5 to 0.8 ranges from 1×10^{-9} to 1×10^{-7} m/s. The SWRC for Bonny silt specimen having an initial void ratio of 0.69 under a range of net stresses are shown in Figure 3.4 (Khosravi 2011).

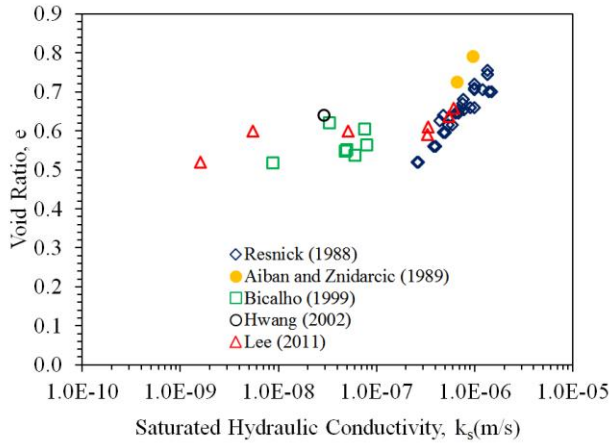

Figure 4.3 Hydraulic conductivity as a function of void ratio for a variety of tests performed on Bonny silt

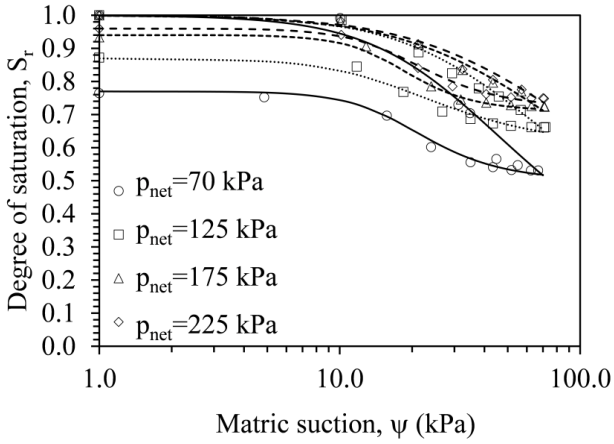

Figure 4.4 SWRCs for Bonny silt specimens having an initial void ratio of 0.69 under a range of net stresses (Khosravi 2011)

4.2.6 Thermal Conductivity

Thermal conductivity for Bonny silt was measured using a thermal needle test on a compacted silt specimen during isotropic compression, using the methodology described by McCartney et al. (2013b). Thermal conductivity of Bonny silt was measured as a function of the void ratio for two void ratio conditions. The test performed by inserting a thermal needle probe into a triaxial cell and then measuring thermal conductivity at those two void ratios throughout

consolidation. Results from the two tests performed on Bonny silt (Figure 3.5) shows that the thermal conductivity ranges from 1.37 to 1.47 W/(mK) for void ratios of 0.60 to 0.52.

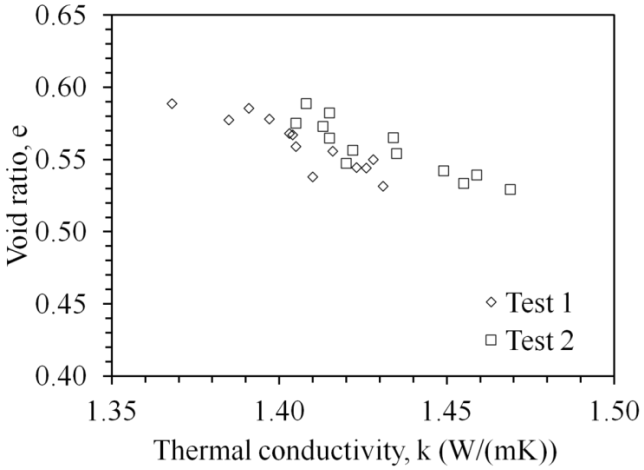

Figure 4.5 Thermal conductivity as a function of void ratio (McCartney et al. 2013)

5. EXPERIMENTAL SETUP

5.1 Overview

The experiment was conducted in a circular steel container that has a diameter of 603 mm and a height of 554 mm (Figure 5.1). The bottom of the container has two entry holes on each sides of its diameter to permit inflow and outflow of water. One of the holes in the base was linked to a Mariotte bottle used as a constant head reservoir to saturate the sand layer and maintain the water table at the top of the sand layer.

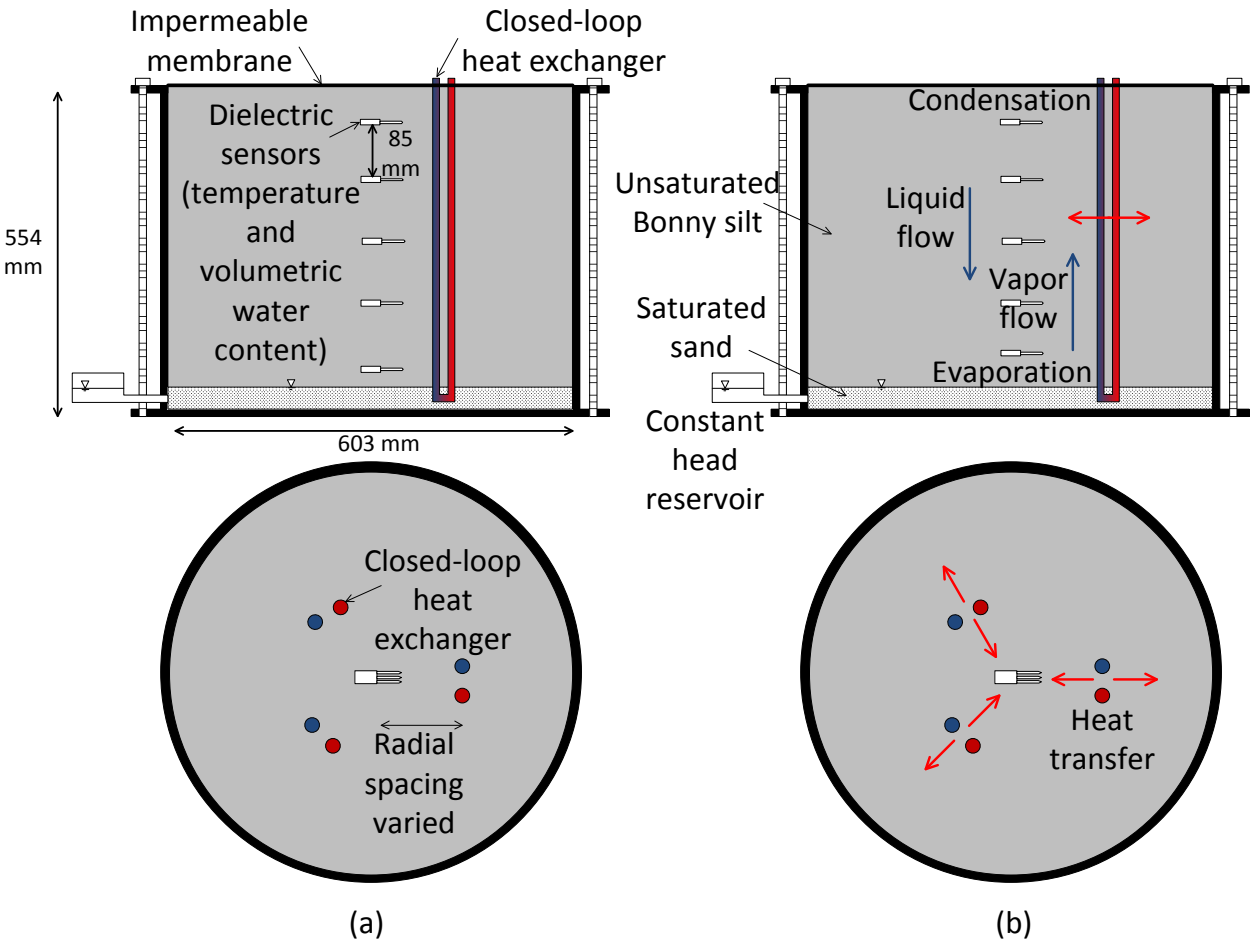

Figure 5.1 Cross-section elevation and plan views of the soil container for a typical setup: (a) Instrumentation; (b) Expected heat and water transfer processes

A temperature-regulated heating system coupled with a high temperature water pump was used to circulate water through steel closed-loop "U"-tube heat exchangers. The system consists

of a pressure cell and a heat regulator. The pressure cell has an outlet that provides hot water to the heat exchangers that are buried in the soil and an inlet that returns slightly colder water from them. The water in the pressure cell was pressurized using a pressure panel to ensure that the water does not vaporize under the elevated temperature, and to help in de-airing the circulation pump used to transfer fluid through the borehole heat exchangers. A schematic of the experimental set up is shown in Figure 5.2.

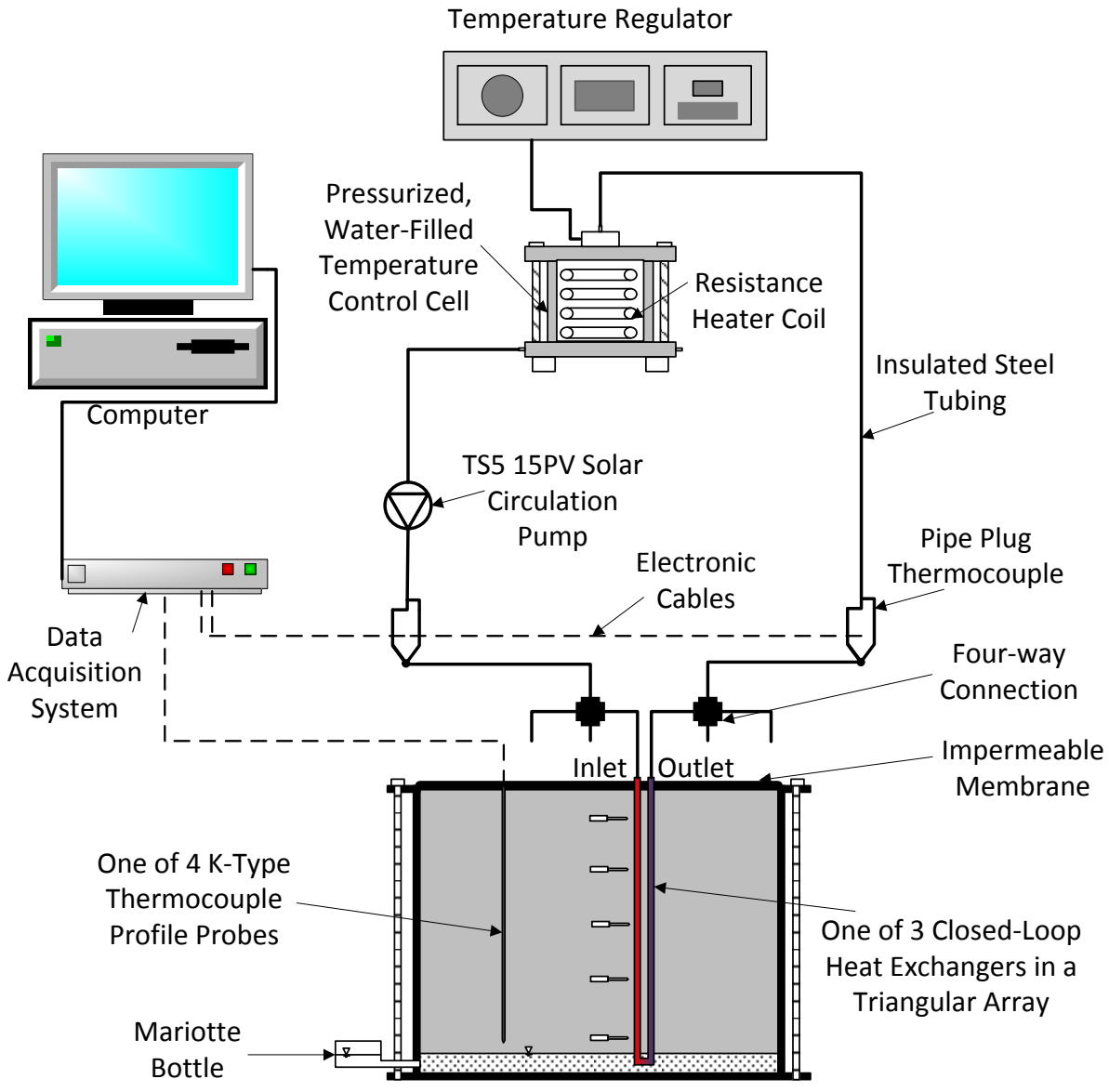

Figure 5.2 Schematic of the overall experimental setup

5.2 Temperature Probes

Four Type-K thermocouple profile probes shown in Figure 5.3(a) were inserted into the soil at different radial locations to measure transient changes in soil temperature. They were four thermocouple probes, 450 mm long and 2 mm in diameter. Each probe has six sensors embedded inside it at different points spaced 90 mm from the tip as shown in Figure 5.3(b).

(a)

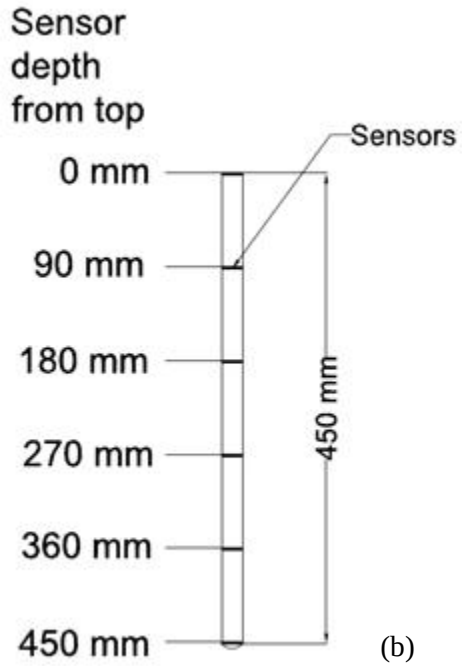

(b)

Figure 5.3 (a) Picture of thermocouple profile probe; (b) Location of sensors in probe

The connection cable of each sensor connects to a data acquisition box that has physical channels. The box in turn is connected to a data acquisition system and then connected to a computer (Figure 5.4). Virtual channels were created in LabView for the temperature sensors that correspond to the physical channels on the data acquisition system to get the readings from the sensors. In order to see how much heat is stored in the specimen, pipe plug thermocouples probes (Model TC-J-NPT-G-72 from Omega, Inc.) were also used to measure the temperature of the water going into and out of the heat exchanger tubes, as shown in Figure 5.5(a). They were mounted in

T-connections in the insulated tubing after the circulation pump and before circulating water returns to the pressure cell. Accordingly, they measure the collective heat transfer into the three borehole heat exchangers. Temperature changes and relative humidity at the surface of the specimen and in the experiment's room were monitored as well using EL-USB-2LCD digital thermocouples (Figure 5.5(b)) manufactured by Lascar Electronics. The EL digital thermocouples were programmable for measurements using the software EasyLog.

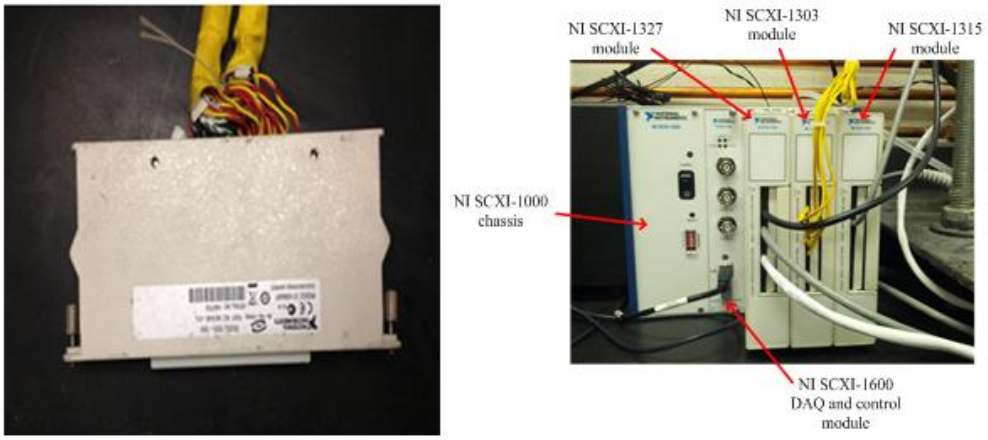

Figure 5.4 Physical connection of thermal probe sensors to the data acquisition system.

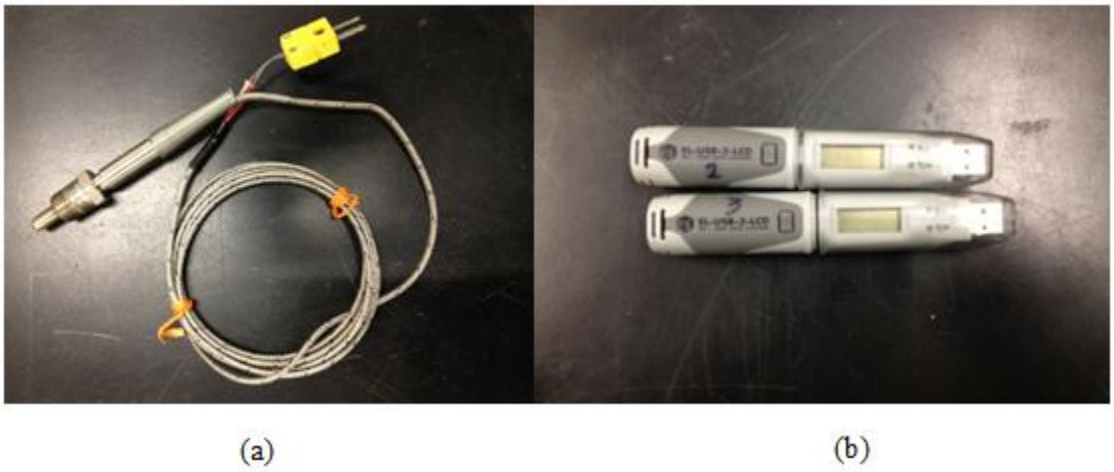

Figure 5.5 (a) Pipe plug thermocouples; (b) Relative humidity and temperature gages

5.3 Temperature Control System

The pressure cell is made of stainless steel. It has two functions used in this study. It is used to control the temperature of the heat exchanger fluid through a set of electrical resistance coils, and it is used to pressurize the fluid, as mentioned above. The pressure cell is cylindrical with an outside diameter of 153 mm and a height of 127 mm, and is closed at its top and bottom by two plates that are 25 mm thick. Pictures of the outside and inside of the pressure cell are shown in Figures 5.6(a) and 5.6(b), respectively.

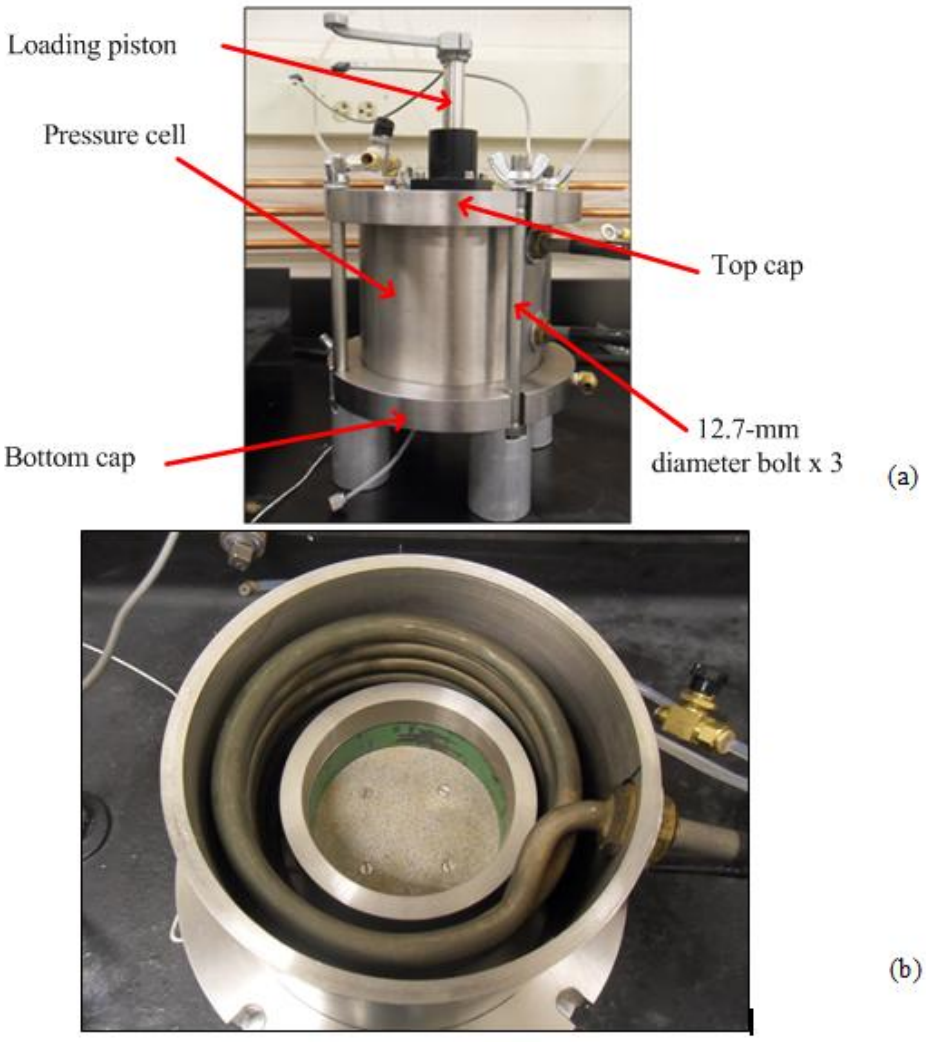

Figure 5.6 (a) Assembled temperature control cell, (b) Inside of temperature control cell

The cylinder and the top and bottom plates are held together by four 12.7 mm diameter bolts. Inside the pressure cell, there is a tubular coiled heater that goes along the inside wall of the pressure cell as shown in Figure 5.6(b). The heater was manufactured by Watlow electronics and has a heat output of 4500 Watts. A schematic drawing of the pressure cell is shown in Figure 5.7. The pressure cell contains two thermocouples that are linked to the temperature control unit (Figure 5.8). The latter is used to set the coils to the desired temperature. It has two temperature reading sources which are the thermocouples.

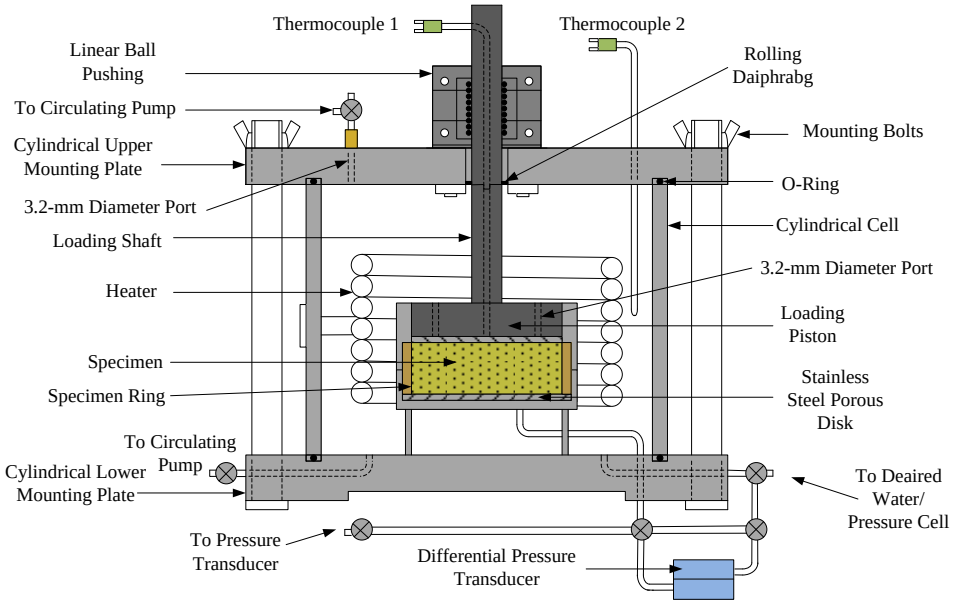

Figure 5.7 Schematic of thermal oedometer used as the temperature control cell (Vega 2012)

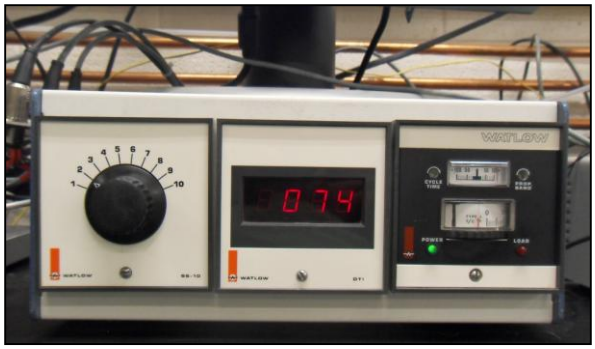

Figure 5.8 Temperature regulator

A solar powered DC circulation (Model TS5 15PV) water pump (Figure 5.9) manufactured by Heliatos Solar was used to circulate hot water through the heat exchanger tubes. One of the key features of the pump is the fact that it can operate at high temperatures. It is brushless which enables it to have more torque and a more efficient power. That also allows for a more continuous use of the pump with less maintenance required due to brushes wearing out.

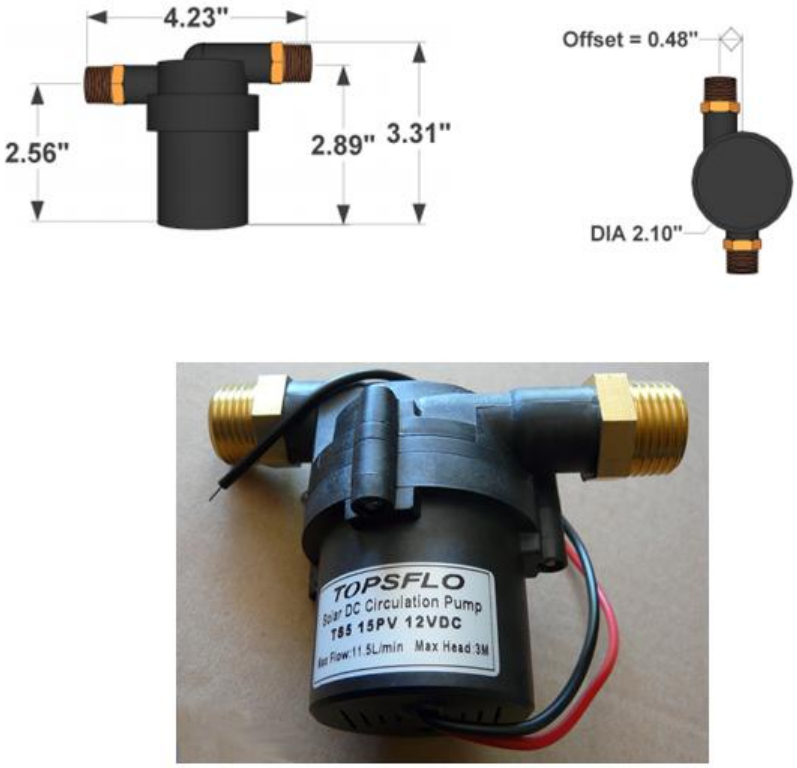

Figure 5.9 Dimensions and picture of the circulation pump

Another key feature is that unlike traditional water pumps, it is seal-less, leading to no leaks during application of high temperatures. In a seal-less magnetic drive pump, the impeller and motor have magnets attached to them. Permanent magnets are attached to the pump's drive assembly. The drive magnet, the magnet responsible for driving the inner rotor, is attached on a second shaft operated by the motor. When the motor turns on, it spins its magnet. The magnetic force from the motor's magnet causes the magnet on the impeller to spin and rotate the impeller. The pump, when powered through a 12V adaptor can operate at pressures up to 800 kPa, temperatures up to 100 ºC and can deliver water at a flow rate up to 3 gallons per minute. Water was used as the circulating fluid in the closed loop system. The properties of water for different temperatures are summarized in Table 5.1.

Table 5.1 Water properties at different temperatures

T (ºC)	Density (×1000 kg/m^3)	Viscosity (Pa-s)	Kinematic Viscosity (m^2/s)	Surface Tension (N/m)	Bulk Modulus (GPa)	Thermal Expansion Coefficient (m/mºC)
0	1.00	1.79E-03	1.79E-06	7.56E-02	1.99	-6.81E-05
4	1.00	1.57E-03	1.57E-06	-	-	-
10	1.00	1.31E-03	1.31E-06	7.42E-02	2.12	8.80E-05
20	1.00	1.00E-03	1.00E-06	7.28E-02	2.21	2.07E-04
30	1.00	7.98E-04	8.01E-07	7.12E-02	2.26	2.94E-04
40	0.99	6.53E-04	6.58E-07	6.96E-02	2.29	3.85E-04
50	0.99	5.47E-04	5.48E-07	6.79E-02	2.29	4.58E-04
60	0.98	4.67E-04	4.75E-07	6.62E-02	2.28	5.23E-04
70	0.98	4.04E-04	4.13E-07	6.64E-02	2.24	5.84E-04
80	0.97	3.55E-04	3.65E-07	6.26E-02	2.20	6.41E-04
90	0.97	3.15E-04	3.26E-07	-	2.14	6.96E-04
100	0.96	2.82E-04	2.94E-07	5.89E-02	2.07	7.50E-04

5.4 Instrumentation

5.4.1 Closed-Loop Heat Exchangers

Three heat exchangers were used to transfer heat to the silt. They are each steel tubes that are bent into a U-shape to form a closed-loop, as shown in Figure 5.10. The tubing has an outside diameter of 6 mm and an inside diameter of 2 mm, and the heat exchanger has a length of 560 mm. The distance between the inlet and outlet pipes is approximately 75 mm. The heat exchangers were placed in the vadose zone (i.e., the unsaturated layer of Bonny silt). Heat is transferred into the soil by circulating hot water through the pipe at a flow rate sufficient to lead to turbulent conditions. Heat is transferred from the outside of the pipe into the soil via conduction, convection due to the movement of water vapor, and by latent heat as the water evaporates into the pores.

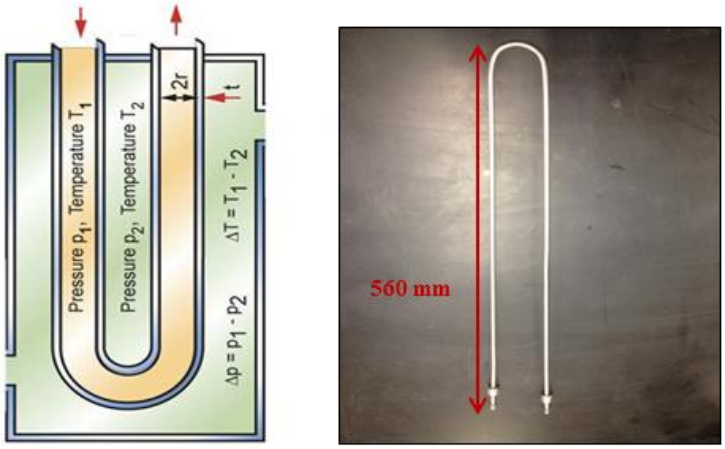

Figure 5.10 Closed loop heat exchanger: (a) Mechanism; (b) Picture

In this experiment, the heat exchange pipes were tentatively placed at equal distances from each other in a triangular array. Experiments were performed for different center-to-center radial distances of the heat exchanger tubes from the center of the container as shown in Figure 5.11. It should be noted that the uppermost sensors shown in this figure is 100 mm below the soil surface.

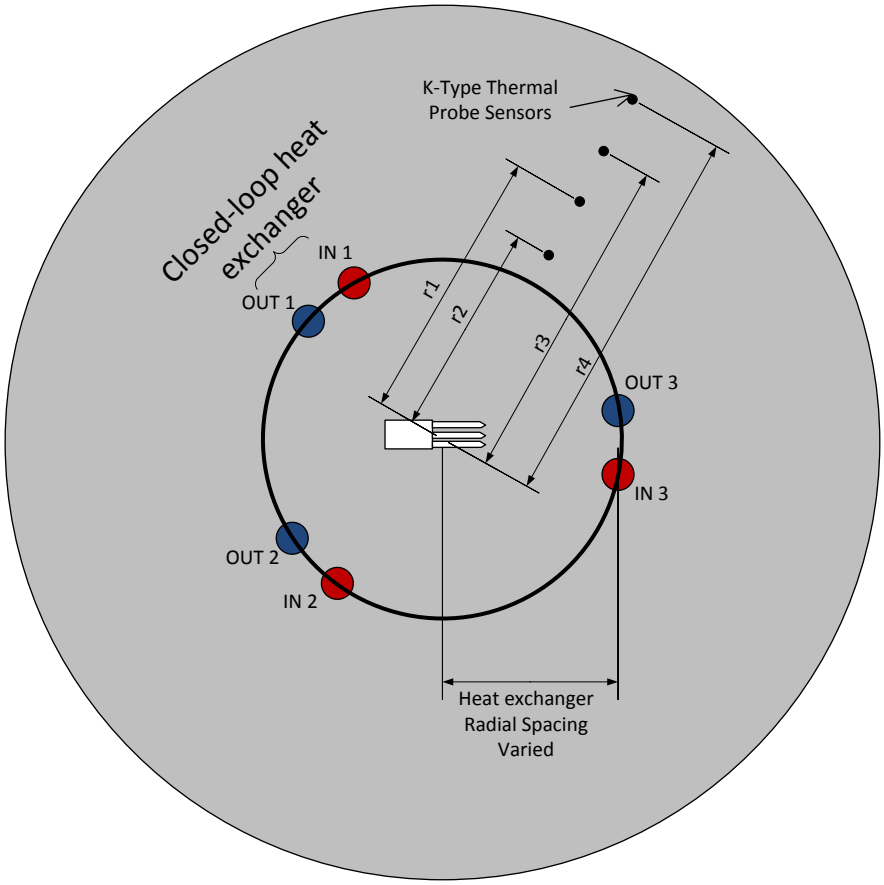

Figure 5.11 Plan view of heat exchanger setup with variables representing general instrumentation locations in the different tests

5.4.2 Dielectric Sensors (Volumetric Water Content and Temperature)

The volumetric water content and temperature of the soil was measured using five 5TE dielectric sensors manufactured by Decagon Devices of Pullman, WA. A picture of the sensors is shown in Figure 5.12. The 5TE sensors are an improvement to the ECH2-TE as they provide more accurate readings by using a 5 point calibration to measure the dielectric permittivity of the soil from the charge time of a capacitor circuit. The dielectric permittivity of the soil is linearly related to the volumetric water content. To measure temperature, the 5TE has a thermistor mounted within the probe body next to the prongs which are in direct contact with the soil. The sensor can also measure the electrical conductivity of the soil, but this was not used in this study.

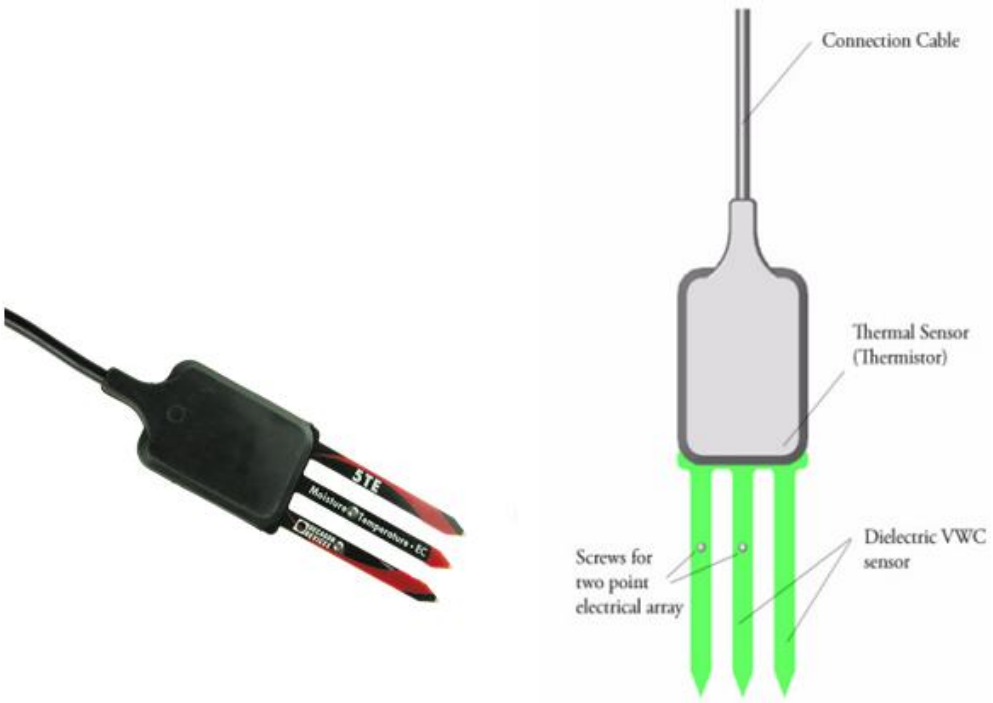

Figure 5.12 Decagon 5TE dielectric sensors with embedded thermistor.

To infer volumetric water content, the 5TE sensors uses an electromagnetic field to measure the dielectric permittivity of the soil. When prompted to take measurements, the sensor sends a 70 MHz oscillating wave to its prong, which in turn produce a charges depending on how dielectric the soil is. When the charge is produced, the soil will store some of this charge. The stored charge is proportional to the soil's volumetric water content and is measured by the 5TE sensor and a dielectric permittivity value is produced. The five 5TE sensors were placed at a uniform spacing of 85 mm with depth at the center line of the soil specimen (Figure 5.1). An ECH20 Em50 data logger from Decagon along with the ECH20 Utility software was used to collect readings from the sensors.

5.4.3 Thermal Conductivity Sensor

The KD2Pro thermal properties analyzer from Decagon Devices of Pullman Washington (Figure 5.13) was used to obtain thermal conductivity, temperature and specific heat data. The

KD2Pro Analyzer consists of a handheld data logger and sensors that can be inserted into subject soil specimen. The logger can be used to take automated measurements at an interval of 15 minutes and is capable of storing 4,095 measurements. The KD2 Pro Analyzer is compatible with three sensors: a 60-mm single-needle (KS-1) sensor, a 100-mm single-needle (TR-1) sensor, and a 30-mm dual-needle (SH-1) sensor. In this experiment, the 30 mm dual-needle (SH-1) sensor was used (Figure 5.13) as it is capable of measuring temperature, volumetric specific heat capacity, and thermal diffusivity. These values can be used to calculate the thermal conductivity or thermal resistivity.

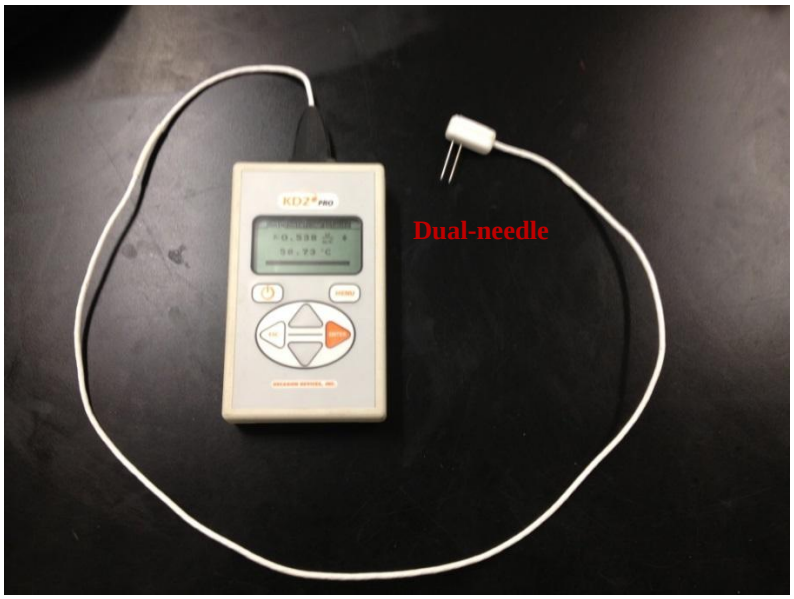

Figure 5.13 KD2Pro thermal properties analyzer.

The principle of the heat-pulse technique is used to measure the thermal conductivity (Kluitenberg et al. 1993). One of the needles contains a heating component and the other, a thermocouple. Energy is supplied to the heating needle in the form of heat, which is then transferred through the Bonny silt between the needles after which it is measured by the thermocouple in the other needle. The single-needle probe for the KD2Pro uses the line source method described by Carslaw and Jaeger (1959) to calculate the thermal conductivity. The line

source method can be used to calculate the thermal conductivity from the change in temperature of the needle when heat is applied at a constant rate. They predicted change in temperature of the line source as a function of time can be defined as follows:

$$T(t, r) = -\frac{Q/L}{4\pi\lambda} Ei\left(-\frac{r^2}{4Dt}\right) \tag{5.1}$$

where λ is the thermal conductivity (W m^{-1} K^{-1}), D is the thermal diffusivity (m^2 s), q = Q/L is the amount of heat applied per unit time and length (J m^{-1} s), t is the time over which heat is applied and r is the distance from the heat source. E_i is the exponential integral, solution of the following integral:

$$-Ei(-x) = \int_x^{\infty} \frac{e^{-t}}{t} dt \cong -0.58 - \ln(x) \tag{5.2}$$

Equation (5.2) can also be represented in a linearized form for small values of r in the following form:

$$-Ei(-x) = 0.58 - \ln(x) \tag{5.3}$$

D and λ can be determined by a non-linear least squares procedure (Marquardt 1963). Alternatively, after inserting Equation (5.3) into Equation (5.1) and taking the derivative with respect to time, the apparent thermal conductivity can be determined as follows:

$$\lambda = \frac{Q}{4\pi L}\left[\frac{dT}{d(\ln t)}\right]^{-1} \tag{5.4}$$

where L is the effective length of each closed-loop heat exchanger. The term $[dT/d(\ln t)]^{-1}$ represents the slope of the change in mean fluid temperature versus logarithmic time. The differential form of the line source equation does not consider the impact of heat capacity of the line source (closed-loop heat exchangers) on the transient heating response; therefore, this slope should be measured over large time intervals (Murphy 2013).

5.4.4 Mariotte Bottle

The Mariotte bottle, invented by Edmé Mariotte, a 17th-century French physicist is a closed vessel that delivers constant rate flow.

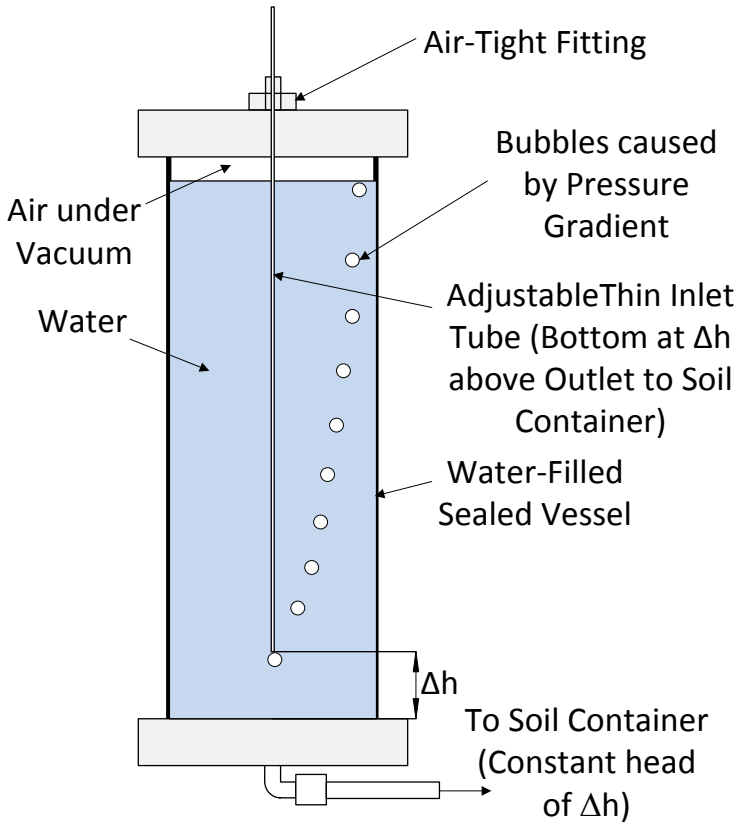

Figure 5.14 Mariotte bottle and mechanism

In this experiment, the Mariotte bottle (Figure 5.14) is a closed container with an exit hole at the bottom to supply water to the sand. The top of the vessel is sealed and had a fitting through which a thin tube is inserted. The fitting also permits the location of the bottom of the tube to be adjusted. The top of the thin tube is open to atmospheric pressure, which implies that the the bottom end of the tube must also be at atmospheric pressure if bubbles of air move from the thin tube into the vessel. The principle behind the Mariotte bottle is that when it is full of water and the inlet tube is lifted above the exit hole by Δh, the pressure at the exit hole is greater than atmospheric pressure by $\rho g \Delta h$. That causes water to flow out of the exit hole at a constant rate. As soon as water begins

flowing out of the exit hole, the pressure inside the vessel decreases, causing the pressure at the bottom of the inlet tube to fall below atmospheric pressure. This causes air to enter the tube and form bubbles, keeping the pressure at the bottom of the tube at atmospheric pressure. As long as the level of water inside the cylinder is above the bottom of the inlet tube, the pressure at the exit hole will remain constant at $\rho g \Delta h$. The air that enters the system forms bubbles at the bottom of the tube to the air at the top of the cylinder, as shown in Figure 5.14. This is very important because when saturating the sand, as the water level should always stay at the top of the sand layer.

6. PROCEDURES

6.1 Soil Placement Conditions

6.1.1 Preparation of the Physical Model

The first step before testing was to moisture condition the silt to a gravimetric water content of approximately 22% by mixing it with a shovel while spraying a fine mist of water using a pressurized spray bottle. After adding the required amount of water, the loose, moist silt was placed into a pair of sealed drums for at least 24 hours for the water content to homogenize. Before starting compaction, four samples of the moisture-conditioned silt were oven-dried to determine the average gravimetric water content, which was used to determine the total density of the specimen corresponding to the target dry density of 1400 kg/m^3. The total density of the specimen is crucial as the mass of soil necessary per lift can be estimated to reach the target compaction conditions. The projected lift levels were marked on at four locations on the inside of the container (Figure 6.1). The levels where the dielectric sensors and thermal conductivity sensors were to be placed were also marked on the tape. A schedule of the lift levels used for compaction including the depths of the dielectric sensors in the different physical models is shown in Table 6.1.

Table 6.1 Arrangement of sensors in the physical model (Note: all sensors are located at the center of the container)

Sensor depth from top (mm)	Type of Sensor
440	5TE (Temperature & Volumetric water content)
355	5TE (Temperature & Volumetric Water Content)
270	5TE (Temperature & Volumetric Water Content)
244	SH-1 (Temperature & Thermal Conductivity)
185	5TE (Temperature & Volumetric Water Content)
100	5TE (Temperature & Volumetric Water Content)

Figure 6.1 Experimental container with sensor level markings

6.1.2 Sand Pluviation

The holes at the bottom of the container used for supply of water to the sand layer were first covered with filter paper. This allowed for the holes to remain unclogged with sand during testing, especially when vacuum was applied to de-air the sand layer. The sand layer was placed by dry pluviation. Sand was poured continuously into the container from a height of approximately 700 mm above the soil surface height to reach a relative density of approximately 60%. The sand was placed in two lifts having thicknesses of 31 mm. Although careful control of the density of the sand layer is not particularly important for the results of this study, the density was checked so that the hydraulic conductivity could be assumed from the results of previous experimental studies. At each sand lift, the sides of the container were hit with a hammer and the container was hit against the ground in order to achieve maximum density of the sand layer. A ruler was used to level the surface of the sand. A thin layer of filter fabric was placed over the surface of the sand to prevent its mixing with the overlying silt layer.

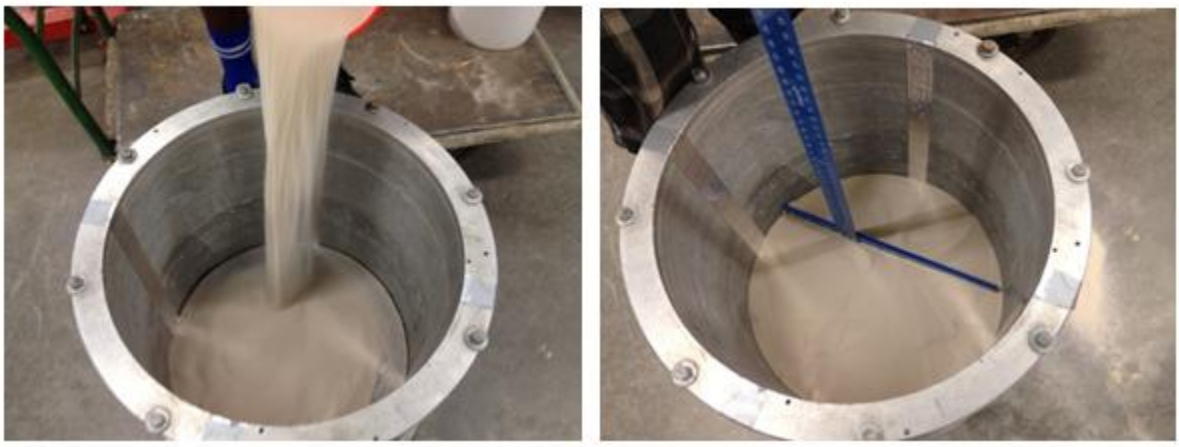

Figure 6.2 Sand Placement in experimental container

6.1.3 Placement of Silt

The center of the container was marked. The perimeter of the container was calculated and divided by three to determine the balanced positions of the closed-loop heat exchangers. They were also tentatively placed equally at different radial distances in each of the tests. While two people held the three closed-loop heat exchangers in to their proper positions, half a lift of silt was poured and compacted to lock the heat exchangers into position. They were held so that the flat portion of the "U" faced the middle of the container. An 80 kg cylindrical rod was used to compact the silt to approximately 93%. Compaction was performed at every half lift (i.e. each 13.6 kg of silt) to ensure uniformity of density. To compact the soil, the cylindrical rod was raised approximately 80 mm and then dropped on the silt. The edges were first compacted then the middle area. After reaching each lift, the level of the soil surface was verified to ensure that it matched the marked intended levels for each lift. The schedule used for compaction of the silt lifts in the container is shown in Table 6.2.

Table 6.2 Typical compaction details for the silt layer

Lift number	Thickness (mm)	Depth from soil surface (mm)	Mass of soil (kg)
Sand	62	491.7	26.9
1	61	431	27.2
2	61	370	27.2
3	61	309	27.2
4	61	248	27.2
5	61	187	27.2
6	61	126	27.2
7	61	65	27.2
8	61	3.7	27.2
Total specimen height (mm)	550		
Total specimen mass (kg)	245		

Figure 6.3(a) Compacting rod, (b) Compaction of silt layer, (c) 5TE dielectric sensor placement

Each dielectric sensor was placed at the depths shown in Table 6.1. Soil was compacted to slightly below the level of the sensor. Loose soil was placed a little above the intended dielectric sensor height upon which the sensor was put (in the middle of the container) and covered with more soil before compaction. The latter technique was done to provide some cushion for the dielectric sensor during compaction and avoid damaging it. In the same regards, compaction around the sensor needs to be done very gently. Soil samples were taken from the surroundings of each 5TE dielectric sensors then oven-dried to obtain the volumetric water content. The measured volumetric water contents were then plotted against the readings from the 5TE dielectric sensors to develop a soil-specific calibration. The calibration curve used for the sensors is shown in Figure 5.4. Further work may be required to define a calibration curve for each sensor.

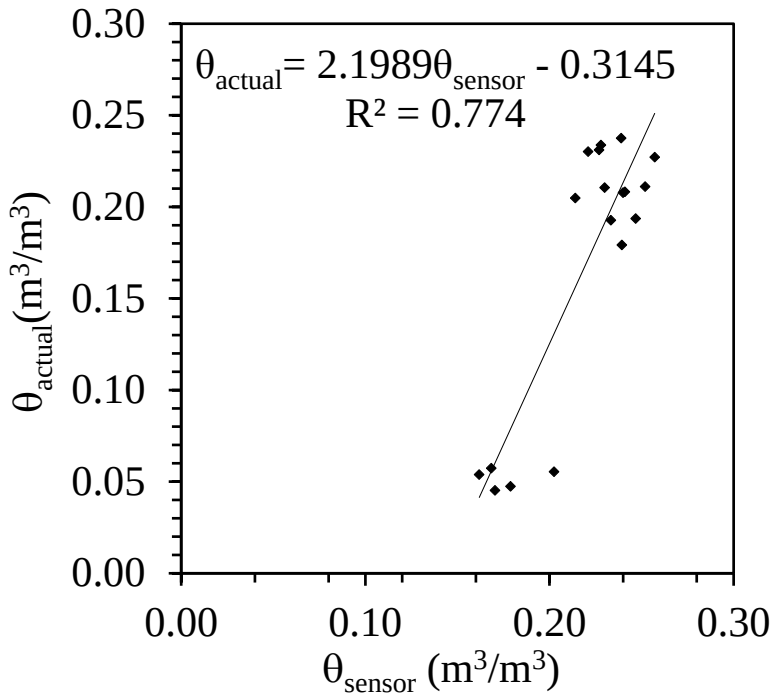

Figure 6.4 Volumetric water content calibration for the dielectric sensors

The dielectric sensors were placed at a vertical spacing of 85 mm apart along radial center of the soil layer. The thermal conductivity sensor was placed at mid-height of the silt layer at in the center of the container, next to the middle dielectric sensor. To obtain accurate readings, it was

important to make sure that the needles of the SH-1 sensor were inserted straight into the silt and parallel to each other. After all the lifts and sensors were placed, aluminum foil heat insulation was used to insulate the container on the top and sides. That was intended to minimize the effect of outside temperature and reduce heat loss from the sides of the container. The top of the soil specimen was also covered with several layers of saran wrap to minimize loss of water to the laboratory air due to evaporation during the experiment. The bottom of the container was left un-insulated, as heat loss was expected from this zone of soil.

The four K-type thermocouples profile probes were pushed into the silt layer after compaction of all of the soil lifts and placement of the insulation were completed. Before pushing the probes into the soil layer, holes were predrilled to facilitate insertion and to avoid bending. The probes were located at different distances from the heat exchangers, and were installed at different locations in each test as summarized in the next chapter. The depths of the sensors were consistent as shown in Figure 5.11. As mentioned earlier, the uppermost sensor was placed 100 mm below the soil surface. More plastic wrap was wrapped around the cables to minimize the chance for preferential pathways for water vapor to escape the system.

6.2 Sand Saturation

The Mariotte bottle was filled with water then connected to one of the bottom holes of the container. The thin inlet tube was kept at 62 mm above the bottom plate of the container (which is the height of the sand layer). This was done to ensure that the water level stays always at the sand level. applied vacuum of -57 kPa was applied to another of the ports in the base of the container opposite from the Mariotte bottle, and water was permitted to flow from the Mariotte bottle through the sand layer toward this port. After water exited from the port connected to vacuum, it was assumed that the sand layer was saturated with water. After this point, the Mariotte bottle was

filled with water and the level of the inlet tube was set to the top of the sand layer. This permits the water table (i.e., zero pressure head) to be maintained at the top of the sand layer. Throughout the experiment, the Mariotte bottle was refilled several times to ensure that the sand was always saturated.

6.3 Heating Procedures

A four-way splitter was used to supply an equal amount of the heated water to the three closed loop heat exchange pipes. Another four-way splitter was used to collect the outflow from the tubes and return it to the pressure cell. All of the tubing outside of the soil layer was insulated to minimize heat loss.

The pressure cell was filled with de-aired water and was then pressurized to 150 kPa using a water-filled tank. The circulation pump was turned on and water was circulated through the closed-loop heat exchange tubes under room temperature. While the system was running, the valve at the top of the pressure cell was opened to flush air from the tubes and the pressure cell. When water with no bubbles came out of the pressure cell, the valve was closed. It was important to make sure at that point that the pump was working properly (i.e. to make sure that there were no entrapped air bubbles in the pump). Air bubbles were observed to cause the pump to run noisily, and an embedded sensor in the pump stops its operation automatically if air is detected. The initial circulation approach at room temperature was also used to ensure that there were no water leaks.

The temperature and volumetric water content data from the dielectric sensors were acquired using an Em50 data logger. The ECH20 utility was used to first erase all previously recorded data, then was set to acquire data at an interval of one minute. The KD2Pro was programmed to record the thermal conductivity from the thermal conductivity probe every 15 minutes. All thermocouples profile probes and the fluid inlet/outlet temperatures were set to record

data every second using a program written in LabView. With the pump running properly and all the data acquisition apparatus set to record, the water heater was turned on to a temperature of 70 ºC. Pictures of the assembled test are shown in Figure 6.5.

Figure 6.5 Pictures of the assembled experimental container in a typical test

7. RESULTS

7.1 Scope of Testing

Several heat storage tests were performed on compacted layers of unsaturated Bonny silt that were underlain by a saturated layer of Nevada sand. The goal of these tests was to characterize the coupled flow of water and heat in the unsaturated soil between an array of borehole heat exchangers having different spacings from the center of the container. The spacings for the closed-loop borehole heat exchanger arrays from the center of the container were 80 mm, 160 mm, 300 mm, 150 mm and 100 mm. The 5TE dielectric sensors and the SH-1 thermal conductivity sensor were placed at the same depths in all tests (see Table 6.1). However, the radial locations of the thermocouple profile probes was different in each test in order to understand the role of different geometries of the borehole array. A summary of the radial distances of the closed loop heat exchanger tubes and the thermal sensor probes in each test is also shown in Table 7.1. The initial soil conditions in the tests were similar. Profiles of the initial volumetric water contents obtained from oven-dried samples in four of the tests are shown in Figure 7.1.

Table 7.1 Scope of testing in the four physical modeling tests

Test	Dry density (kg/m^3)	Initial volumetric water content (m^3/m^3)	Initial degree of saturation	Void ratio	Borehole array spacing	Radial spacing of thermal probes			
						r_1	r_2	r_3	r_4
Test 1	1400	0.236	0.4	0.9	100	110	160	210	260
Test 2	1400	0.231	0.4	0.9	160	160	200	240	280
Test 3	1400	0.233	0.4	0.9	300	300	250	200	150
Test 4	1400	0.236	0.4	0.9	150	163	177	193	235
Test 5	1715	0.222	0.6	0.5	100	-	-	-	-

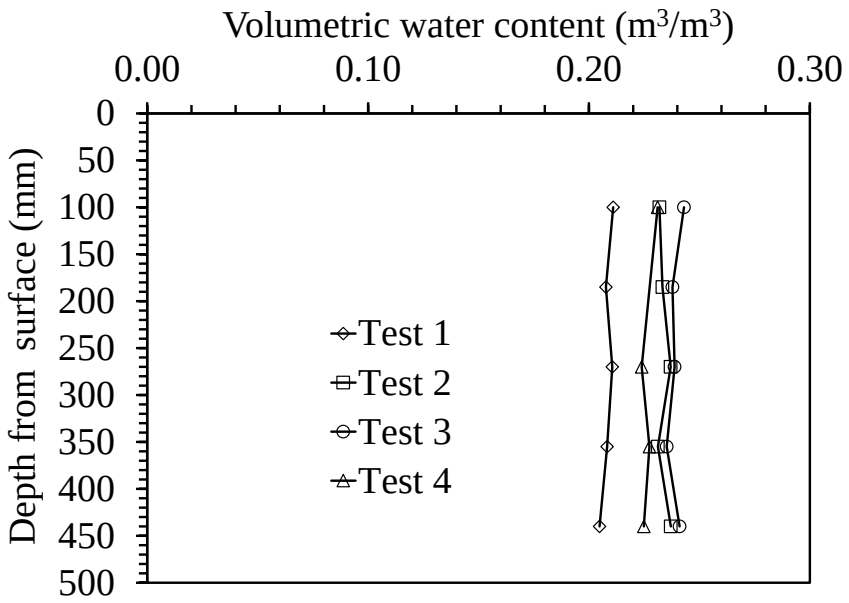

Figure 7.1 Profiles of initial volumetric water content after compaction for Tests 1-4

7.2 Test 1

This test was performed to assess the changes in volumetric water content and temperature within the unsaturated zone of soil within a borehole heat exchanger having radial spacing of 80 mm from the center of the container. The results were used to characterize the transfer mechanisms involved with coupled heat and water flow in the vadose zone. Insulation was placed over the saran wrap hydraulic barrier to help minimize loss of heat from the soil surface. The flow rate of water circulating through the borehole heat exchangers was measured to be 7 mL/s, and was assumed to be steady throughout the test. The temperature of the water entering the borehole heat exchangers was approximately 85 ºC, while the temperature of the fluid exiting the heat exchangers was approximately 79 ºC, as shown in Figure 7.2.

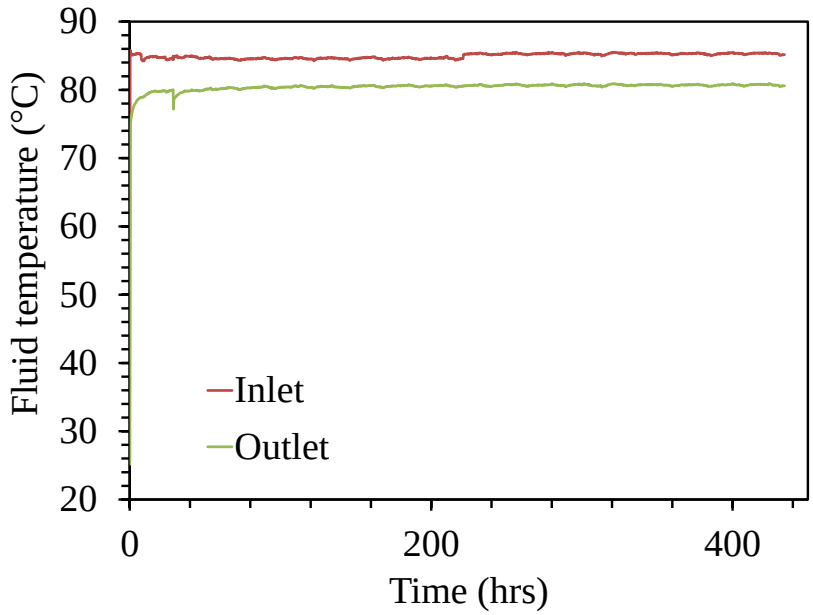

Figure 7.2 Inlet and outlet heat exchange fluid temperatures in Test 1

The difference between the inlet and outlet fluid temperatures along with the mass flow rate and properties of water can be used to calculate the thermal energy input (power) into the system, as follows:

$$\dot{q} = h(T_{in} - T_{out}) \tag{7.1}$$

where T_{in} and T_{out} are the temperatures of the water entering and exiting the heat exchanger loops, respectively, and h is the entropy drift, which can be calculated as follows:

$$h = \dot{m}C \tag{7.2}$$

where C is the specific heat capacity of water, equal to 4183 J kg^{-1} K^{-1}, and $\dot{m}$ is the mass flow rate, which can be calculated as follows:

$$\dot{m} = \dot{V}\rho \tag{7.3}$$

where $\dot{V}$ (mL/s) is the volumetric flow rate (the volume of water supplied by the pump to the heat exchangers per unit time) and ρ is the water density (1 g/mL). By combining Equations (7.1),

(7.2), and (7.3), the expression used to calculate the thermal energy input (power) into the system is as follows:

$$\dot{Q} = \dot{V}\rho \, C \, (T_{in} - T_{out}) \quad (7.4)$$

The value of $\dot{Q}$ calculated from the data in Figure 7.2 is relatively constant through the test, and is equivalent to an average of 132 W of energy input into the unsaturated soil layer during the course of the experiment. The results indicate that the power input into the system was relatively steady as a function of time. The volume of water supplied to the sand layer to maintain a water level at the top of the saturated sand layer was equal to 3 L, which was absorbed at a relatively steady pace over the course of the 435 hours of testing.

7.2.1 Time Series of Temperature, Water Content, and Soil Properties

A comparison of temperatures and humidity at the surface of the soil with that of the laboratory is shown in Figures 7.3 and 7.4. Ambient temperature and humidity oscillate in a relatively constant pattern while the temperature and relative humidity at the surface of the soil layer reach values of 50 ºC and 70%, respectively, within 10 hours. The temperatures of the soil at the depths of the five 5TE sensors are shown in Figure 7.5(a), while the change in temperature is shown in Figure 7.5(b). The bottom and top of the vadose zone show the lowest temperatures. The highest temperatures are observed at mid-height in the unsaturated soil layer. Temperatures are relatively stable after approximately 30 hours of operation. The average temperatures with depth from each of the thermocouple profile probes installed at different radial distances from one of the heat exchangers are shown in Figure 7.6. As expected, the thermocouple profile probes indicate that temperatures of the soil are lower as the radial distance from the heat exchangers increases.

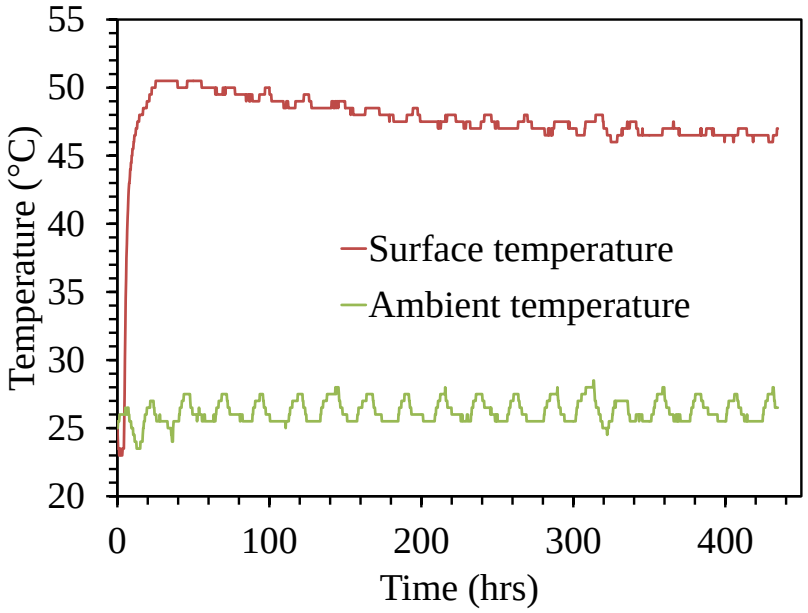

Figure 7.3 Temperatures at the soil surface (under the hydraulic barrier) and in the laboratory for Test 1

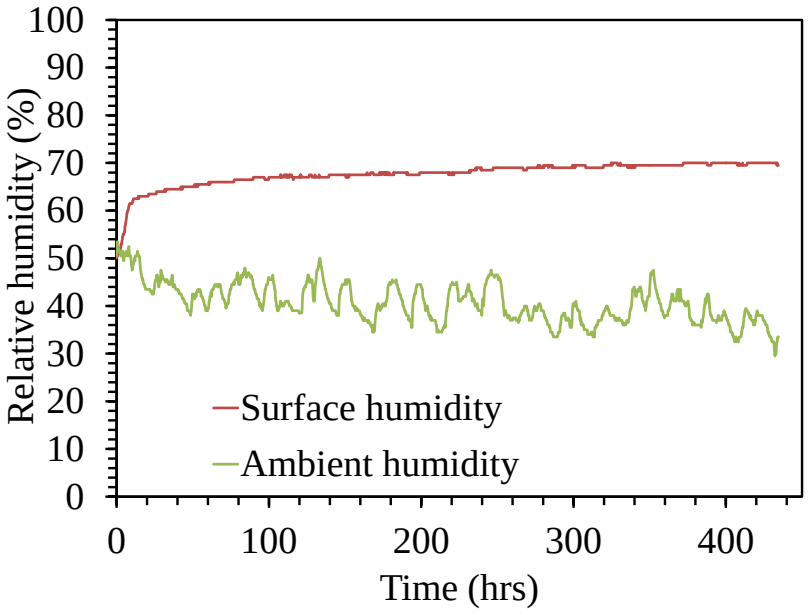

Figure 7.4 Relative humidities at the soil surface (under the hydraulic barrier) and in the laboratory for Test 1

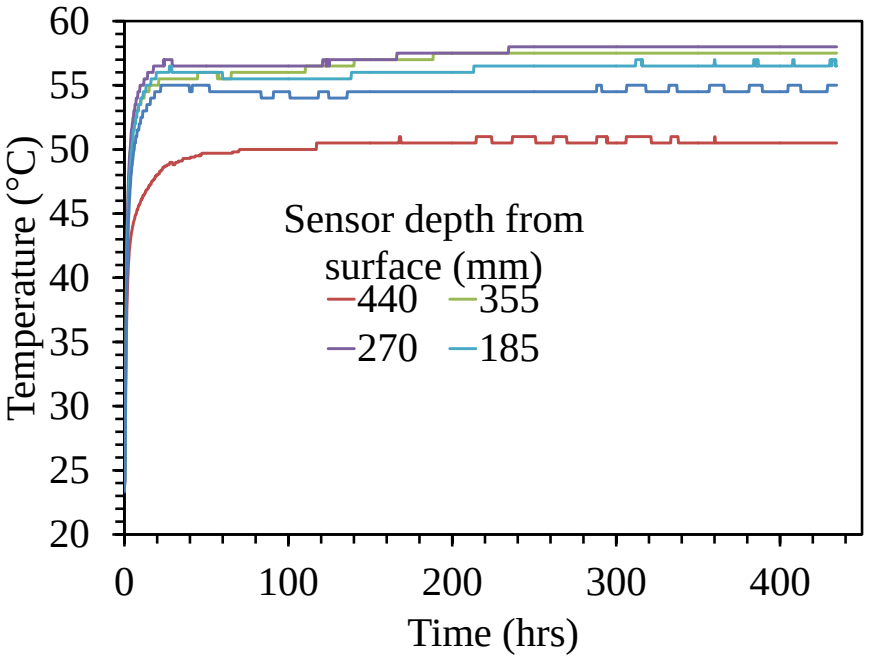

(a)

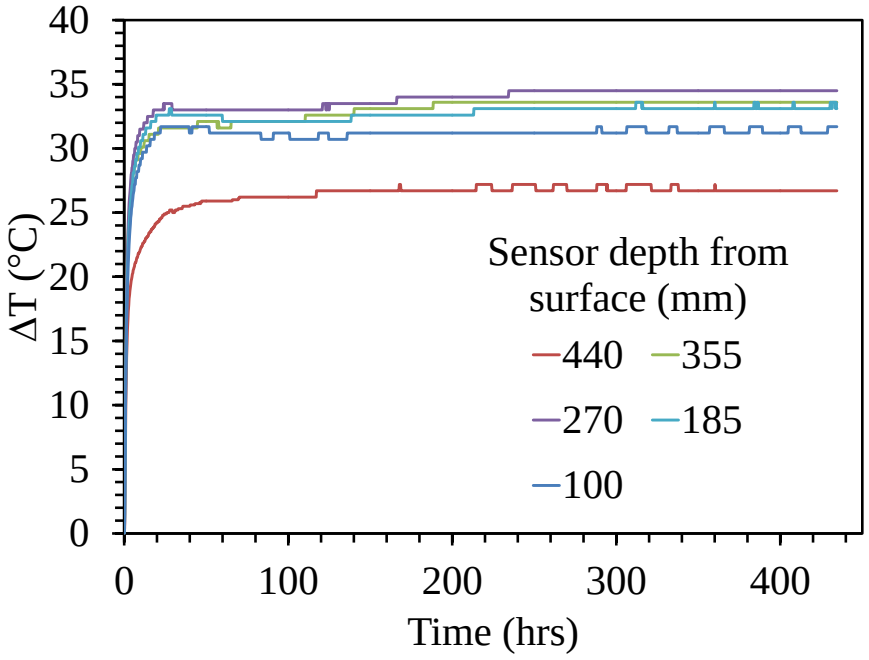

(b)

Figure 7.5 Time series data over time in Test 1from the dielectric sensors embedded at the center of the soil layer (a) Temperature; (b) Change in temperature

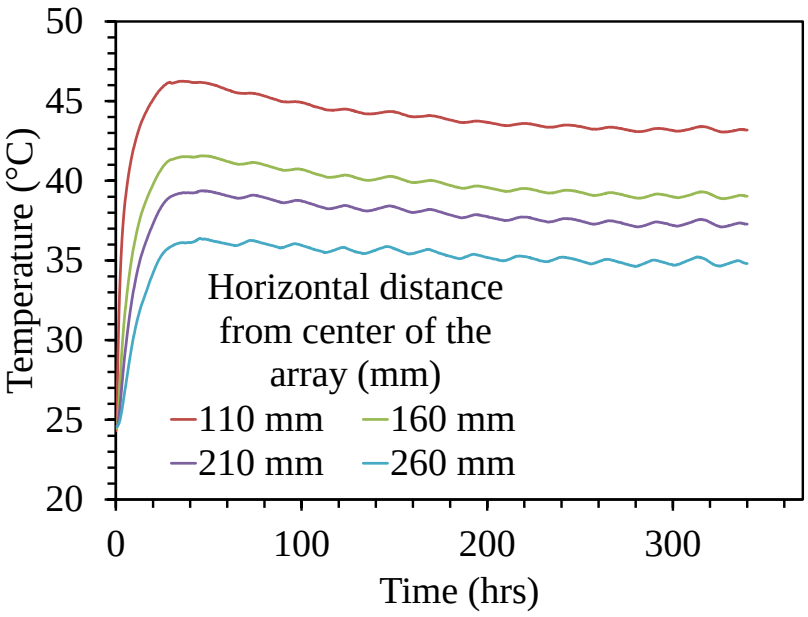

Figure 7.6 Average soil temperature with depth at four different horizontal distances from the center of the borehole heat exchanger array in Test 1

Time series of the volumetric water content and the change in volumetric water content are shown in Figures 7.7(a) and 7.7(b), respectively. The initial volumetric water content of each sensor was found to vary slightly (potentially due to sensor difference, but also potentially due to compaction variability), but the slope of their calibration curves were all assumed to be similar. The change in volumetric water content is thus a better representation of the flow processes occurring in the soil layer that initially had the same compaction water content.

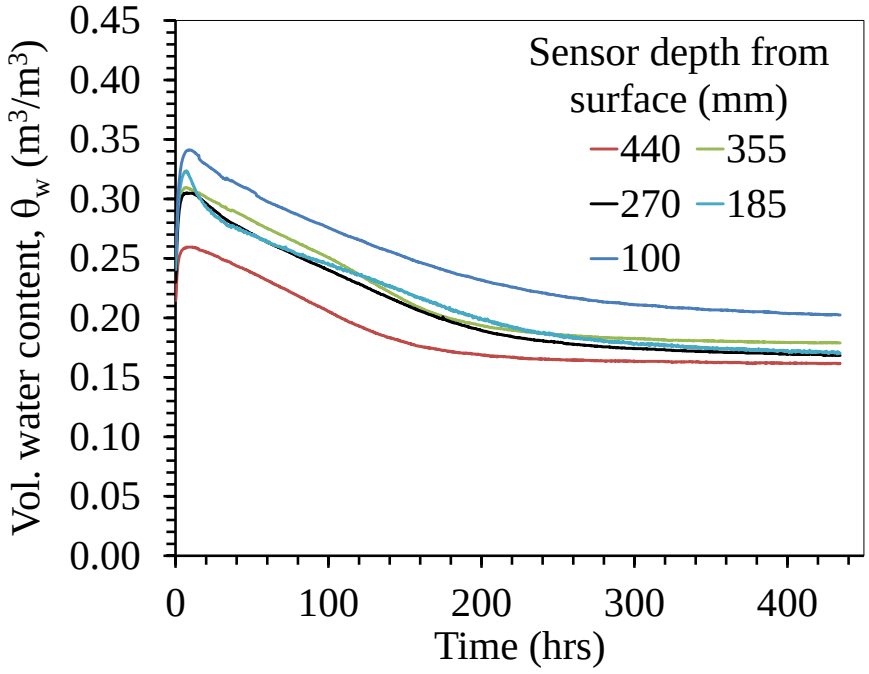

(a)

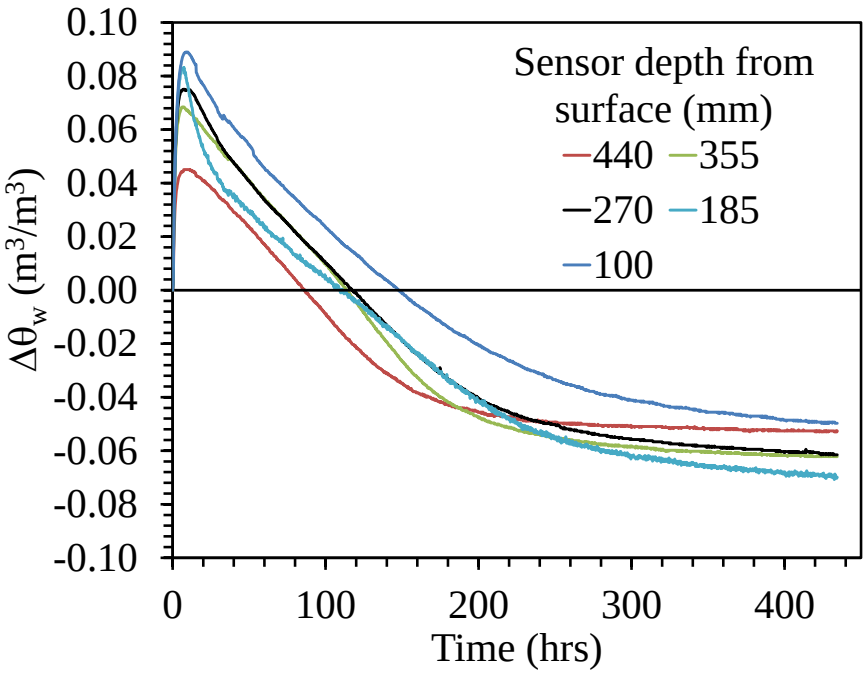

(b)

Figure 7.7 Time series data from the dielectric sensors embedded at different depths in Test 1: (a) Volumetric water content; (b) Change in volumetric water content

The degree of saturation calculated from the change in volumetric water content was calculated as $\Delta S = S_0 - \Delta\theta/n$, where S_0 is the initial degree of saturation and n is the porosity of the soil, and is shown in Figure 7.8. The data in Figures 7.7 and 7.8 show the same behavior at all

depths. Initially, a rapid increase in water content is observed, quickly followed by a slow decrease over time. The values of volumetric water content and degree of saturation at the end of the test (435 hours) were lower than their initial values for this heat exchanger spacing. The highest values of volumetric water content and degree of saturation were observed at the top of the silt layer while the lowest values were observed at the bottom. This observation indicates that the water near the heat exchangers vaporized, toward the dielectric sensors at the center of the array, and then moved upward. Condensation was clearly observed to occur at the underside of the hydraulic barrier at the soil surface. However, the results indicate that capillarity and gravity were not sufficient to cause the condensed liquid water to fall back down into the soil layer and rewet the soil at the center of the array.

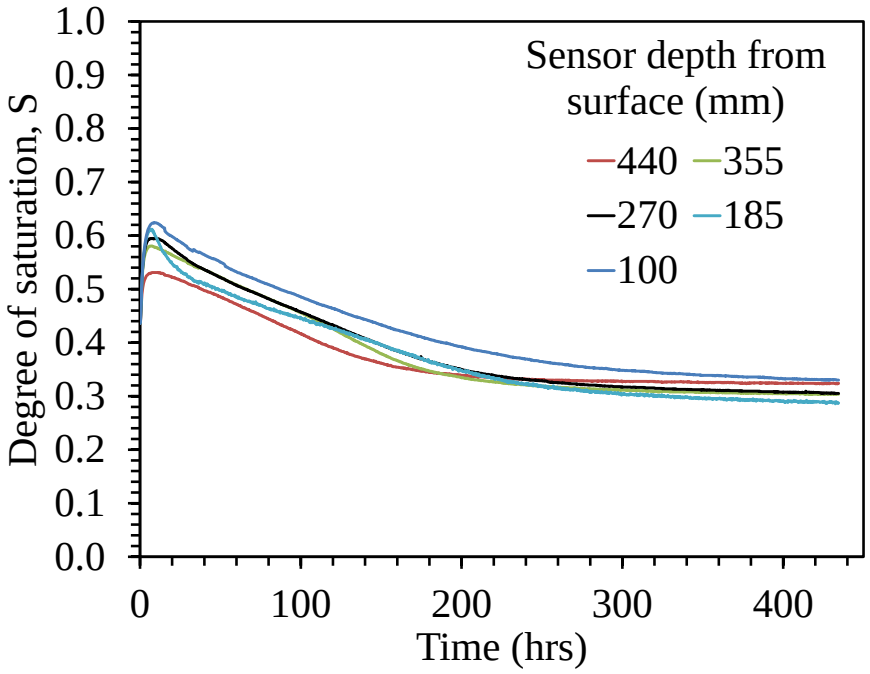

Figure 7.8 Time series data from dielectric sensors in Test 1: Degree of saturation at different depths in the center of the soil layer

The thermal conductivity of the unsaturated soil at the center of the profile is shown in Figure 7.9. For a brief time interval, the thermal conductivity was observed to increase up to a

certain point that corresponded to the peak in volumetric water content. After this point, the apparent thermal conductivity was observed to decrease slowly to a value of approximately 0.55 W/mK. The specific heat capacity does not increase during the initial wetting of the soil, but increases slightly after the volumetric water content starts to decrease, then decreases to an asymptotic value of 1.5 MJ/m^{3}K after 435 hours of heating. These values represent the steady-state apparent thermal properties similar to those shown in Figure 1.4. Unfortunately, they were not higher than the initial apparent thermal properties for this borehole heat exchanger spacing.

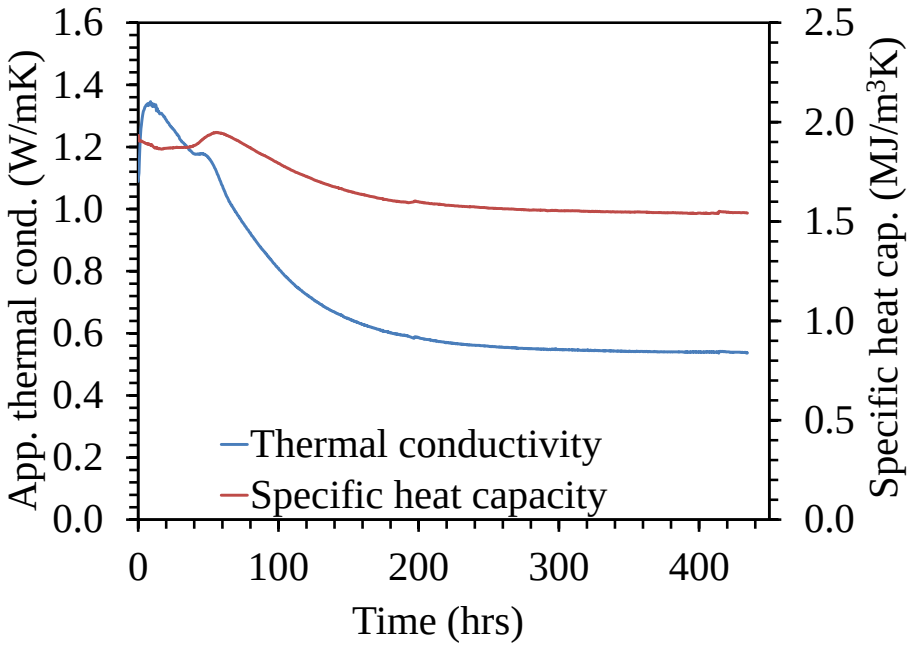

Figure 7.9 Time series data from SH-1 sensor embedded in the middle of the unsaturated soil layer in Test 1: Thermal conductivity and specific heat

A post-test profile section of the unsaturated silt layer is shown in Figure 7.10. The water in the center of the array was observed to move outside of the array into the surrounding soil, visibly drying the soil within the array (lighter) and wetting the soil outside of the array (darker). This figure confirms that the array needs to be large enough to cause thermally induced water flow to enhance heat transfer, and not so small that water can be driven from the array.

Figure 7.10 Post-test profile section of the unsaturated silt layer showing the drying zone within the heat exchanger array in Test 1

7.2.2 Profiles of Temperature and Volumetric Water Content

The profiles of temperature and change in temperature for Test 1 are shown in Figure 7.11(a) and 7.11(b). The temperature is observed to reach a maximum value of approximately 58 °C after about 30 hours then remains constant for the remainder of the experiment. Temperatures are highest at mid-height in the unsaturated soil layer and are lowest in the upper region of the soil layer due to heat loss from the surface. Profiles of the change in water content and degree of saturation are shown in Figures 7.12(a) and 7.12(b). The volumetric water content increases rapidly at all depths, with the silt near the surface being wetter than the silt near the water table at the base of the silt layer. This reflects upward water vapor movement during the heating process. The soil layer is then observed to decrease in water content over time, after which it is nearly uniform with a degree of saturation of about 0.3. A comparison of the initial and final water content profiles is shown in Figure 7.13, and a uniform decrease in water content was observed with depth.

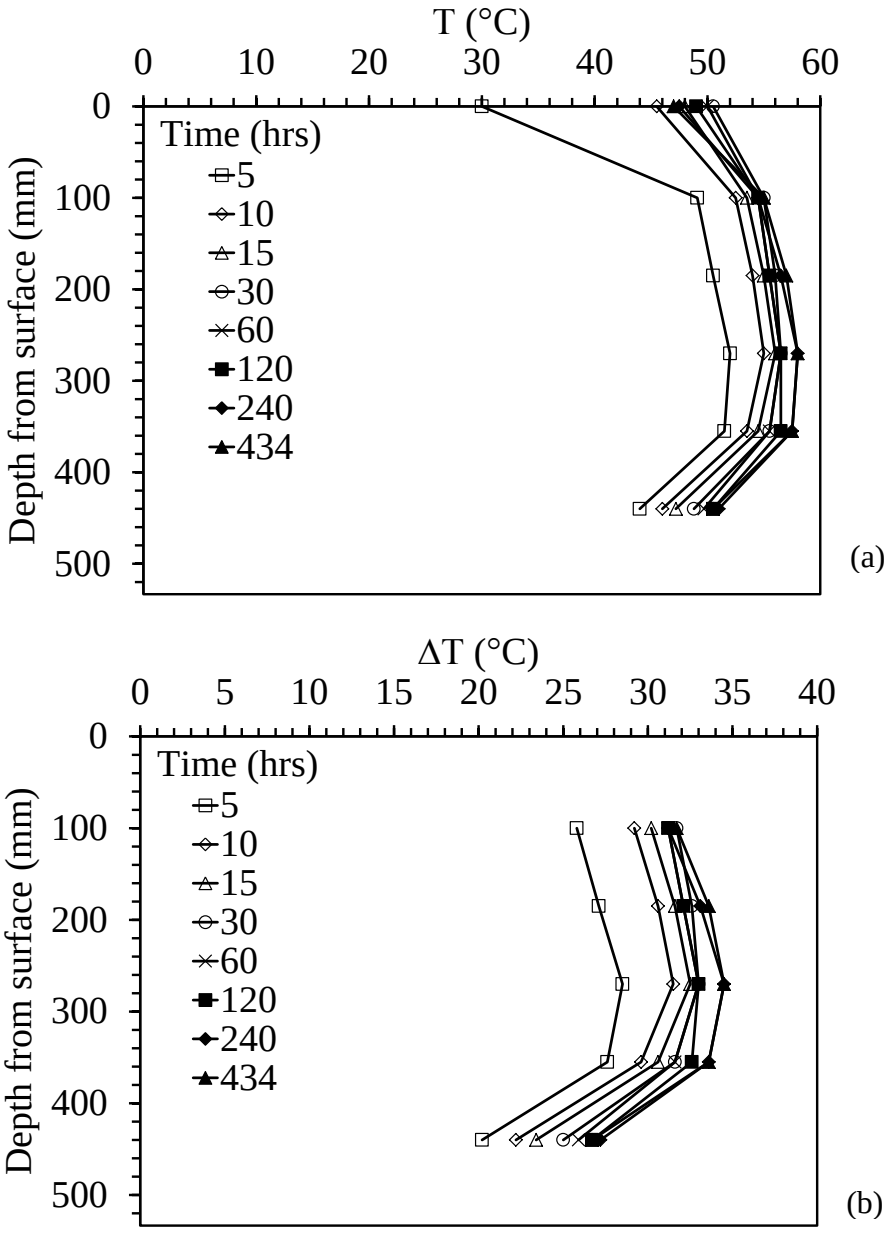

Figure 7.11 Dielectric sensor profiles for Test 1: (a) Temperatures; (b) Change in temperatures

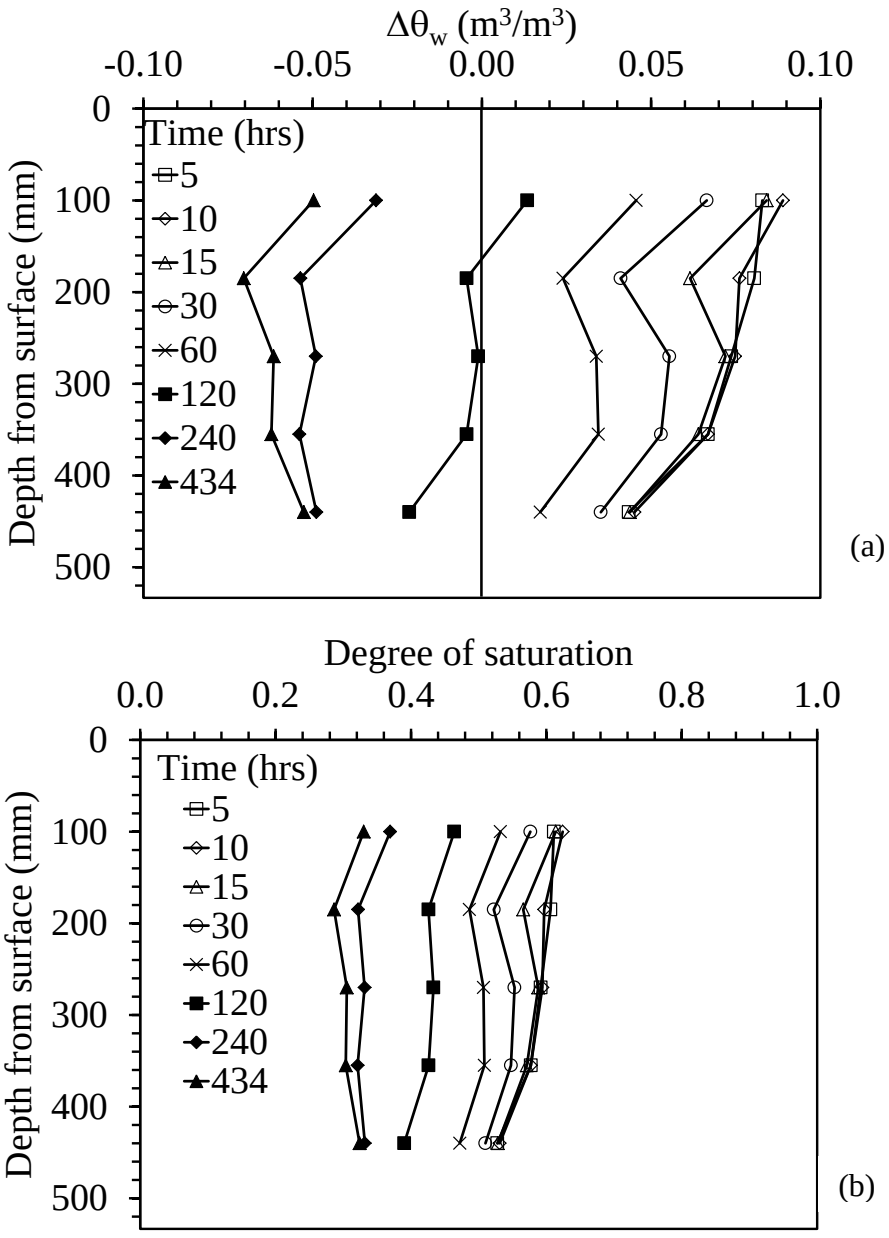

Figure 7.12 Dielectric sensor profiles for Test 1: (a) Change in volumetric water content; (b) Degree of saturation

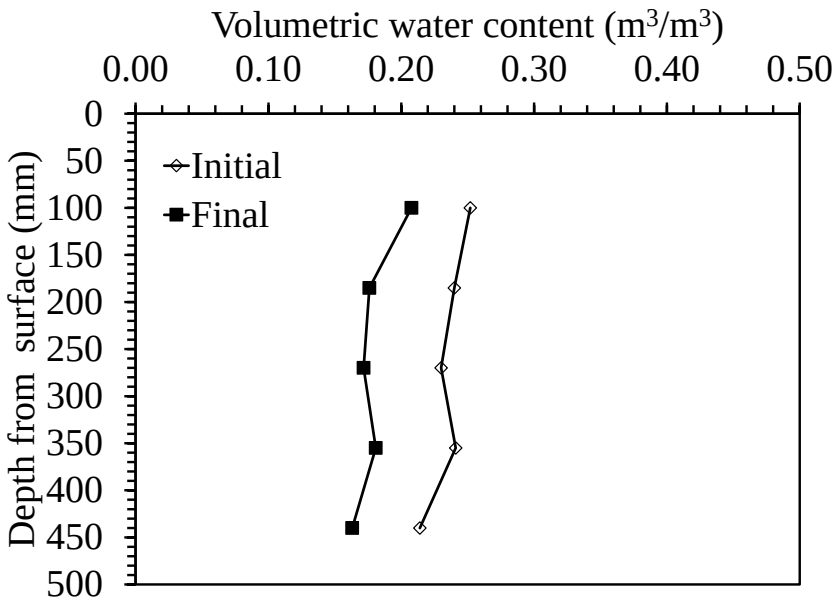

Figure 7.13 Dielectric sensor profiles for Test 1: Initial and final volumetric water contents

7.3 Test 2

This test was performed to assess the changes in volumetric water content and temperature within the unsaturated zone of soil within a borehole heat exchanger array having a radial spacing of 160 mm from the center of the container. The temperature of water entering the borehole heat exchangers was approximately 85 ºC, while the temperature of water exiting the heat exchangers was approximately 77 ºC, as shown in Figure 7.14. The experiment was stopped at 420 hours even though there were still minor changes in material properties. Heated water was supplied to the heat exchangers at a flow rate of 12 mL/s. Using Equation (7.4), this flow rate and the temperature difference of the fluid entering and exiting the heat exchangers corresponds to an average of 470 W of energy input to the unsaturated soil layer. The volume of water supplied to the sand layer to maintain a water pressure at the top of the system was equal to 6 L, which was absorbed at a relatively steady pace over the course of the 420 hours of testing.

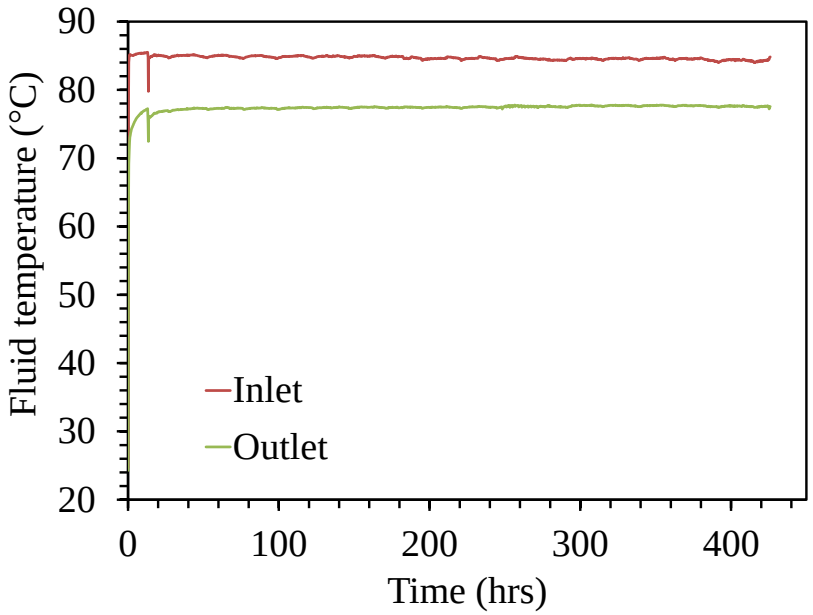

Figure 7.14 Inlet and outlet heat exchange fluid temperatures in Test 2

7.3.1 Time Series of Temperatures, Water Content and Soil Properties

Temperatures and humidity at the surface of the soil and that of the experimental environment are compared in Figures 7.15 and 7.16. Insulation was placed over the hydraulic barrier so only slight oscillations in the room temperature were observed to affect the soil surface temperatures. Room temperature and humidity oscillates in a relatively constant pattern while at the surface of the soil the temperature and humidity reach values of 45 ºC and 70%, respectively within 30 hours.

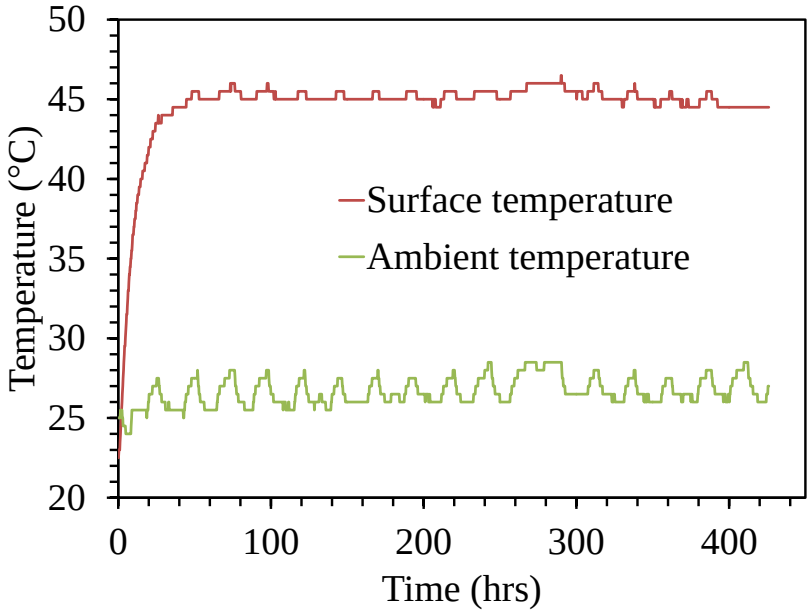

Figure 7.15 Temperatures at the soil surface (under hydraulic barrier) and in the laboratory for Test 2

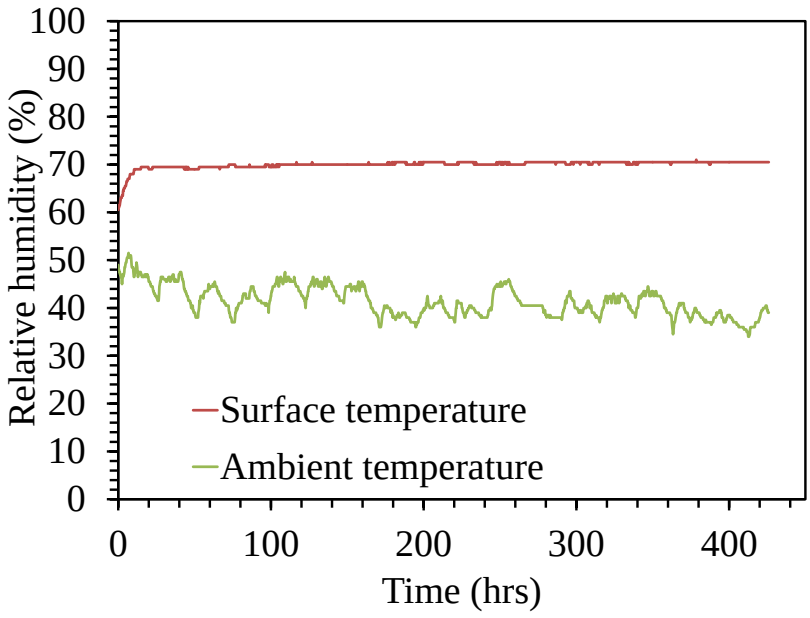

Figure 7.16 Relative humidities at the soil surface (under hydraulic barrier) and in the laboratory for Test 2

Time series of the temperature and change in temperature measured using the four functional dielectric sensors are shown in Figures 7.17(a) and 7.17(b), respectively. The soil was observed to increase in temperature until approximately 50 hours, after which it stabilizes at all

depths. The top section of the unsaturated soil layer (e.g., at depths of 270, 185 and 100 mm) has the highest temperatures while the bottom section (e.g., at depths of 440 and 355 mm) show the lowest.

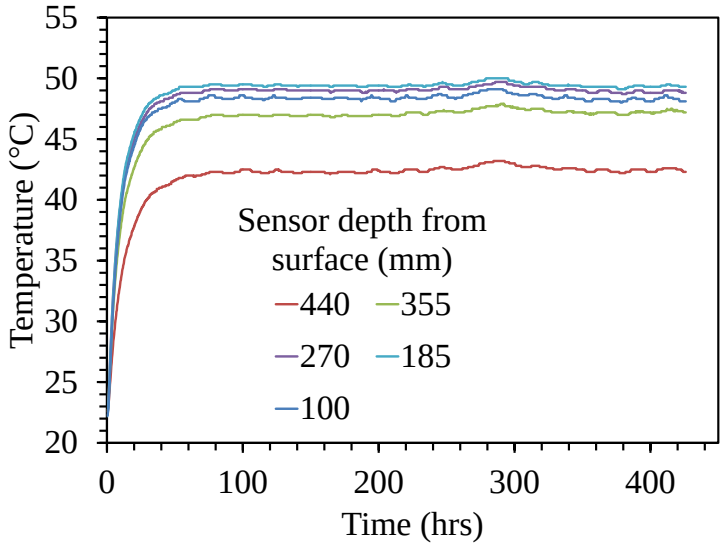

(a)

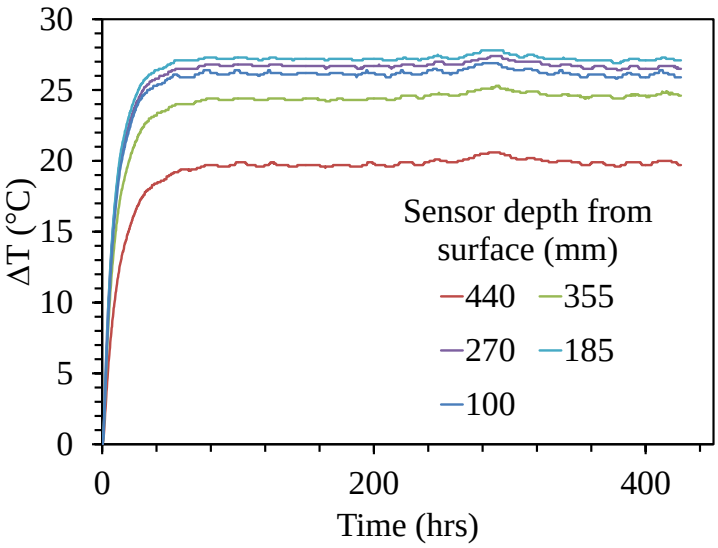

(b)

Figure 7.17 Temperature data over time in Test 2 from the dielectric sensors embedded at the center of the soil layer (a) Temperature; (b) Change in temperature

The average temperatures from the 6 sensors in each of the thermocouple profile probes are shown in Figure 7.18. As expected, the thermocouple probes indicate that temperatures are lower as the distance between the probes and the borehole array increases.

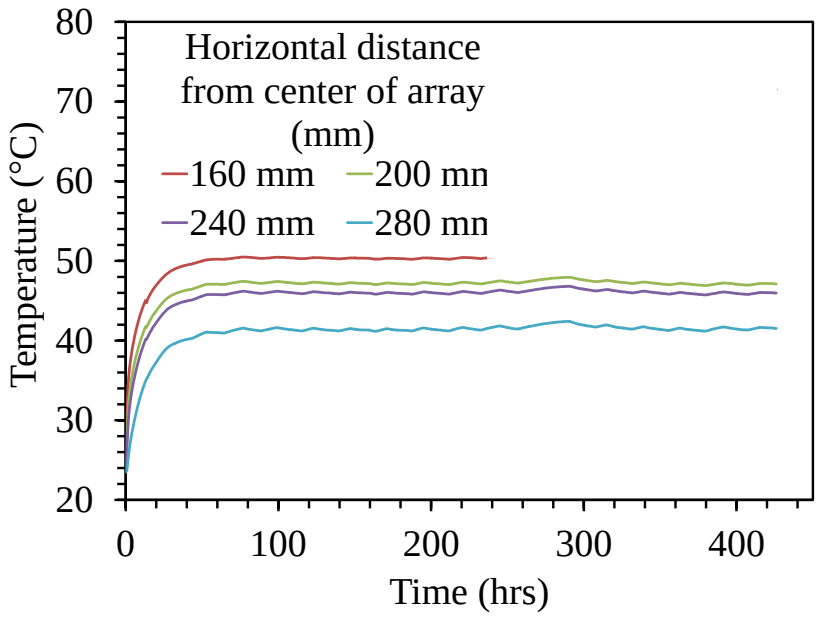

Figure 7.18 Average soil temperature with depth at four different horizontal distances from the center of the borehole heat exchanger array in Test 2

The changes in volumetric water content at different depths in the soil layer are shown in Figure 7.19. Different from the previous test, the volumetric water content and degree of saturation of the soil at different depths within the borehole array did not go below their original values, although the rate of decrease in volumetric water content indicates that it has not completely yet stabilized after 420 hours of testing. At all depths, a rapid increase in volumetric water content was observed within the first 100 hours of heating, followed by a slow, steady decrease over time. The upper section of the unsaturated zone appear to reach the maximum volumetric water content values earlier than the lower section. The soil at a depth of 355 mm in the unsaturated soil layer experienced the highest change in volumetric water content. In the mid-section of the vadose zone, volumetric water content stays relatively constant after the rapid increase. Condensation was observed under the hydraulic barrier at the soil surface. The initial increase indicate the movement of water due to the changes in temperature.

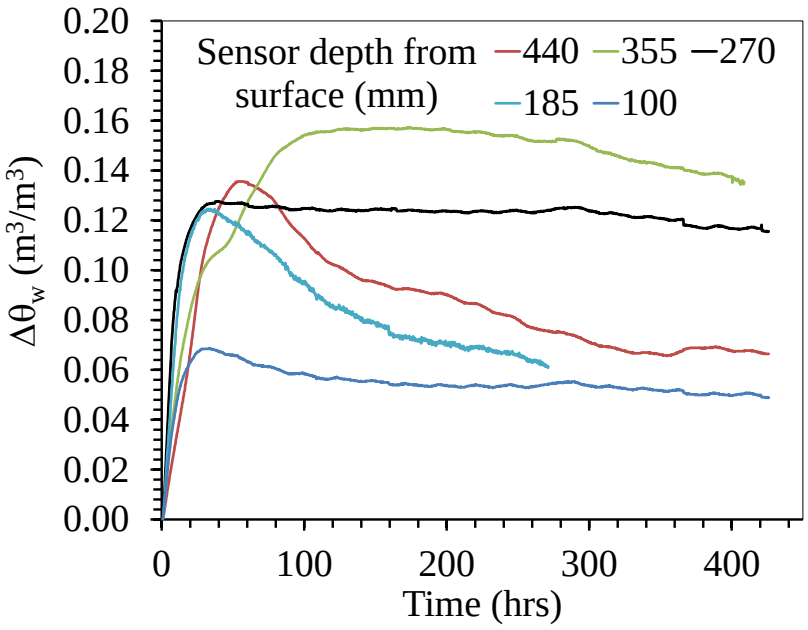

Figure 7.19 Time series of dielectric sensors data for Test 2: Change in volumetric water content

The degrees of saturation at different depths in the soil layer are shown in Figure 7.20. The follow similar trends to those shown in Figure 7.19, and a maximum increase in degree of saturation of about 0.3 was observed during heating.

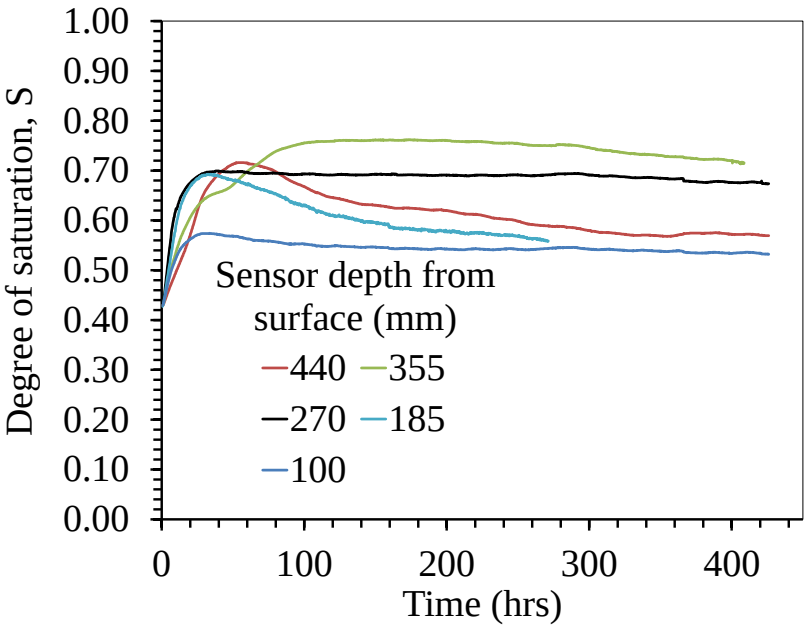

Figure 7.20 Time series of dielectric sensor data for Test 2: Degree of saturation

The apparent thermal conductivity and specific heat capacity of the unsaturated soil at the center of the profile are shown in Figure 7.21. Within the first 30 hours, the apparent thermal conductivity rapidly increases to a maximum value of 1.32 W/mK, which corresponds to the peak volumetric water content at depth 270 mm then slowly decreases to a value of 1.26 W/mK. The specific heat increases to approximately 2.21 MJ/m^{3}K following the same trend, but stays relatively constant for the rest of the test once it reaches the peak volumetric water content. Thermal conductivity is slightly enhanced with the borehole heat exchanger spacing in this test. Though it slowly decreases after it reaches its maximum value, it always stays higher that its initial value.

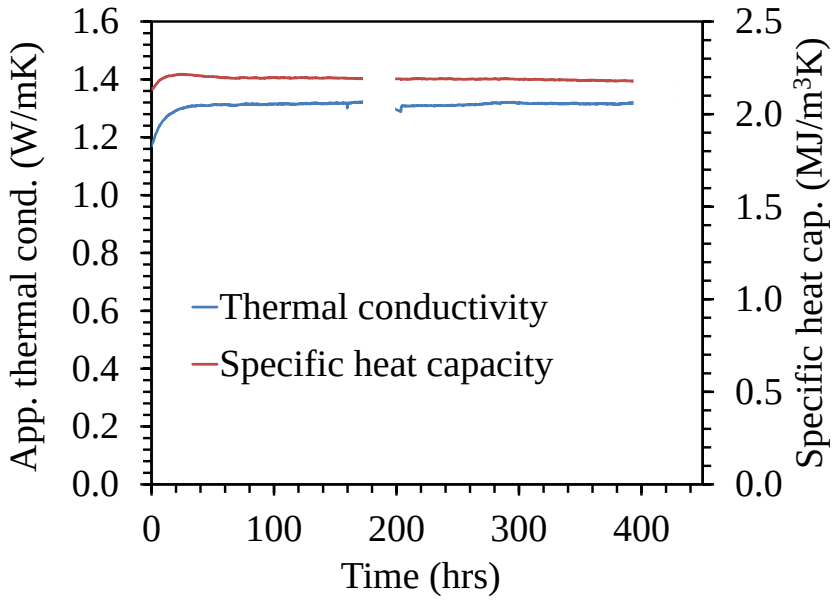

Figure 7.21 Time series data from SH-1 sensor embedded in the middle of the unsaturated soil layer in Test 2: Thermal conductivity and specific heat

7.3.2 Profiles of Temperature and Volumetric Water Content

The profiles of temperature and change in temperature are shown in Figures 7.22(a) and 7.22(b). Temperature is observed to reach a maximum value of approximately 50 °C of in 60 hours, after which it stays constant. Temperatures are highest at mid-height in the unsaturated soil layer.

The lowest temperatures are observed at the upper and lower regions of the unsaturated soil due to heat loss toward the surface and through the bottom of the tank.

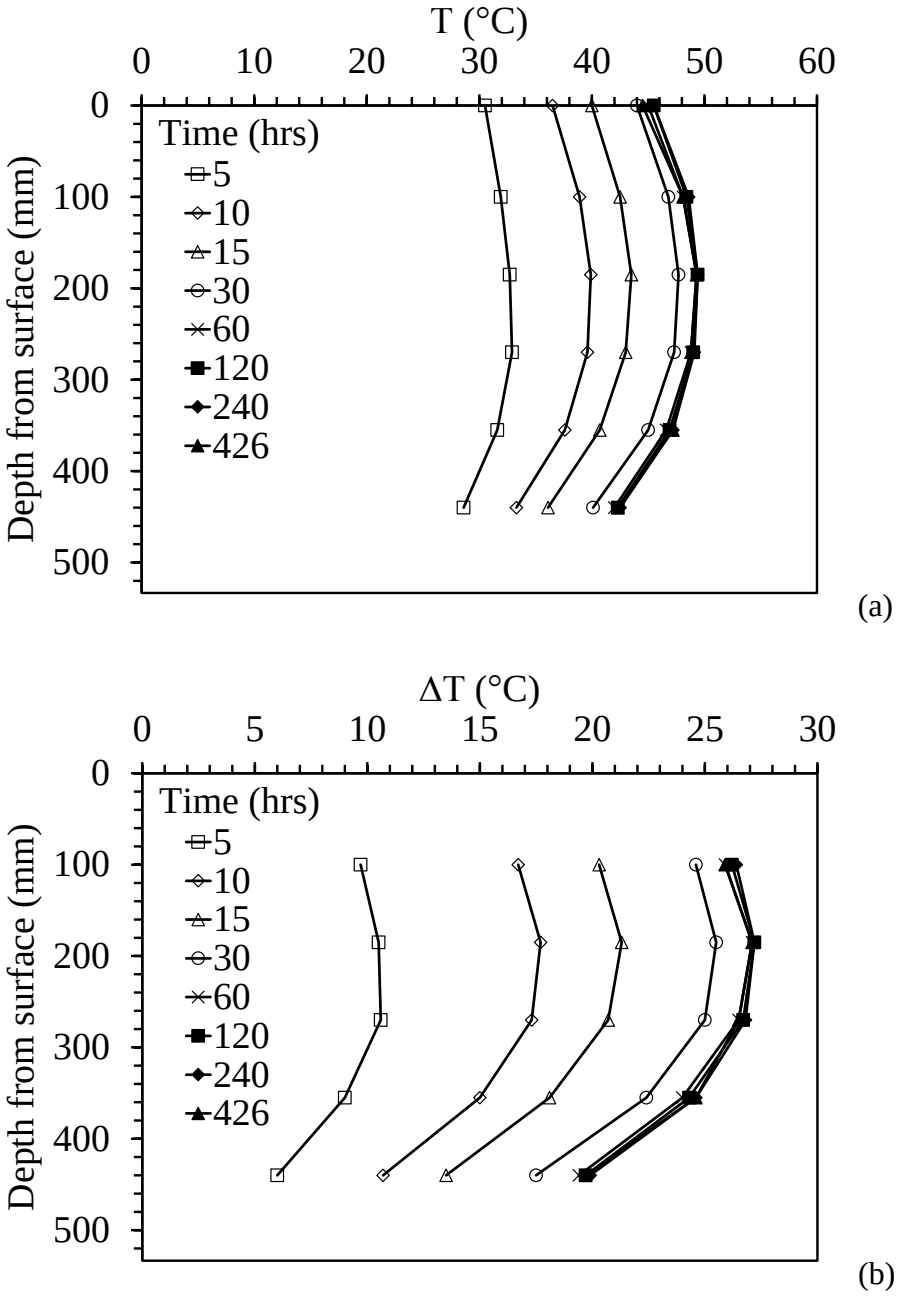

Figure 7.22 Dielectric sensor temperature profiles for Test 2: (a) Temperatures; (b) Change in temperatures

Profiles of the change in water content and degree of saturation are shown in Figures 7.23(a) and 7.23(b). The volumetric water content initially increases rapidly. After approximately 120

hours, the silt near the mid-height region of the unsaturated silt layer is the wettest in the unsaturated silt layer. It stays constant afterwards at that location while the lower region (355 mm) gets wetter while the volumetric water content of the upper and lower regions decrease. This may be due to both the upward movement of water from the lower regions and the flow of water to the middle of the array from the upper regions and the side regions. The unsaturated silt layer is then observed to slowly decrease in volumetric water content for the remainder of the experiment.

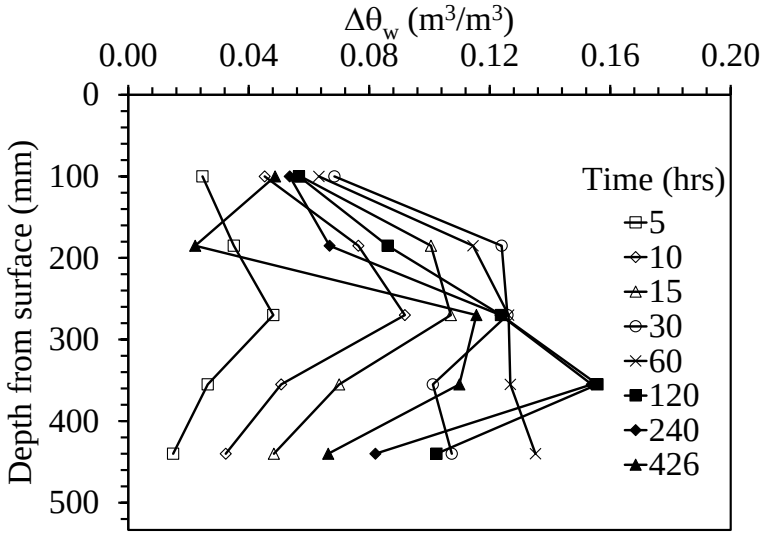

(a)

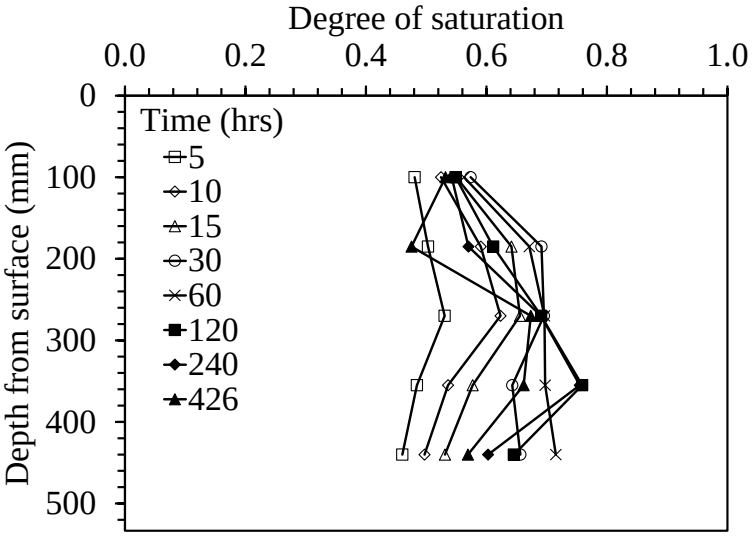

(b)

Figure 7.23 Dielectric sensor profiles for Test 2: (a) Change in volumetric water content; (b) Degree of saturation

Initial and final volumetric water contents for Test 2 are shown in Figure 7.24. The final volumetric water content profile indicates a lower water content than measured using the sensors, which contradicts the results from the dielectric sensors.

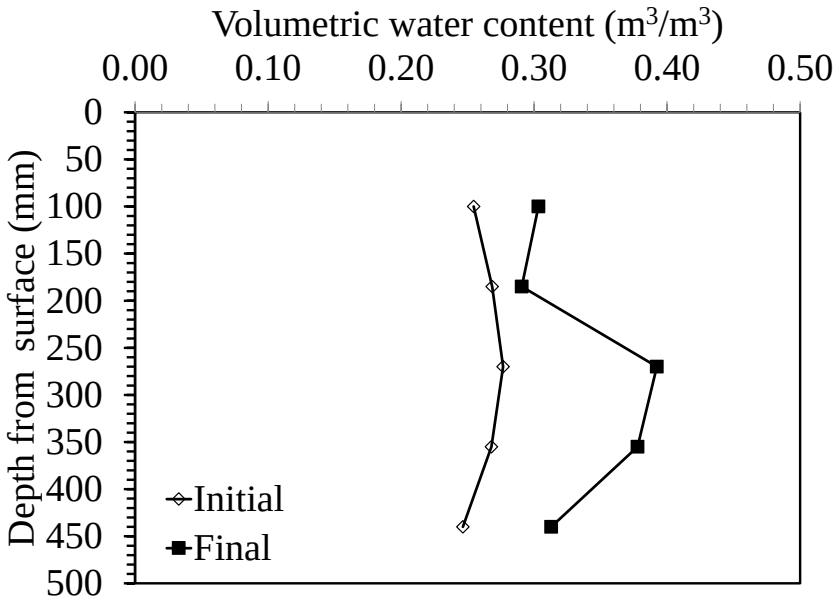

Figure 7.24 Dielectric sensor profiles for Test 2: Initial and final volumetric water contents

7.4 Test 3

This test was performed to assess the changes in volumetric water content and temperature within the unsaturated zone of soil within a borehole heat exchanger array having a radial spacing of 300 mm from the center of the container. The temperature of water entering the borehole heat exchangers was approximately 86 ºC, while the temperature of water exiting the heat exchangers was approximately 79 ºC, as shown in Figure 7.25. The experiment was stopped at 720 hours. Heated water was supplied to the heat exchangers at a flow rate of 18 mL/s. Using Equation (7.4), this flow rate along with the difference in inlet and outlet fluid temperatures corresponds to an average of 180 W of energy input to the unsaturated soil layer. The volume of water supplied to the sand layer to maintain a water pressure at the top of the system was approximately equal to 8.5 L, which was absorbed at a relatively steady pace over the course of the 720 hours of testing.

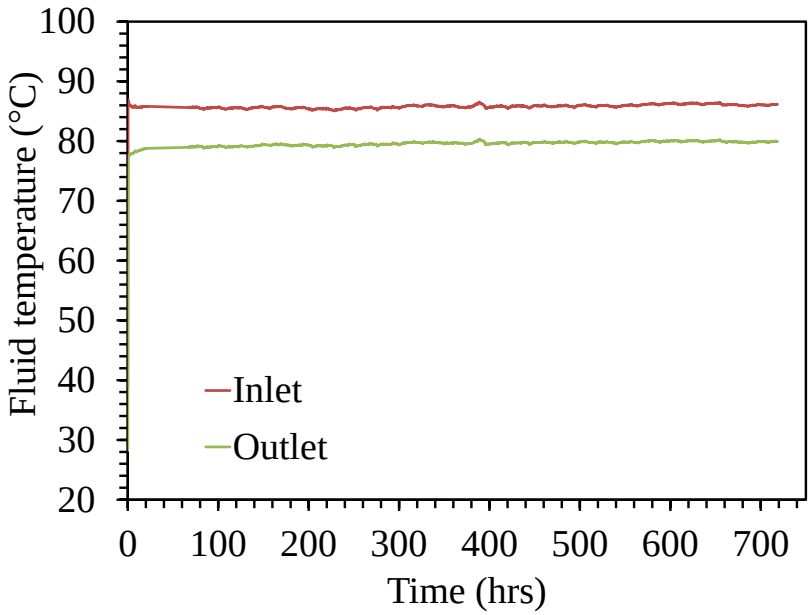

Figure 7.25 Temperatures at the soil surface (under the hydraulic barrier) and in the laboratory for Test 3

7.4.1 Time Series of Temperature, Water Content, and Soil Properties

Temperatures and humidity at the surface of the soil and that of the experimental environment are compared in Figures 7.26 and 7.27. The room temperature and relative humidity oscillate in a relatively consistent pattern. At the surface of the soil, the temperature and relative humidity reach values of 38 ºC and 71%, respectively within 100 hours. Insulation was placed over the hydraulic barrier so only slight oscillations in the room temperature were observed to affect the soil surface temperatures. The temperatures of the silt at the depths of the five 5TE sensors are shown in Figures 7.28 (a) and 7.28(b). Temperatures are relatively steady after approximately 60 hours of testing. The lowest temperatures are observed in the upper and lower regions of the unsaturated silt layer. The highest temperatures are observed at mid-height and in the upper regions of the unsaturated silt layer (i.e. 100 mm to 270 mm) while the lowest temperatures were observed in the lower region (i.e. 440 mm). The temperatures from the profile

probes are shown in Figure 7.29. As expected, temperature decreases as the distance away from the borehole heat exchanger array increases.

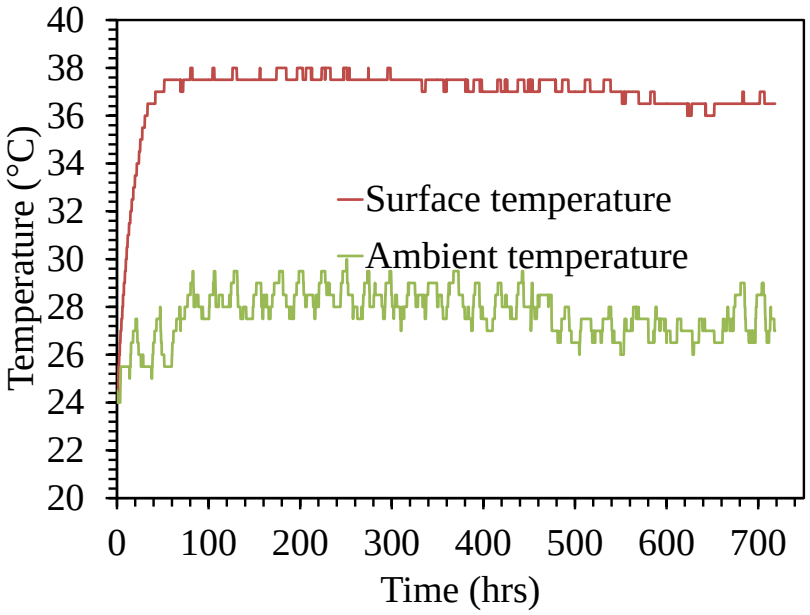

Figure 7.26 Temperatures at the soil surface (under hydraulic barrier) and in the laboratory for Test 3

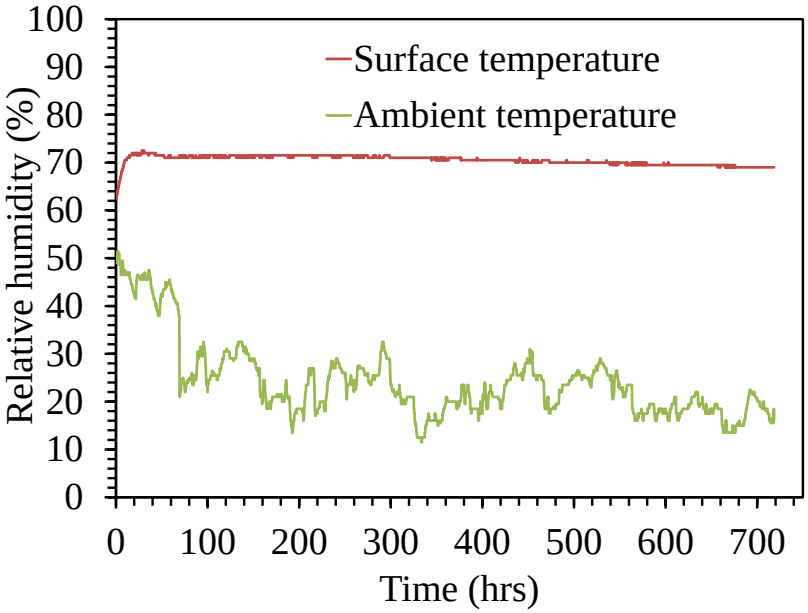

Figure 7.27 Relative humidities at the soil surface (under hydraulic barrier) and in the laboratory for Test 3

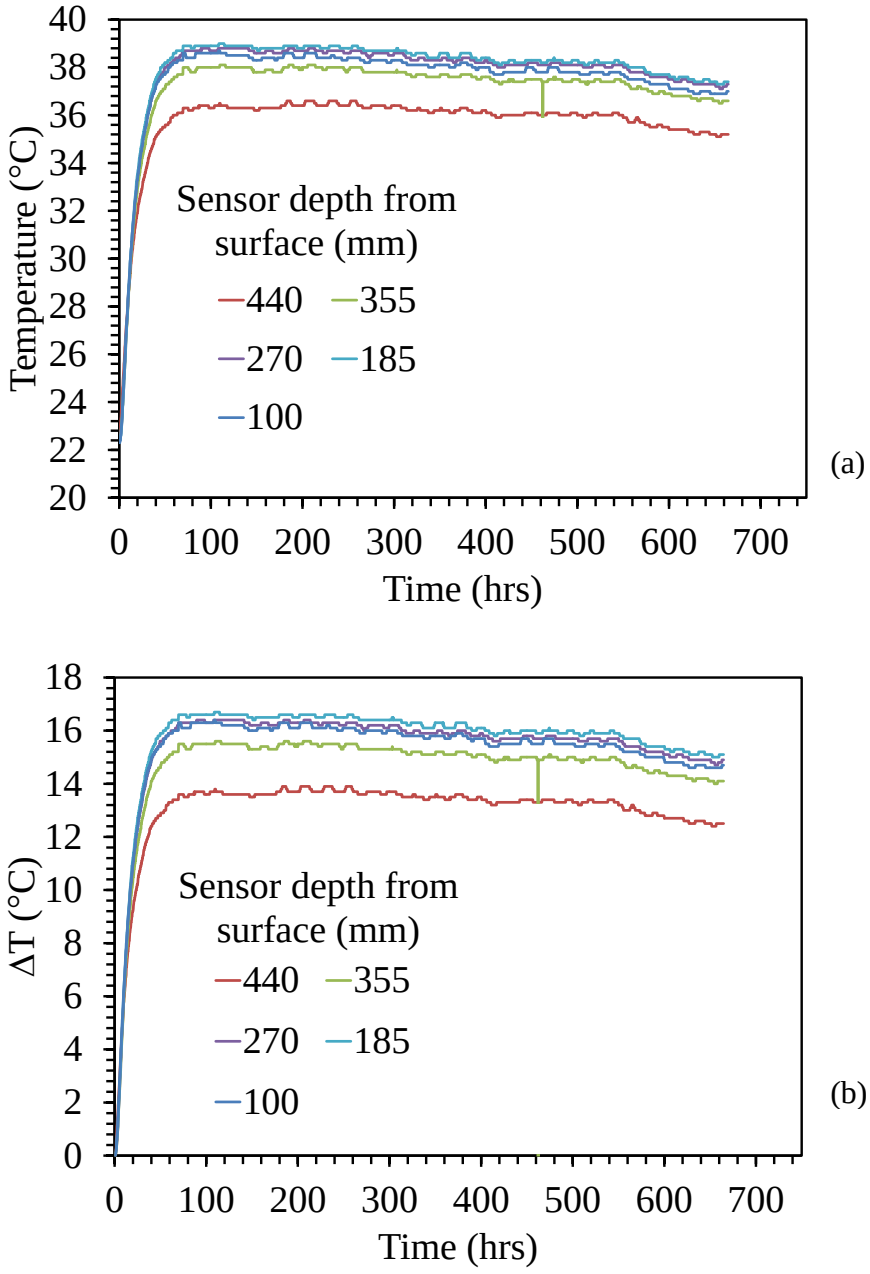

Figure 7.28 Time series of dielectric sensor data in Test 3: (a) Temperature; (b) Change in temperature

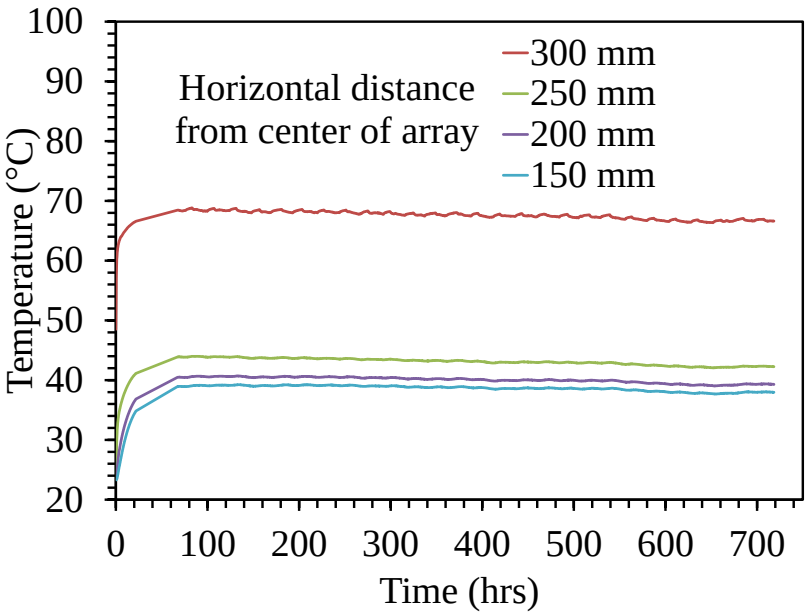

Figure 7.29 Average soil temperature with depth at four different horizontal distances from the outside of the borehole heat exchanger array in Test 3

The time series of the change in volumetric water content is shown in Figure 7.30. The degree of saturation at all depths, calculated from the water content over time is shown in Figure 7.31. At all depths, a rapid increase in volumetric water content and degree of saturation was observed in the first 40 hours of heating, followed by a slow steady decrease over time. The highest volumetric water content and degree of saturation is observed in the middle and lower regions of the unsaturated silt, while the lowest water content is observed in the upper and lower regions. Condensation was observed near the surface of the unsaturated silt. It was also observed that the upward flow of water occurred at a much slower rate than in Tests 1 and 2. The thermal conductivity of the unsaturated soil at the center of the profile is shown in Figure 7.32. The thermal conductivity increases rapidly for approximately 40 hours, which corresponds to the maximum reached degree of saturation. After that point, the apparent thermal conductivity stays constant at 1.22 W/mK. Specific heat capacity increases within the first 220 hours until it becomes constant at 2.05 MJ/m^{3}K. This trend is similar to that observed in Test 2. A picture of the container after

the test is shown in Figure 7.33. A distinct zone of drying is not observed in this figure different than in Test 1, and the color of the soil was relatively consistent throughout the soil layer.

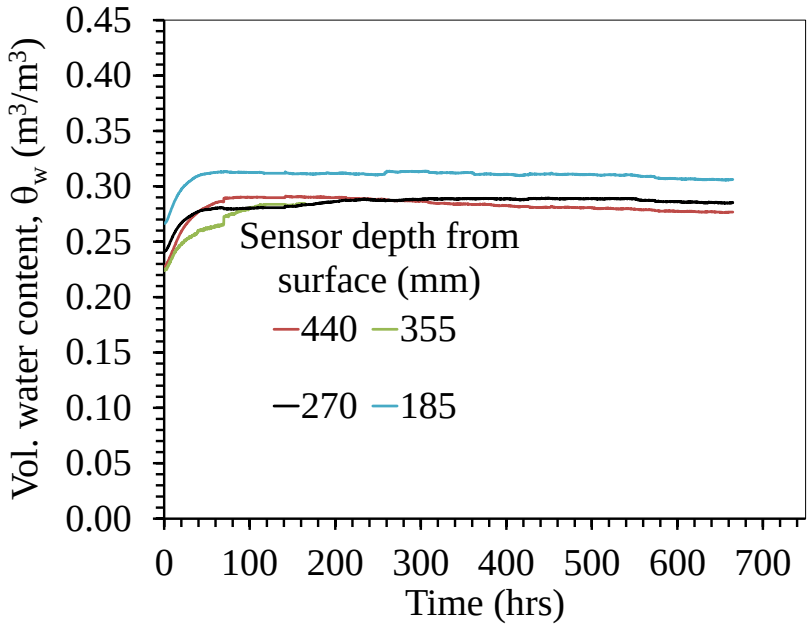

Figure 7.30 Time series of dielectric sensor in Test 3: Change in volumetric water contentat different depths

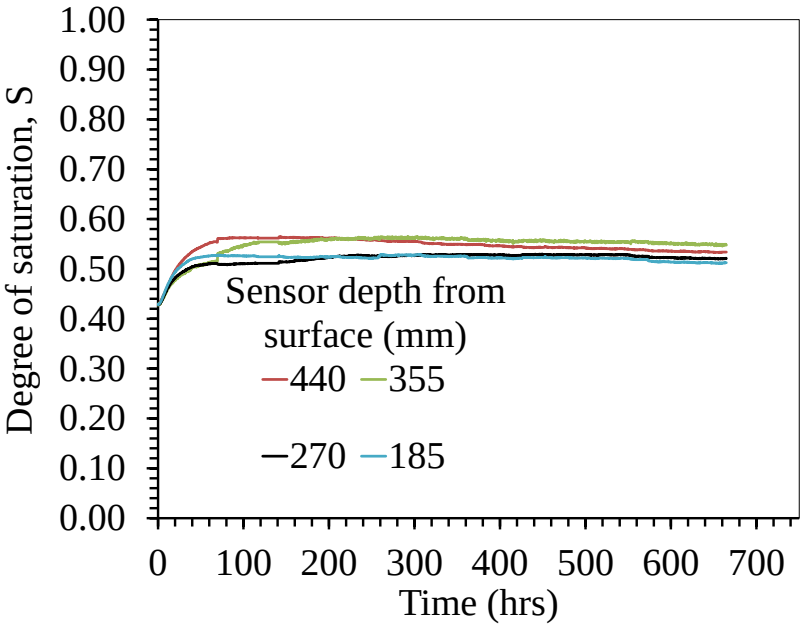

Figure 7.31 Time series of dielectric sensor data in Test 3: Degree of saturation at different depths

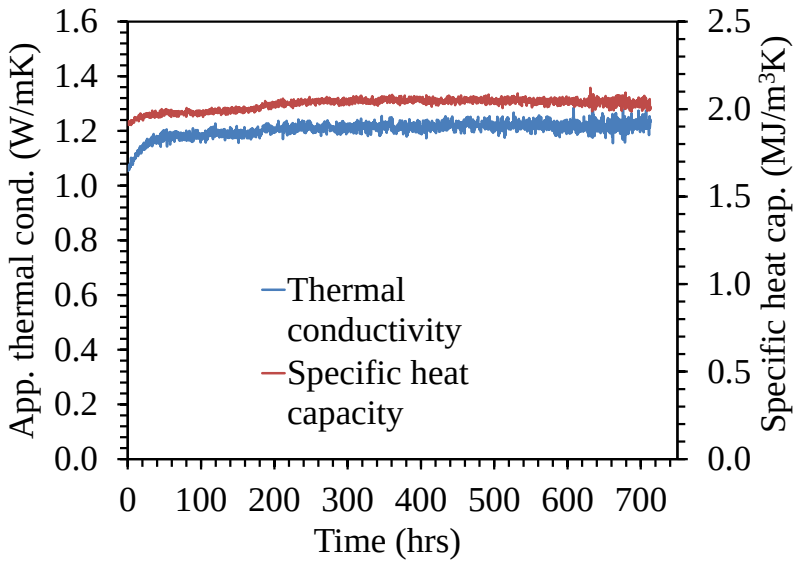

Figure 7.32 Time series from SH-1 sensor embedded in the middle of the unsaturated soil layer in Test 3: Thermal conductivity and specific heat capacity

Figure 7.33 Post-test profile section of the unsaturated silt layer in Test 3

7.4.2 Profiles of Temperature and Volumetric Water Content

The profiles of temperature and change in temperature with depth are shown in Figures 7.34(a) and 7.34(b). The temperature is observed to reach a maximum value of approximately 40 ºC in 120 hours of operation, after which it remains relatively constant. Temperatures are highest around the middle regions of the unsaturated silt layer.

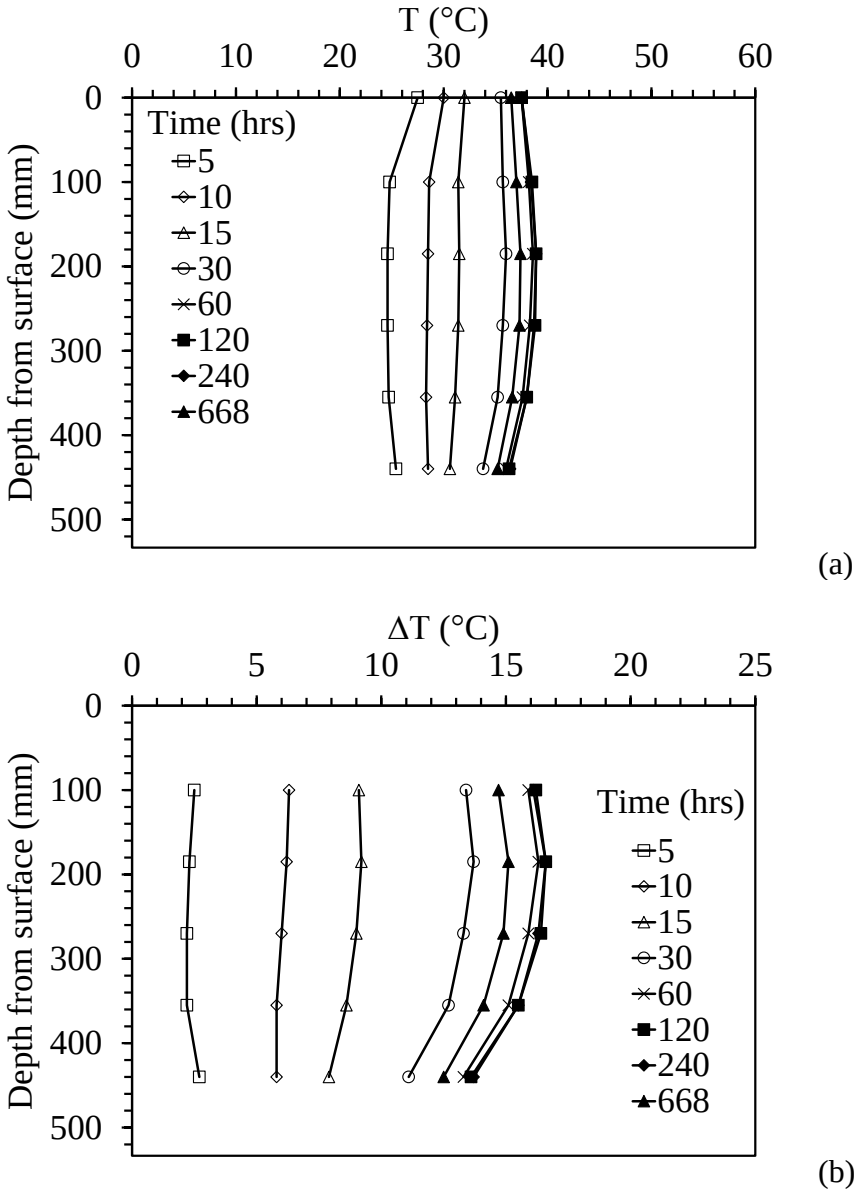

Figure 7.34 Dielectric sensor profiles in Test 3: (a) Temperatures; (b) Changes in temperature

The profiles of the change in volumetric water content and degree of saturation are shown in Figures 7.35(a) and 7.35(b). The lower maximum temperature may be attributed to the fact that energy is being transferred in a larger mass of soil (radius of 300 mm). Furthermore, the borehole heat exchangers were in contact with the boundary of the container, causing heat losses through the steel container. The volumetric water content initially increases rapidly at all depths. After 120 hours, it stays relatively constant for the middle and upper regions, while it decreases in the bottom region. The silt near the water table at the base of the unsaturated silt is wetter than the silt near the surface. This result is opposite from that observed in Test 1 but consistent with observations made in Test 2. Figure 7.36 shows the initial and final volumetric water contents in Test 3. Like in Test 2, these water content profiles contradict the readings from the sensors.

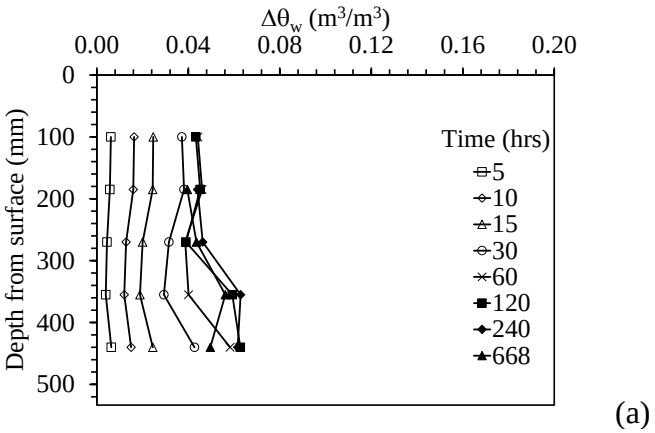

(a)

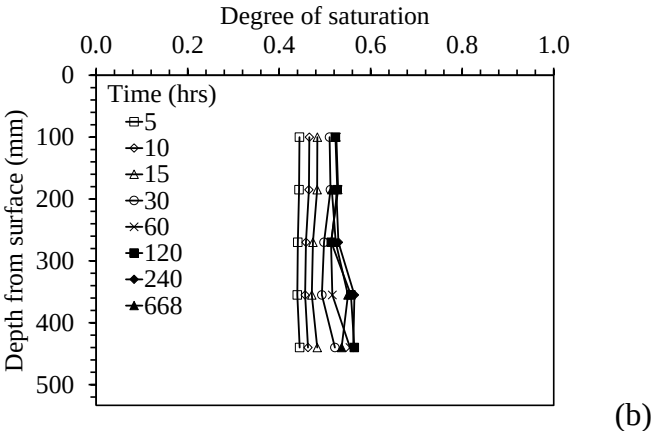

(b)

Figure 7.35 Dielectric sensor profiles in Test 3: (a) Volumetric water content; (b) Degree of saturation

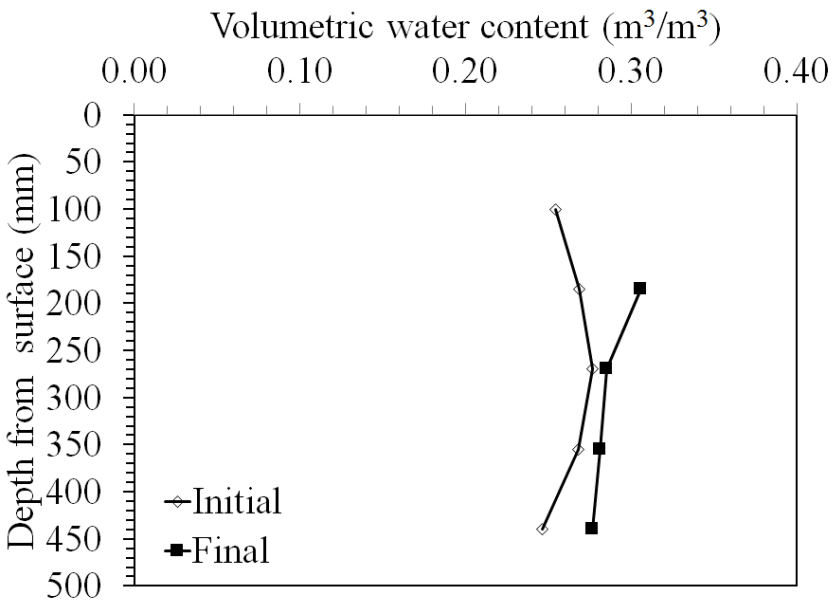

Figure 7.36 Dielectric sensor profiles: Initial and final volumetric water contents in Test 3

7.5 Test 4

This test was performed to assess the changes in volumetric water content and temperature within the unsaturated zone of soil within a borehole heat exchanger array having a radial spacing of 150 mm from the center of the container. The temperature of water entering the borehole heat exchangers was approximately 84 ºC, while the temperature of water exiting the heat exchangers was approximately 78 ºC, as shown in Figure 7.37. The experiment was stopped at 370 hours even though there were still minor changes in material properties. The SH-1 thermal conductivity sensor was not placed in the soil body because it was defective at the time. Heated water was supplied to the heat exchangers at a flow rate of 7 mL/s. The flow rate of water circulating through the borehole heat exchangers was measured to be 7 mL/s. Using Equation (7.4), this is equivalent to an average of 180 W of energy input into the unsaturated soil layer. The volume of water supplied to the sand layer to maintain a water pressure at the top of the system was equal to 4.5 L, which was absorbed at a relatively steady pace over the course of the 370 hours of testing.

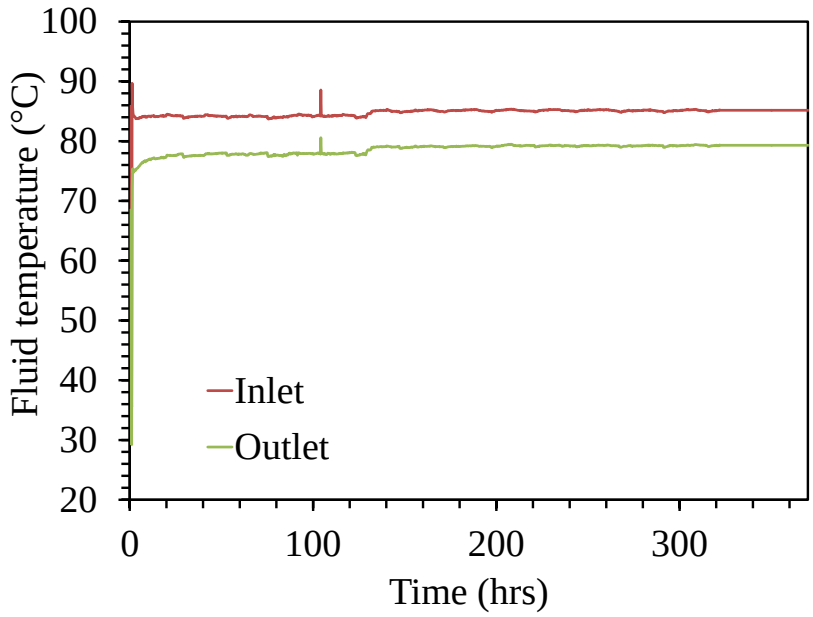

Figure 7.37 Inlet and outlet heat exchange fluid temperatures in Test 4

7.5.1 Time Series of Temperature, Water Content, and Soil Properties

Temperatures and humidity at the surface of the soil and that of the experimental environment are compared in Figures 7.38 and 7.39. Room temperature and humidity oscillates in a relatively constant pattern while at the surface of the soil the temperature and humidity reach values of 38 ºC and 60%, respectively within 30 hours. Different from Test 1, surface insulation was not used, although a saran wrap hydraulic barrier was still used. Oscillations in the room temperature were observed to affect the soil surface temperatures.

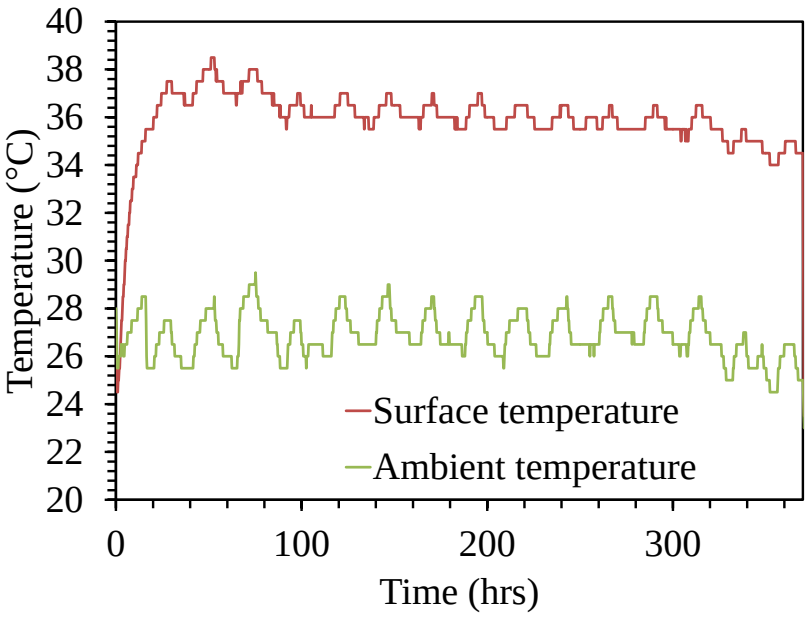

Figure 7.38 Temperatures at the soil surface (under hydraulic barrier) and in the laboratory for Test 4

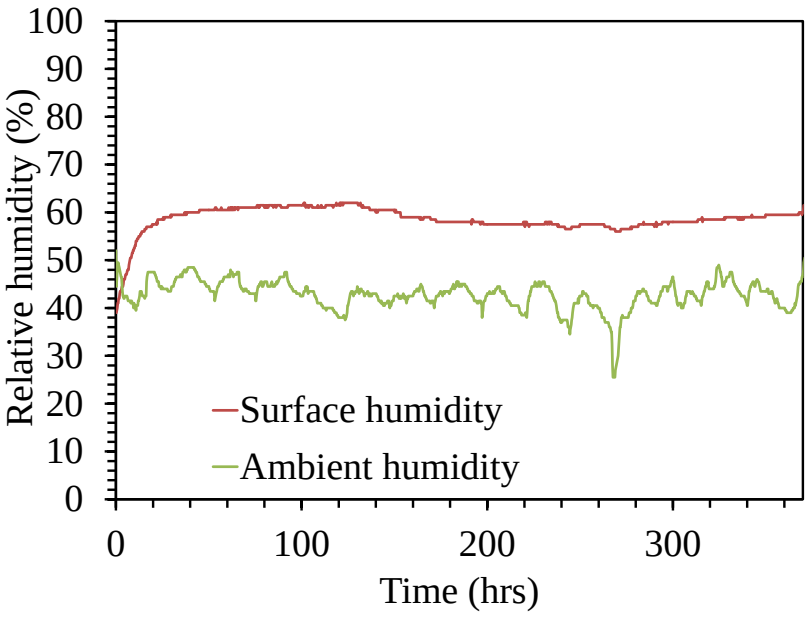

Figure 7.39 Relative humidities at the soil surface (under hydraulic barrier) and in the laboratory for Test 4

In this test, one of the 5TE dielectric sensors was damaged during compaction and was not functional. Time series of the temperature and change in temperature measured using the four functional dielectric sensors are shown in Figures 7.40(a) and 7.40(b). The soil was observed to

increase in temperature after approximately 60 hours, after which it stabilizes at all depths. The mid-area of the unsaturated soil layer (e.g., at depths of 270 and 355 mm) shows the highest temperatures while the bottom and the top show the lowest.

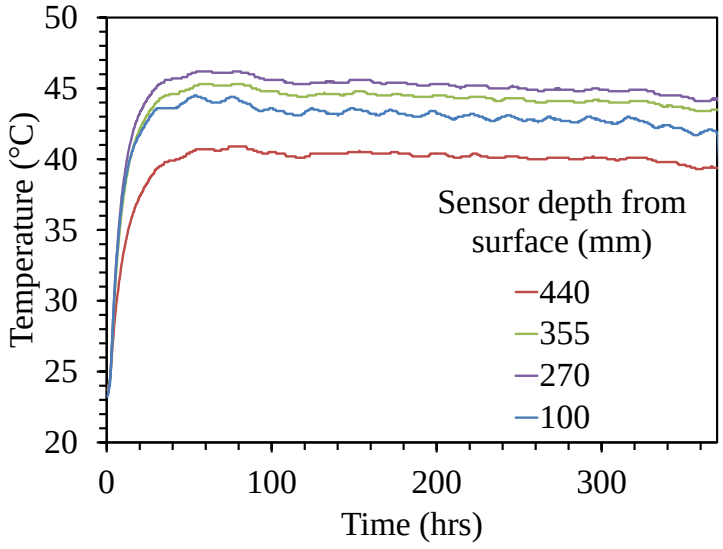

(a)

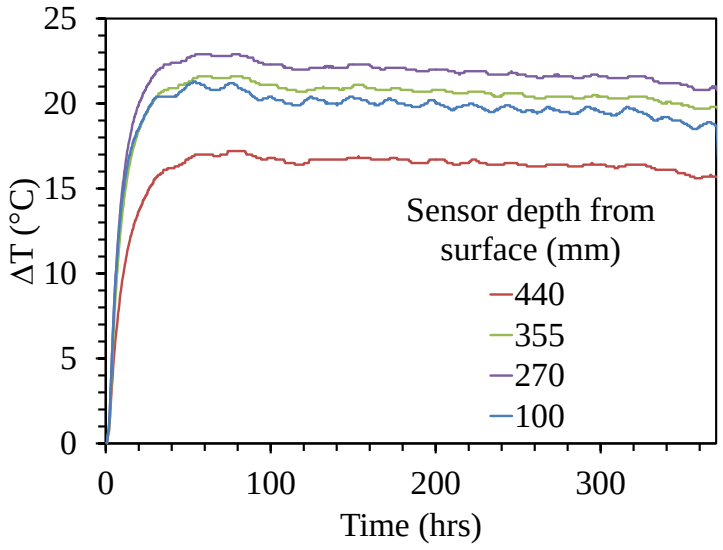

(b)

Figure 7.40 Temperature data from the dielectric sensors embedded at the center of the soil layer (a) Temperature; (b) Change in temperature over time in Test 4

The average temperatures from the 6 sensors in each of the thermocouple profile probes are shown in Figure 7.41. As expected the thermocouple probes indicate that temperatures are lower as the horizontal distance from the closest heat exchanger increases.

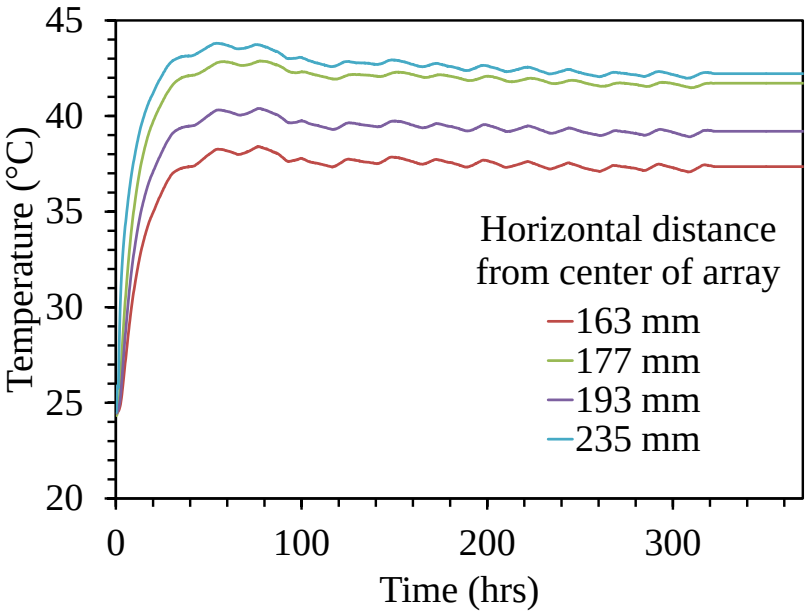

Figure 7.41 Average soil temperature with depth at four different horizontal distances from the center of the borehole heat exchanger array in Test 4

The changes in volumetric water content at different depths in the soil layer are shown in Figure 7.42. A rapid increase in volumetric water content was observed in the first 40 hours of heating, followed by a slow, steady decrease over time. The soil above a depth of 440 mm in the unsaturated soil layer experienced the highest change in volumetric water content. The degrees of saturation at different depths in the soil layer are shown in Figure 7.43. Different from the previous test, volumetric water content within the borehole array did not go below its original value, but the rate of decrease in volumetric water content indicates that it has not yet stabilized after 370 hours of testing.

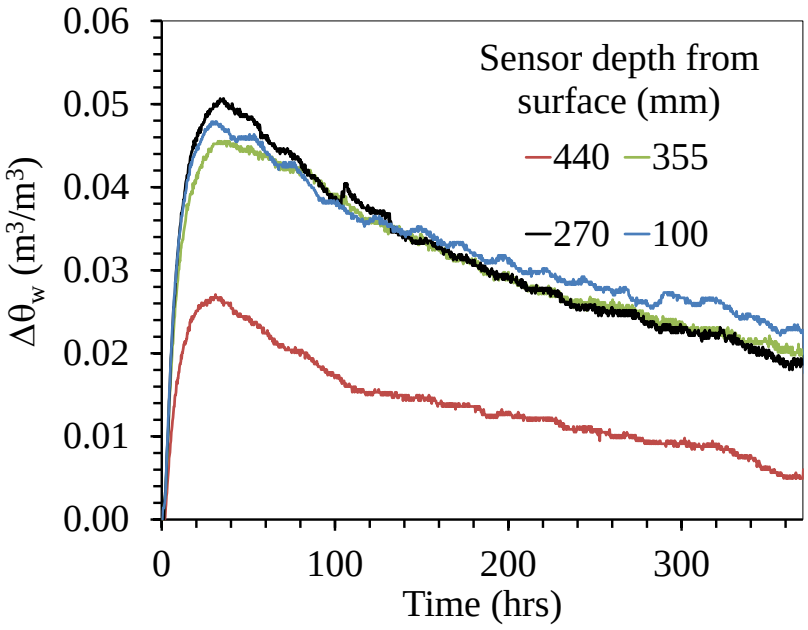

Figure 7.42 Time series of dielectric sensor data for Test 4: Change in volumetric water content

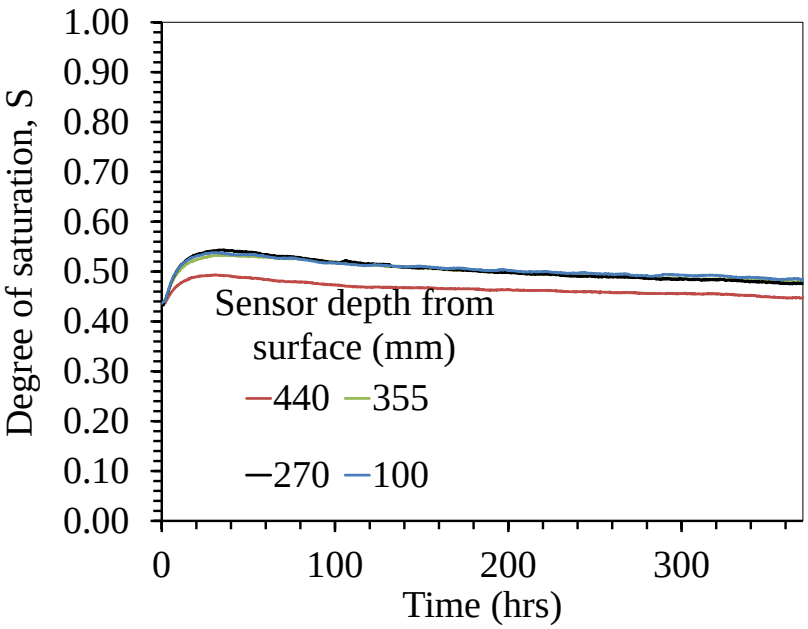

Figure 7.43 Time series of dielectric sensor data for Test 4: Degree of saturation

7.5.2 Profiles of Temperature and Volumetric Water Content

The profiles of temperature and change in temperature are shown in Figures 7.44(a) and 7.44(b). Temperature is observed to reach a maximum value of approximately 46 °C of in 60 hours, after which it stays constant. Temperatures are highest at mid-height in the unsaturated soil layer. The lowest temperatures are observed at the upper and lower regions of the unsaturated soil.

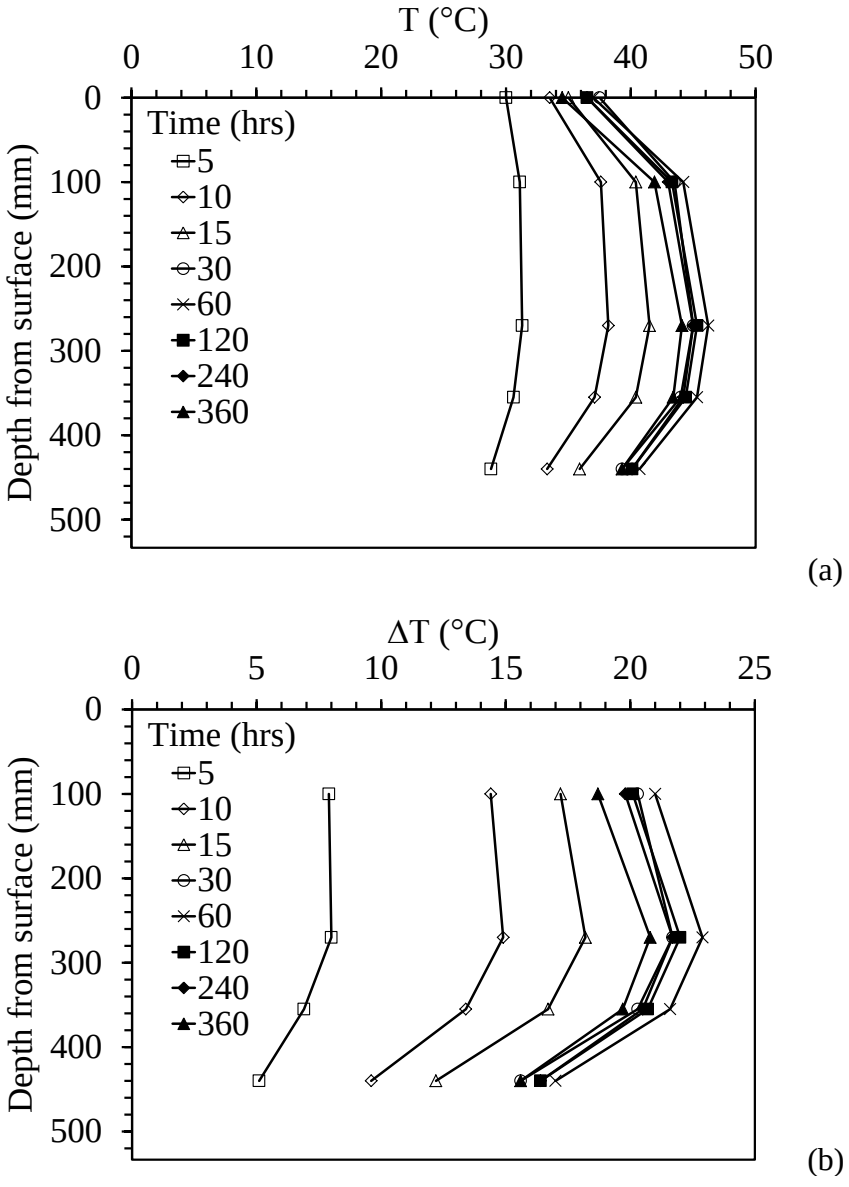

Figure 7.44 Dielectric sensors temperature profiles for Test 4: (a) Temperatures; (b) Change in temperatures

Profiles of the change in water content and degree of saturation are shown in Figures 7.45(a) and 7.45(b). The volumetric water content initially increases rapidly. After approximately 120 hours, the silt near the surface of the unsaturated silt layer is wetter than the silt at the bottom of the unsaturated silt layer. As explained earlier, this reflects the upward movement of water vapor during heating. The unsaturated silt layer is then observed to rapidly decrease in water content for the remainder of the experiment, after which it is nearly uniform and similar to initial conditions.

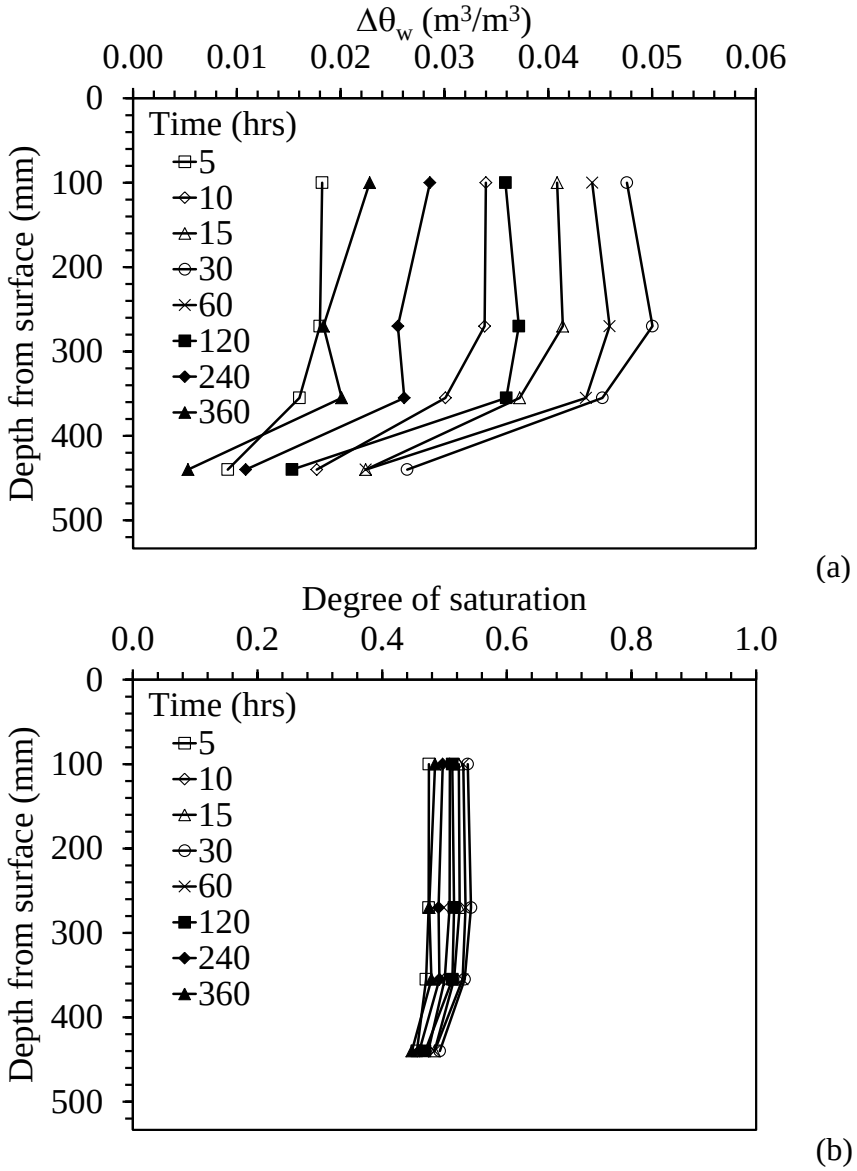

Figure 7.45 Dielectric sensor profiles for Test 4: (a) Change in volumetric water content; (b) Degree of saturation

Initial and final volumetric water contents for this test are shown in Figure 7.46. Consistent with the dielectric sensor measurements, even though the soil experienced a relatively uniform increase then decrease in water content, its final value is still higher than its initial.

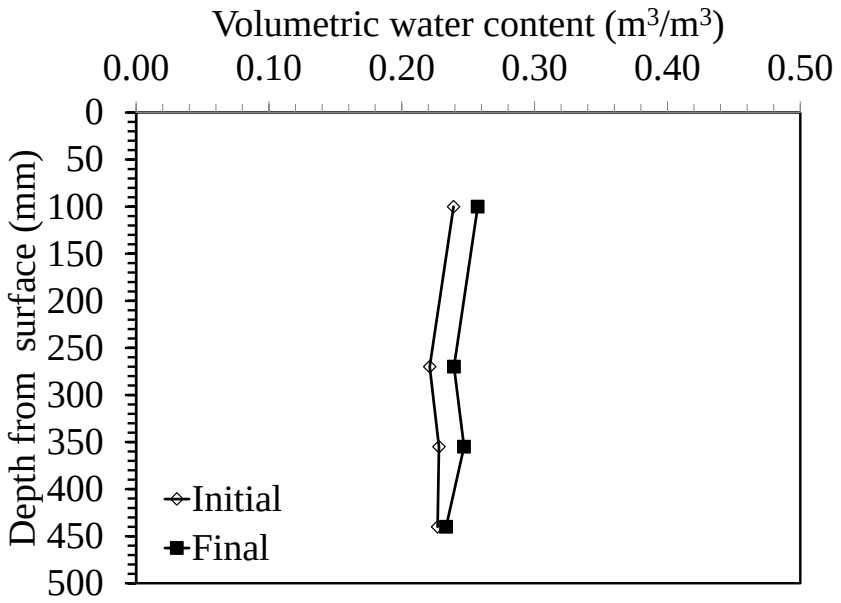

Figure 7.46 Dielectric sensor profiles for Test 4: Initial and final volumetric water content

7.6 Test 5

The set of sensors comprised the five 5TE sensors and the SH-1 sensor. Saran wrap was used at the surface of the unsaturated silt layer as hydraulic barrier, but no hydraulic barrier was incorporated. Due to intermittent pump performance, the test was performed for only 130 hours. The borehole heat exchangers had a radial spacing of 100 mm from the center of the container. The silt used in this test was compacted to a dry density of 1715 kg m^{-3}. No vacuum was applied when saturating the sand layer. The temperature of the water entering the borehole heat exchangers was regulated to 65 ºC.

7.6.1 Time Series of Temperature, Water Content, and Soil Properties

The temperatures of the silt at the depths of the five 5TE sensors are shown in Figures 7.47(a) and 7.47(b). Temperatures are relatively steady after approximately 50 hours of testing. The

lowest temperatures are observed in the upper and lower regions of the unsaturated silt layer. The highest temperatures are observed at mid-height in the silt layer (i.e. 355 mm and 270 mm).

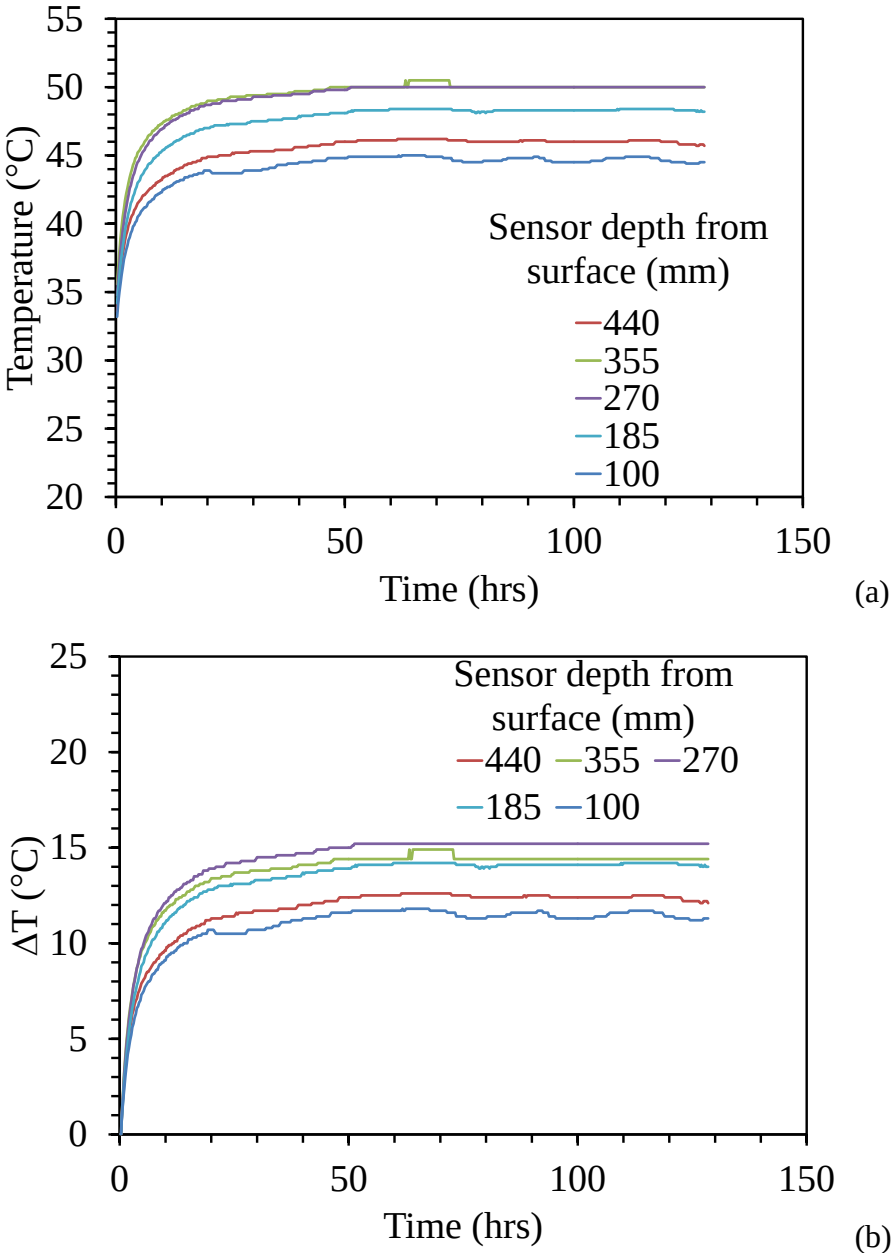

Figure 7.47 Time series of ielectric sensor data in Test 5: (a) Temperature; (b) Change in temperature

The time series of volumetric water content and change in volumetric water content are shown in Figures 7.48(a) and 7.48(b), while the calculated degree of saturation is shown in Figure 7.49. At all depths, rapid increases in volumetric water content and degree of saturation were

observed in the first 20 hours of heating, followed by a slow steady decrease over time. The highest volumetric water content and degree of saturation is observed in the middle and lower regions of the unsaturated silt, while the lowest water content is observed in the upper regions. This is the opposite of what was observed in the two previous tests. Condensation was observed near the surface of the unsaturated silt. This observation indicates that water flowed upwards at a much slower rate than in Test 1 and Test 2. The higher density of the silt causes porosity to be much lower, which in turn inhibits the vapor flow upwards.

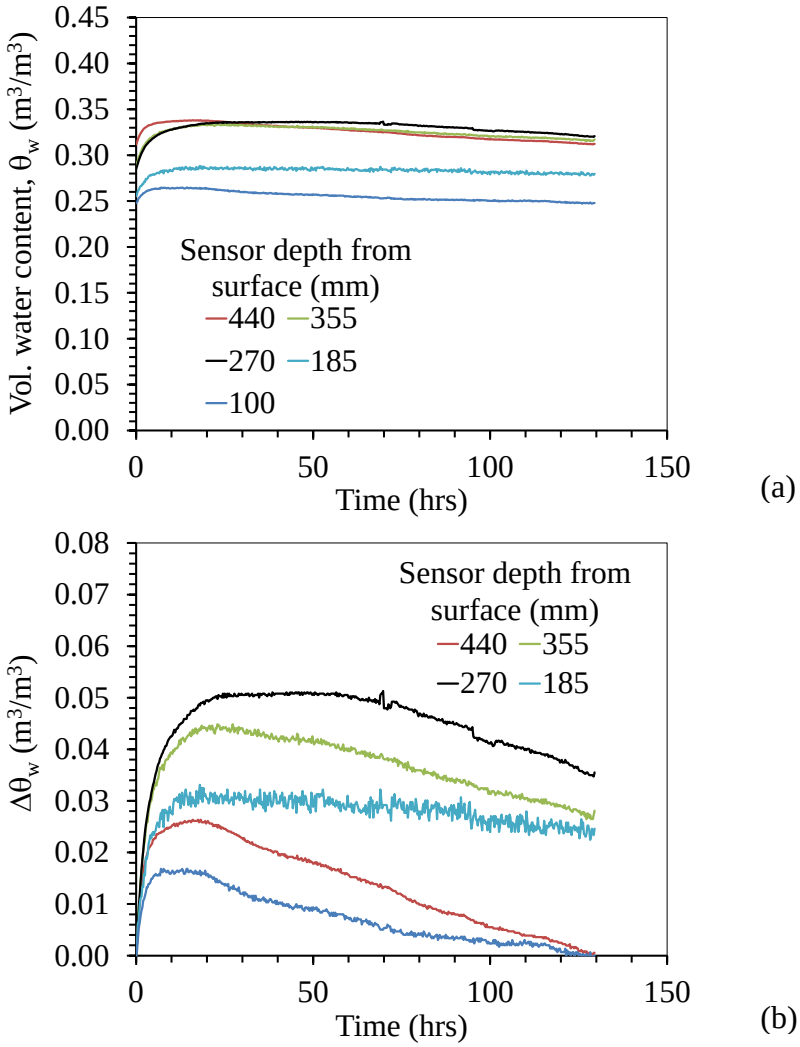

Figure 7.48 Time series of dielectric sensors data in Test 5: (a) Volumetric water content; (b) Change in volumetric water content

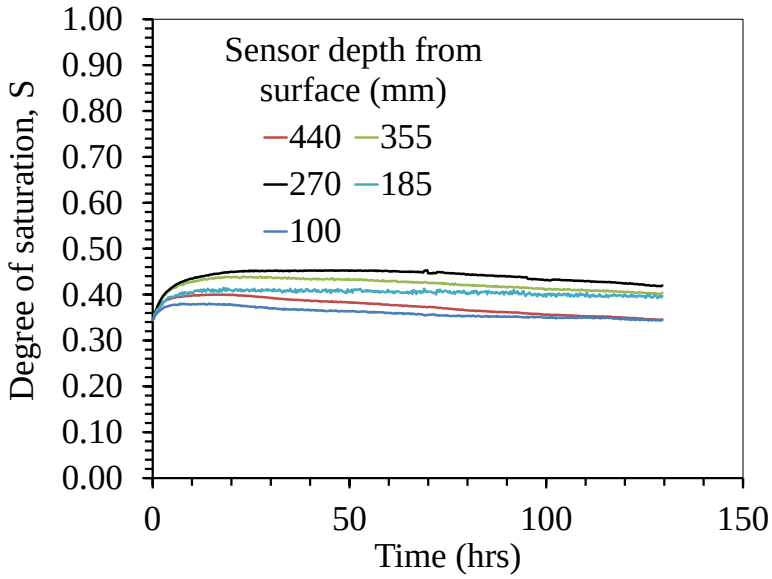

Figure 7.49 Time series of dielectric sensor data in Test 5: Degree of saturation at different depths

The thermal conductivity of the unsaturated soil at the center of the profile is shown in Figure 7.50. The thermal conductivity increases rapidly for approximately 20 hours, after which it increases at a slower rate. Specific heat capacity appears to rapidly increase to a value of approximately 2.56 in 20 hours, then decreases almost at the same rate. This is very similar to the trend observed in Test 1. After 50 hours of testing, the thermal conductivity sensor was accidentally disconnected.

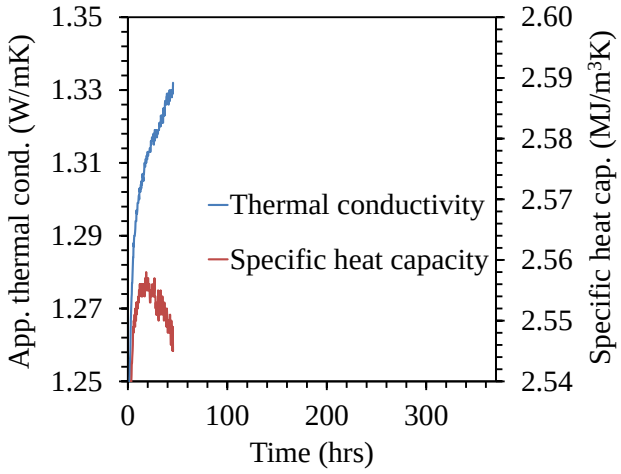

Figure 7.50 Time series from SH-1 sensor embedded in the middle of the unsaturated soil layer in Test 5: Thermal conductivity and specific heat capacity

7.6.2 Profiles of Temperature and Volumetric Water Content

The profiles of temperature and change in temperature are shown in Figures 7.51(a) and 7.51(b). The temperature is observed to reach a maximum value of approximately 50 ºC in 60 hours of operation, after which it remains constant. Temperatures are highest in the middle regions of the unsaturated silt layer.

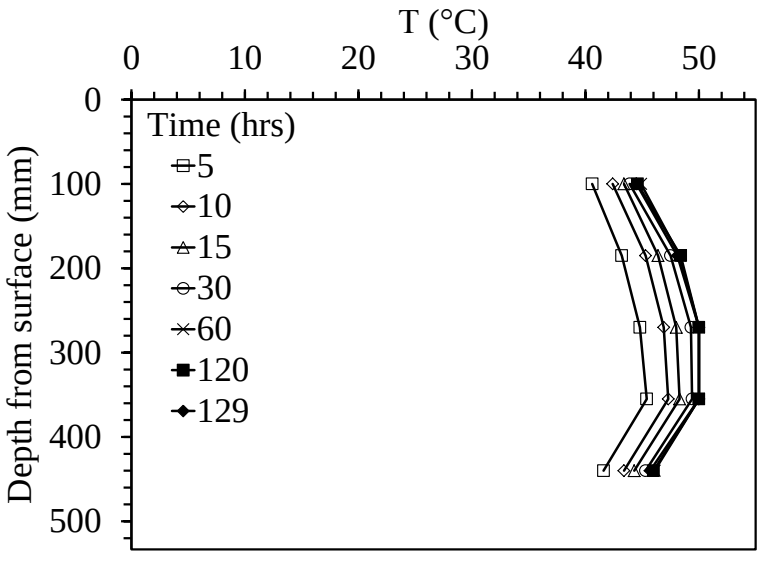

(a)

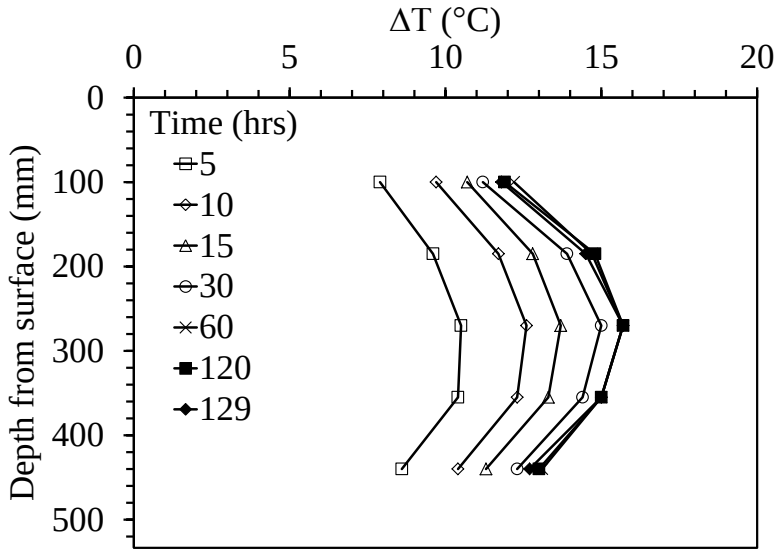

(b)

Figure 7.51 Dielectric sensor profiles in Test 5: (a) Temperatures; (b) Change in temperatures

The profiles of the change in volumetric water content and degree of saturation are shown in Figures 7.52(a) and 7.52(b). The results are similar to that of Test 1 where the radial spacing of the closed-loop heat exchanger pipes was 80 mm. The volumetric water content increases rapidly at all depths, but the test was not long enough to dry the silt layer like in Test 1.

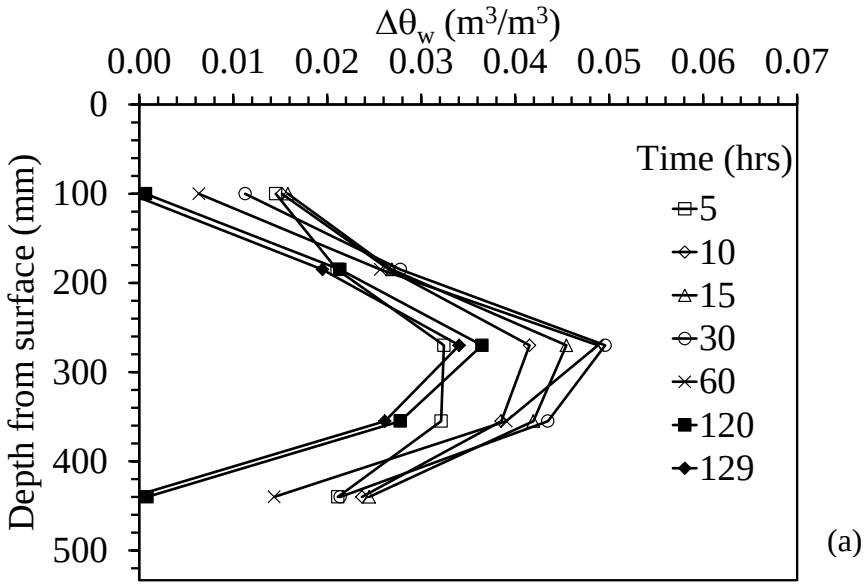

(a)

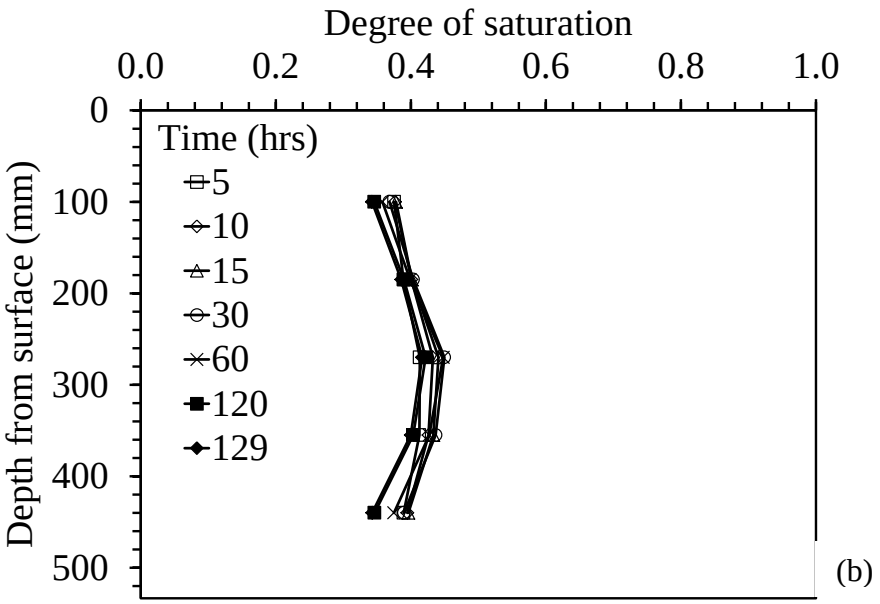

Figure 7.52 Dielectric sensor profiles in Test 5: (a) Volumetric water content; (b) Degree of saturation

The silt near the surface is wetter than the silt near the water table at the base of the silt layer. This reflects the slow upward water vapor movement during the heating process. At 129 hours, the volumetric water content at the top and bottom of the unsaturated silt layer has already

decreased back to its initial value. These values might have been lower than initial values for a longer testing time. Figure 7.53 shows the initial and final volumetric water contents in Test 5.

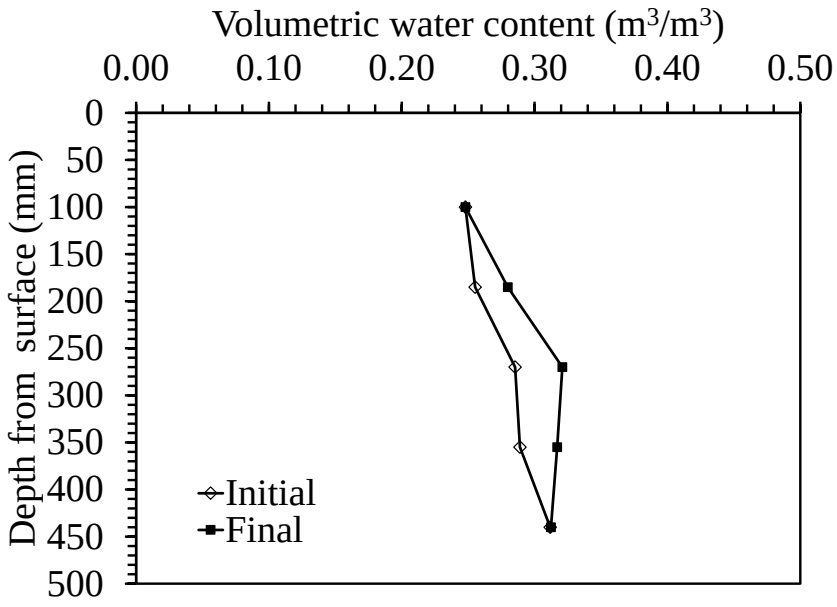

Figure 7.53 Dielectric sensor profiles: Initial and final volumetric water content in Test 5

8. ANALYSIS

8.1 Coupling between Soil Properties

In order to analyze the heat and water transfer in the vadose zone within the closed-loop heat exchangers array, the coupling between the different thermo-hydraulic properties of the unsaturated soil must be understood. Relationships between the apparent thermal conductivity, specific heat capacity, temperature, volumetric water content, and degree of saturation are explored in this section. This will focus on Tests 1, 2 and 3 as they have the most complete sets of data. The changes in apparent thermal conductivity and degree of saturation of the change in temperature during Test 1, 2 and 3 are shown in Figures 8.1, 8.2 and 8.3, respectively. It appears that thermal conductivity is enhanced by the presence of water as expected. For Test 1 (80 mm array spacing) at a change in temperature of 31 ºC, the degree of saturation decreases, leading to a sudden decrease in thermal conductivity. The energy transfer within the heat exchanger array causes water to flow out of the soil within the heat exchangers array in the form of water vapor. As a result, the soil pores are filled with air, which is a poor heat conductor. Conduction becomes the main mode of heat transfer within the borehole heat exchangers array, and heat transfer decreases.

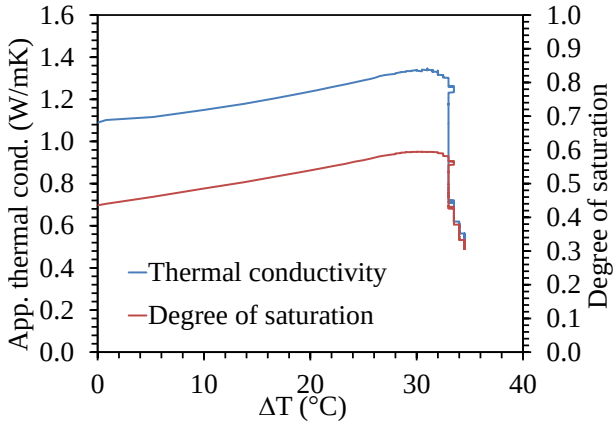

Figure 8.1 Apparent thermal conductivity and degree of saturation as a function of the change in during Test 1

The thermal conductivity and degree of saturation in Tests 2 and 3 follow the same simultaneous increase as in Figure 8.1 but a decrease is not observed. This may be due to the presence of water within the array. Contrary to Test 1, the amount of water within the borehole heat exchangers array did not get drier than it initially was. The presence of the extra water permitted a slight sustained increase in thermal conductivity. These results show a clear relationship between degree of saturation and thermal conductivity.

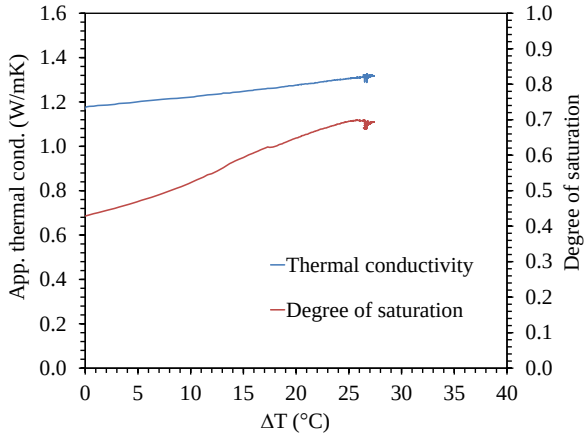

Figure 8.2 Apparent thermal conductivity and degree of saturation as a function of the change in during Test 2

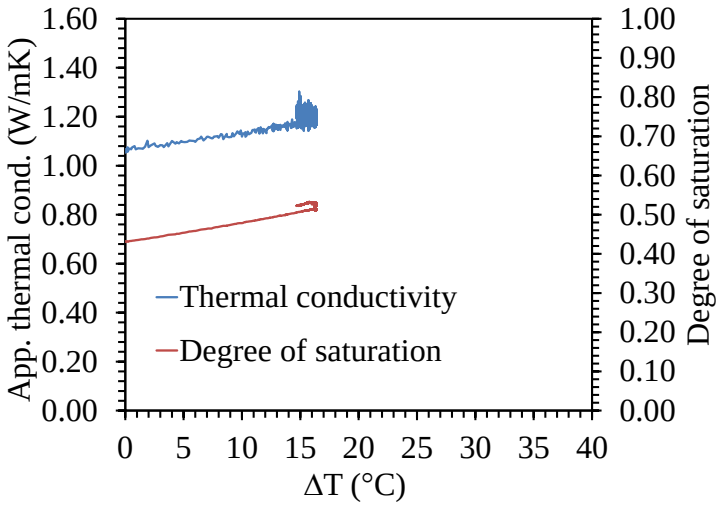

Figure 8.3 Apparent thermal conductivity and degree of saturation with temperature changes in Test 3

Plots of the thermal conductivity and specific heat as a function of the degree of saturation in Test 1, 2 and 3 are shown in Figures 8.4 and 8.5 and 8.6, respectively. The results for Test 1 indicate that the apparent thermal conductivity increases rapidly with saturation to a saturation value of approximately 0.6, and then declines on a different path as the soil gets dryer, similar to the drop-off with increasing change in temperature observed in Figure 8.1. The blue and red arrows represent the behavior of thermal conductivity and specific heat capacity, respectively during wetting and drying paths. Water within the closed-loop heat exchangers array may have vaporized and water flowed away from the array. The drying within the borehole heat exchanger array caused by this water movement was observed to lead to a decrease in thermal conductivity.

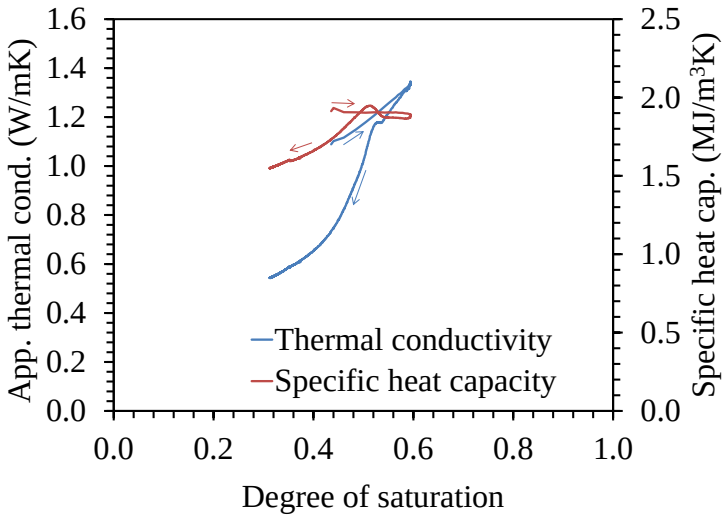

Figure 8.4 Thermal conductivity and specific heat capacity with degree of saturation in Test 1

Thermal conductivity and specific heat capacity both increase with increasing degree of saturation in Test 2. When the degree of saturation reaches a value of approximately 0.7, slight drying occurs. This drying causes thermal conductivity to increase slightly and specific heat capacity to decrease slightly. In Test 3, both specific heat capacity and thermal conductivity increase with the wetting of the unsaturated silt. When the degree of saturation reaches a steady

value of 0.53, they both still increase asymptotically. This indicates that a convective cell may have been formed, and heat transfer was enhanced.

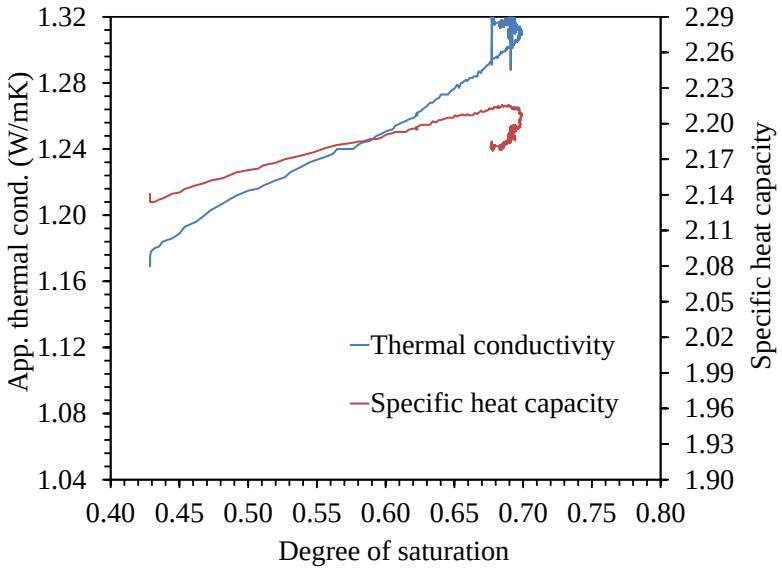

Figure 8.5 Thermal conductivity and specific heat capacity with degree of saturation in Test 2

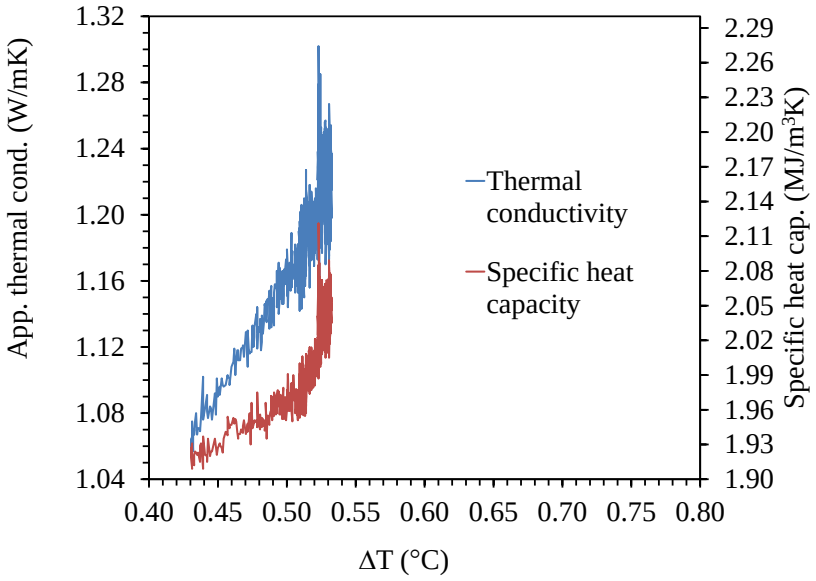

Figure 8.6 Thermal conductivity and specific heat capacity with degree of saturation in Test 3

The data from the thermocouple profile probes can also be used to calculate the changes in apparent thermal conductivity of the soil surrounding the borehole heat exchanger array. The thermal conductivity in the soil surrounding the heat exchanger array at steady state can be calculated as follows:

$$\lambda = \frac{\dot{Q}}{-2\pi R l \left[\frac{dT}{dr}\right]} \tag{8.1}$$

where λ (W m^{-1} K^{-1}) is the thermal conductivity, $\dot{Q}$ (W) is the energy transfer rate which can be calculated using Equation (7.4), l (m) is the total length of the borehole, R (m) is the radius of the borehole, and $\left[\frac{dT}{dr}\right]$ (K/m) is the temperature gradient. The term $2\pi Rl$ (m^2) is the surface area of the borehole over which heat is transferred. The distribution of temperature at different locations (110 mm, 160 mm, 210 mm and 260 mm) for Tests 1 is shown in Figure 8.7. The temperature distributions are relatively linear, and are sufficient to define the thermal gradient in the soil outside of the heat exchanger zone.

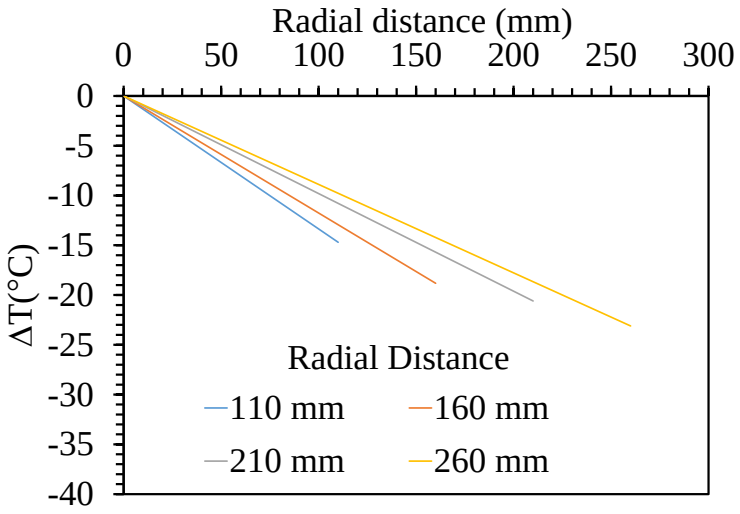

Figure 8.7 Test 1 thermal profile probes data: Temperatures at diferent radial locations

The thermal conductivity of the mass of soil outside of the heat exchanger array can be calculated using the overall slope of the data in Figure 8.7 and Equation (8.1). In this case, the overall thermal conductivity of the soil outside of the heat exchanger array can be compared with the overall thermal conductivity of the soil within the heat exchanger array, as shown in Figure 8.8. It is clear that the apparent thermal conductivity of the soil outside of the borehole heat exchanger array increased during the test, likely due to the gradual wetting of the soil surrounding the heat exchanger array for this particular spacing (80 mm).

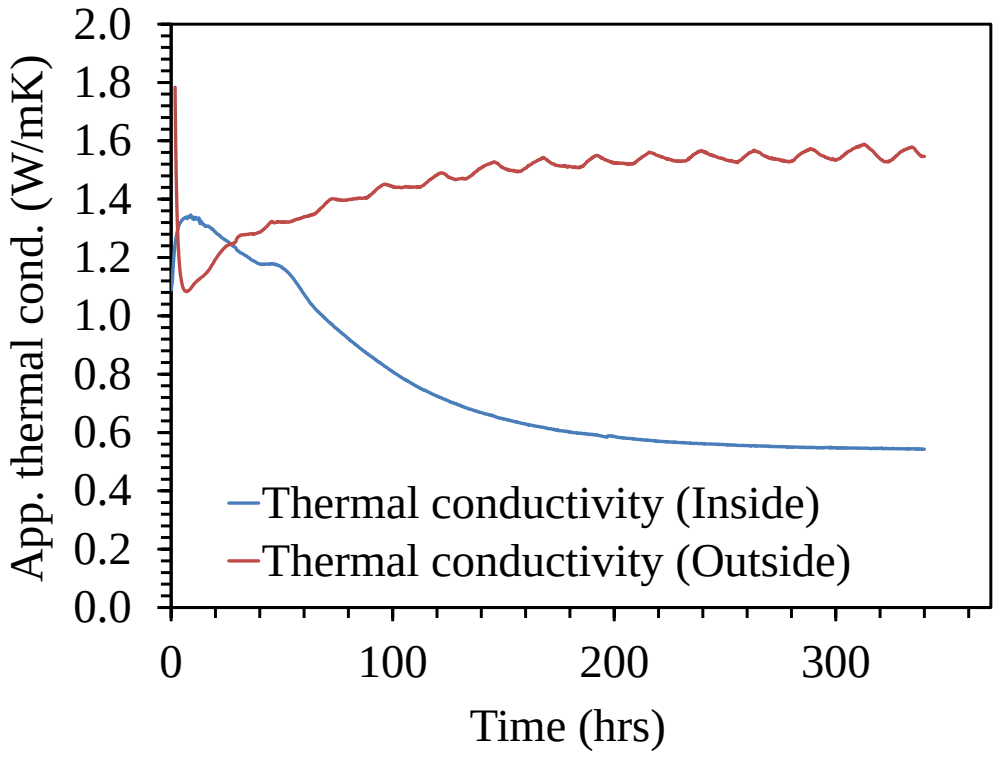

Figure 8.8 Thermal conductivity inside and outside the borehole array in Test 1

The formation of a convection cell was not observed within the closest spaced borehole-heat exchanger array. It was observed that as the spacing gets larger, formation of a convective cell appeared to be more promising. Moreover, results from the 5TE sensors presented in Chapter 7 suggest that there was an accumulation of water at the top of the unsaturated silt layer and that that region had one of the lowest temperatures. However, no evidence of downward water flow due to

gravity was observed in these tests. The use of a geotechnical centrifuge may help to better capture the role of capillary rise and downward liquid water flow on the coupled heat transfer and water flow process.

8.2 Role of Array Spacing

The thermal conductivity was not measured in Test 4 (array spacing of 150 mm) due to a defective data logger. However, knowing that the thermal conductivity varies with the degree of saturation, the water flow monitored with the 5TE sensors still provides important information. A plot of the degree of saturation with borehole heat exchanger spacing is shown in Figure 8.9.

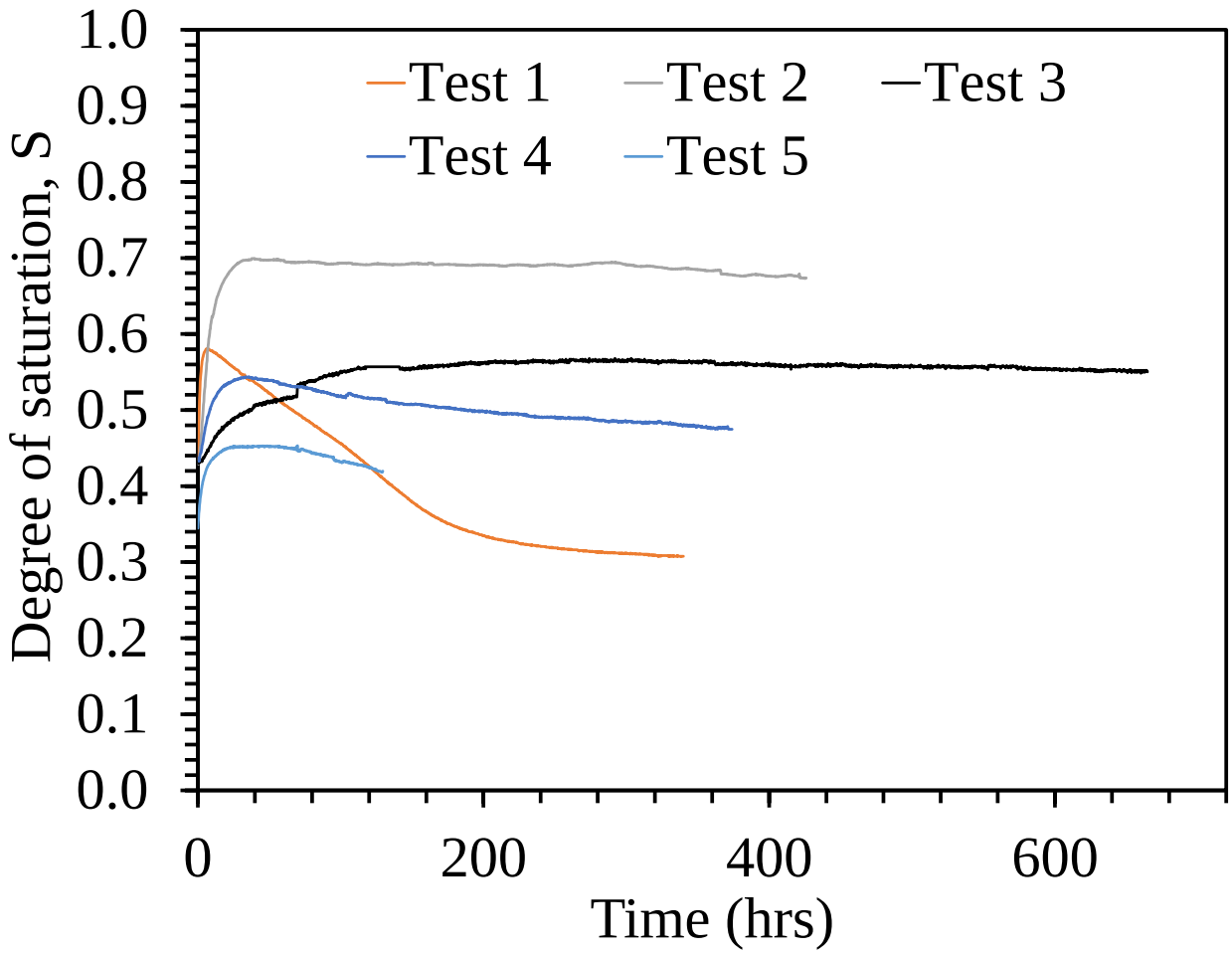

Figure 8.9 Dielectric sensors time series: Degree of saturation with variations in borehole heat exchangers spacing

As shown in Chapter 7, an initial increase in degree of saturation followed by a steady decline was observed in all tests, although the rate of decrease in degree of saturation seems to depend on the spacing of the borehole array. The permanent drying was occurring but at a much slower rate for larger spacing. However, results from Test 1 (array spacing of 80 mm) indicate that within the borehole heat exchangers array, a brief wetting occurs followed by a sudden drying of the soil. The zone of influence of the heat exchanger pipes may have taken up all the space within the array, making it nearly as hot as the heat source. Water was then permanently vaporized within the array and flowed through capillarity to a cooler region. Volumetric water content measurements taken after the test was completed showed the presence of wetter soil around the sides of the container and around the top of the vadose zone. This is evidence that water migrated from the heat source to colder regions where it condensed. It was concluded that this spacing may be too small to induce a convective cell within the array.

Test 5, which had slightly higher array spacing (100 mm) was inconclusive due to the duration of the test. It showed the initial increase in thermal conductivity with saturation but the lack of data made it impossible to observe the behavior of thermal conductivity at later times. Results from the 5TE sensors however indicated that rapid wetting then permanent drying occurred in the same way seen in Test 1. Test 3 which had the highest array spacing (300 mm) showed that the degree of saturation increased until it reached a relatively steady value. It was observed that thermal conductivity was still increasing even with a steady degree of saturation. This implies that a convective cell may have been formed within the array, with enough water to enhance the thermal conductivity.

8.3 Quantification of Heat Transfer

The energy transfer during the course of the experiment was determined using the inlet and outlet temperatures. The amounts of energy transferred in to the silt over time for Tests 1, 2, 3 and 4 are presented in Figure 8.10. Test 5 did not have the inlet and outlet temperature thermocouples, therefore energy input could not be estimated. In all tests, the amount of energy transfer initially has a high value as the temperature gradient is very high, then drops over time as the temperature within the array increases, then becomes relatively constant after approximately 30 hours. These results indicate that for borehole arrays with wider spacings, more energy is transferred to the silt.

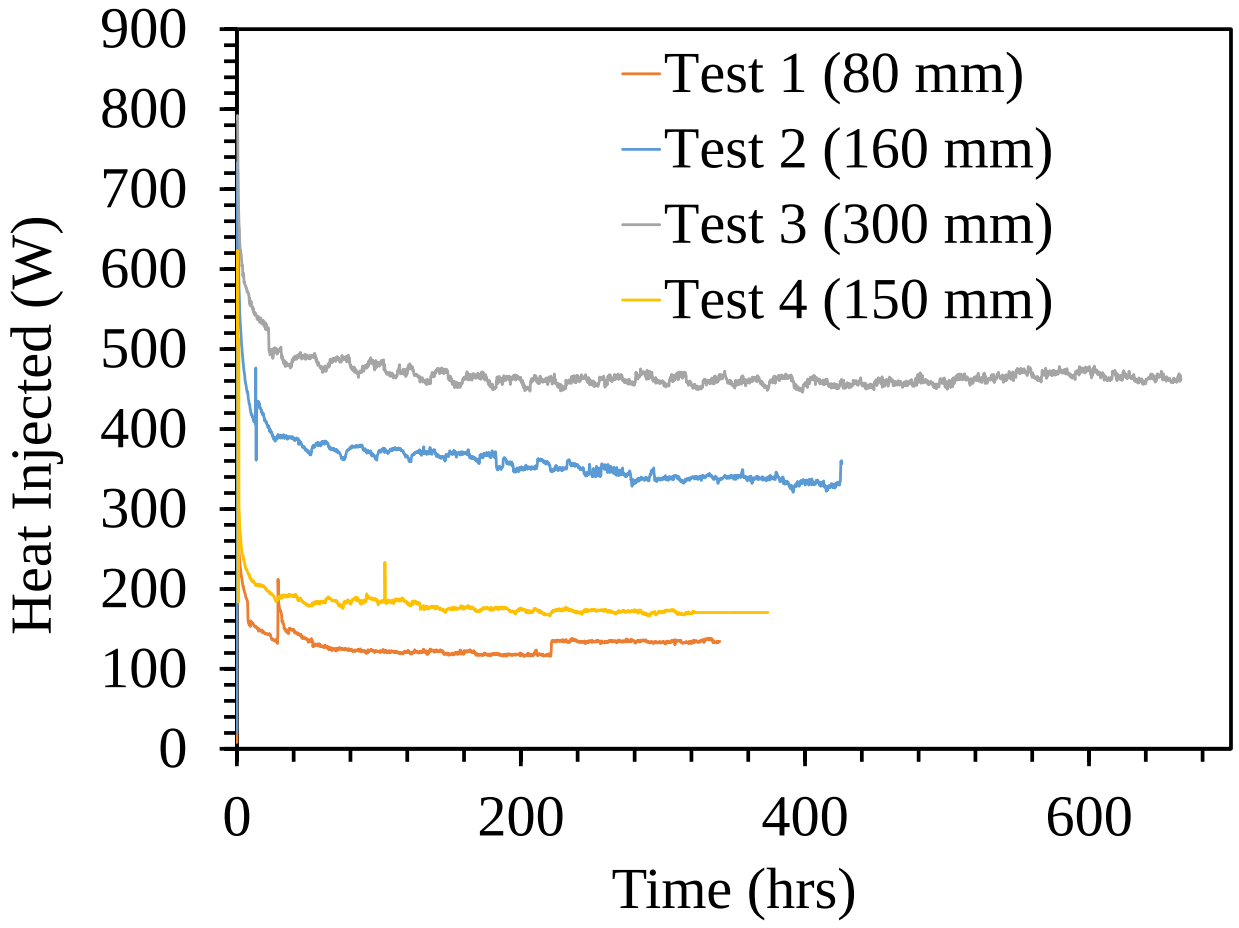

Figure 8.10 Total energy transferred for Tests 1, 2, 3 and 4

The maximum energy stored in the unsaturated silt layer was calculated as follows:

$$q = V\rho c_p dt \tag{8.2}$$

where C (m^3) is the total volume of the soil. This equation can be broken down to account for the heat storage capacities of the water, air and solids, as follows:

$$q = V_w\rho_w c_w + V_a\rho_a c_a + V_s\rho_s c_s \tag{8.3}$$

where q is the heat storage is in kJ/K, V_w (kg/m^3), V_a (kg/m^3) and V_s(kg/m^3) are the volumes of water, air and solids, respectively, c_w (kJ m^3 K^{-1}), c_a (kJ m^3 K^{-1})and c_s (kJ m^3 K^{-1}), are the specific heat capacities if water, air and solids, respectively, and ρ_w (kg/m3), ρ_a (kg/m3) and ρ_s (kg/m3) are the densities of water, air, and solids, respectively. The volumes were determined using the soil phase diagram. Table 8.1 presents the possible contributions of each phase to the energy storage. The highest specific heat capacity for the silt was observed in Test 3 (spacing of 300 mm), therefore its value was used in this calculation.

Table 8.1 Heat storage contributions from water, air and silt in Test 3

	Volume (m^3)	Volumetric heat capacity (kJ/m^3K)	Available heat storage (MJ/K)
Water	0.020	4183000	2954
Air	0.045	1.152	0.002
Silt	0.074	3581200	9104
Total available heat storage (kJ/K)			12058

The actual heat storage within each soil layer was estimated as follows:

$$q = \dot{q}t \tag{8.4}$$

where $\dot{q}$ (W or J/s) is the average heat transfer rate obtained from the inlet and outlet fluid temperatures, and t (s) is the duration of the experiment. The energy loss was estimated for the tests by calculating the thermal gradient between the soil at the inside boundary the container and

the ambient temperature of the laboratory at steady state, and multiplying it by the thermal conductivity of the aluminum container as follows:

$$q_{lost} = \lambda_{aluminum} \nabla T \tag{8.5}$$

where $\lambda_{aluminum}$ (W/(mK)) is the thermal conductivity of aluminum and ∇T is the temperature gradient between the soil inside the container and the ambient temperature.

$$\nabla T = \frac{dT}{\delta} \tag{8.6}$$

where, δ is the thickness of the aluminum insulation. The energy stored is the difference between the total energy injected and the energy that was lost to the surroundings as shown in Equation 8.7.

$$q_{stored} = q_{injected} - q_{lost} \tag{8.7}$$

This calculation was performed only for Test 3 where the heat exchangers were at the boundary of the container. It is not entirely accurate as it is hard to quantify the amount of heat that was transferred in all directions in the soil. Furthermore for smaller spacings, it can be assumed that most of the injected energy dissipated in the soil and that the losses to the surroundings can be neglected. The energy transfer is expected to be significantly higher for larger spacing, where a convective cycle is allowed to form within the borehole heat exchangers array.

The amount of energy injected, lost and stored in Test 3 are shown in Figure 8.11. As shown in Chapter 7, it takes several hours for the volumetric water content within the borehole array to stabilize. However, the energy storage reaches a stable value after approximately 50 hours of heat storage, which corresponds to the maximum heat storage capacity of the soil. Even though the water content was observed to change throughout the test, the energy transfer and storage stabilized very quickly after the temperatures reached a steady value.

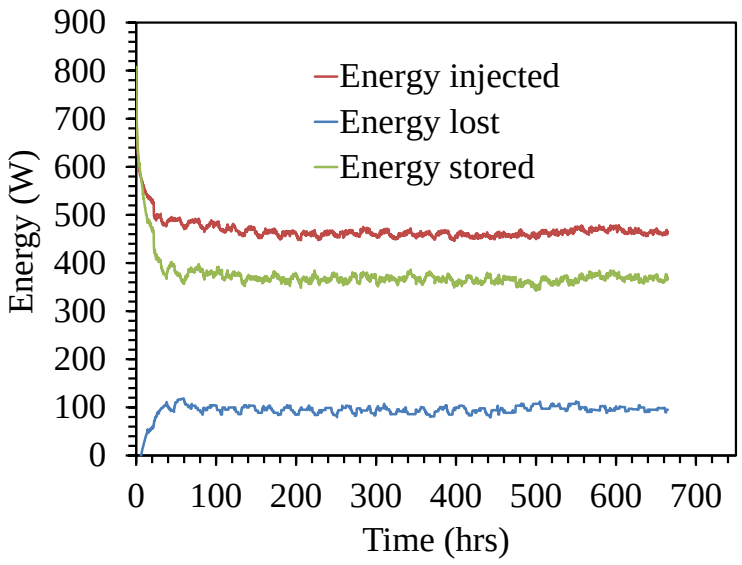

Figure 8.11 Energy transfer and storage over time in Test 3

The estimated heat storage over the course of the different tests is shown in Table 8.2. As expected, Test 3 has a significantly higher energy storage compared to the other tests as it had the largest volume of soil within the array. Future tests can evaluate the amount of the heat stored in the soil that can be subsequently extracted from the soil by circulating cold fluid through the heat exchangers. This can be used to define the efficiency of heat exchange in the borehole array.

Table 8.2 Summary of the estimated energy storage for all tests

	Spacing (mm)	Duration (hours)	Average power transfer (W)	Total Energy Injected (MJ)	Energy Lost (W)	Energy stored (W)
Test 1	80	435	132	207	-	207
Test 2	160	635	360	823	-	823
Test 3	300	715	469	1207	95	1112
Test 4	150	370	180	240	-	240
Test 5	100	-	-	-	-	-

9. CONCLUSIONS

A series of five tests were performed on unsaturated layers of Bonny silt underlain by a saturated layer of water-saturated Nevada sand. The unsaturated silt layer (i.e., the vadose zone) contained an array of three closed-loop heat exchangers with a different radial spacing in each test (80 mm, 160 mm, 300 mm, 150 mm and 100 mm). Water with a temperature of approximately 70 °C was circulated through the heat exchangers to inject heat into the unsaturated soil layer. Coupled heat and water flow was examined by monitoring the changes in volumetric water content, temperature, thermal conductivity, and specific heat within the vadose zone. The following conclusions were drawn from this study:

- For borehole arrays with a close spacing (80 mm and 100 mm), permanent and rapid drying was observed in the unsaturated soil within the borehole array. Water was observed to escape from the array laterally toward the sides of the container and upward toward soil surface. A convective cell is not formed within these array.
- For borehole arrays with a larger spacing of 150 mm and 160 mm, drying was also observed within the array. However, it occurred at a much slower rate. A convective cell was still not formed within these arrays.
- For the borehole array with the largest spacing of 300 mm (i.e., heat exchangers at the boundary of the cylindrical container), the soil within the soil layer was observed to increase in water content, indicating that a convective cell may have formed. In this array, heat was able to escape from the sides of the container, but water was not able to escape laterally.
- In the case of the arrays with spacings less than 300 mm, energy transfer into the array was observed to decrease over time as the soil dried. However, the same amount of heat was injected as the heat moved to the wetter soil outside of the array.

- Although water was observed to condense at the soil surface in all of the physical modeling experiments, the downward flow of liquid water due to gravity was not observed to be significant compared to the rate of upward vapor flow. Longer testing times may have revealed this phenomenon. A recommendation from this study would be to use a geotechnical centrifuge to better capture the role of capillary rise and downward liquid water flow on the coupled heat transfer and water flow process.
- The thermal conductivity measured using the SH-1 sensor was observed to increase significantly during the heating process, and was observed to be a function of both the degree of saturation of the soil and the temperature. Similar behavior was noted in all of the experiments.
- The heat storage in the soil layer defined as the difference between heat injection and heat loss away from the borehole array was observed to be the greatest in the array with the greatest spacing, both because there was the largest zone of soil within the array and because the soil experienced the greatest increase in water content within the area during heating.

References

Aiban, S.A. and Znidarcic, D., 1989. "Evaluation of the flow pump and constant head techniques for permeability measurements." Geotechnique 39, pp. 655-666.

Brandl, H., 2006. "Energy foundations and other thermo-active ground structures." Geotechnique 56 (2), 81–122.

Brandon, T.L. and Mitchell, J.K., 1989. "Factors influencing thermal resistivity of sand." Journal of Geotechnical Engineering, 115, 1683-1698.

Burdine, N.T. 1953. "Relative permeability calculations from pore-size distribution data." Petroleum Transactions of the American Institute of Mining and Metallurgical Engineering. 198, 71-77.

Campbell, G.S., J.D. Jungbauer, W.R. Bidlake, and R.D. Hungerford. 1994. "Predicting the effect of temperature on soil thermal conductivity." Soil Sci. 158,307–313.

Carslaw, H.S. and Jaeger, J.C., 1959. Conduction of Heat in Solids, 2nd Edition. Oxford, London.

Cass, A., Campbell, G. S., and Jones, T. L., 1984. "Enhancement of thermal water vapor diffusion in soil." Soil Science Society of America Journal, 48, 25-32.

Childs, E.C. and Collis-George. N. 1950. "The permeability of porous materials." Proc. Roy. Soc. London. A:201, 392-405.

Coccia, C.J.R. and McCartney, J.S. 2012. "A thermo-hydro-mechanical true triaxial cell for evaluation of the impact of anisotropy on thermally-induced volume changes in soils." ASTM Geotechnical Testing Journal. 35(2), 11 pg.

COMSOL. 2008. COMSOL Multiphysics Reference Guide. Version 3.5a

Dell'Avanzi, E., Zornberg, J.G., and Cabral, A.R. 2004. "Suction profiles and scale factors for unsaturated flow under increased gravitational field." Soils and Foundations. 44(3), 1-11.

deVries, D.A. 1960. Heat Transfer in Soils. Eindhoven University of Technology, The Netherlands.

deVries, D.A., 1958. "Simultaneous transfer of heat and moisture in porous media", Trans Am Geophys Union, vol.39, p.909-916

Duarte, A.P.L., de Campos, T.M.P, Araruna Jr, J.T. and Filho, P.R., 2006, "Thermal properties of unsaturated soils. Proceedings UNSAT 2006. Carefree, Arizona. 10 pg.

Farouki, O.T., 1981. Thermal Properties of Soils. Cold Regions Science and Engineering, CRREL Monograpg 81-1, 136.

Flynn, D.R. and T.W. Watson, 1969. Measurements of the Thermal Conductivity of Soils to High Temperatures. Sandia Laboratory Final Report (SC-CR-69·3059). Albuquerque

Goode, J.C. III 2012. Centrifuge Modeling of the Thermo-Mechanical Response of Energy Foundations. MS Thesis. University of Colorado Boulder.

Heitman J. and Horton R. 2011. Coupled Heat and Water Transfer in Soil. In: Glinski J., Horabik J., Lipiec J. (Ed.) Encyclopedia of Agrophysics: SpringerReference. Springer-Verlag Berlin Heidelberg, 2011. DOI: 10.1007/SpringerReference_329982 2012-05-23 11:42:58 UTC

Heitman, J. L., Horton, R., Ren, T., Nassar, I. N., and Davis, D., 2008a. "Test of coupled soil heat and water transfer prediction under transient boundary conditions." Soil Science Society of America Journal, 72, 1197-1207.

Hermanson, A., Charlier, R., Collin, F., Erlingsson,S., Srsen, M., Laloui, L. 2008. Water in Road Structures Movement, Drainage and Effects. Nottingham Transportation Engineering Centre, University of Nottingham, UK, Springer ed., p69-79

Hopmans, J.W. and J.H. Dane. 1986. "Thermal conductivity of two porous media as a function of water content, temperature and density." Soil Sci. 142,187–195. International Journal of Heat and Mass Transfer, Vol. 25, pp. 1605–1606.

Jahangir, M.H. and Sadmejad, S.A. 2012. "A new coupled heat, moisture and air transfer model in unsaturated soil." Journal of Mechanical Science and Technology. Department of Civil Engineering, Khaje Nasirodin Toosi University of Technology, Tehran, Iran.

Khaleel, R. Relyea, J.F., and Conca, J.L. 1995. "Evaluation of van Genuchten-Mualem relationships to estimate unsaturated hydraulic conductivity at low water contents." Water Resources Research. 31(11)2659-2668.

Khosravi, A. 2011. Small Strain Shear Modulus of Unsaturated, Compacted Soils During Hydraulic Hysteresis. PhD. Thesis. University of Colorado Boulder.

Khosravi, A., Alsherif, N., Lynch, C., and McCartney, J.S. (2012). "Use of multistage triaxial testing to define effective stress relationships for unsaturated soils." ASTM Geotechnical Testing Journal. 35(1), 10 pg.

Kluitenberg, G.J., Ham, J.M., and Bristow, K.L., 1993. "Error analysis of the heat pulse method for measuring soil volumetric heat capacity." Soil Sci. Soc. Am. J. 57, 1444-1451.

Marquardt, D.W., 1963. "An algorithm for least squares estimation of nonlinear parameters." Journal of the Society of Industrial and Applied Mathematics. 11, 431-441.

McCartney, J.S. 2007. Determination of the Hydraulic Properties of Unsaturated Soils in a Centrifuge Permeameter. PhD Thesis. University of Texas at Austin.

McCartney, J.S., Ge, S., Reed, A., Lu, N., and Smits, K. 2013a. "Soil-borehole thermal energy storage systems for district heating." European Geothermal Congress 2013, Pisa, Italy, June 3-7, 2013. 10 pg.

McCartney, J.S., Jensen, E., and Counts, B., 2013b. "Measurement of subgrade thermal conductivity using a modified triaxial test." TRB 92nd Annual Meeting, January 13-17, Washington D.C., USA.

Murphy, K.D., McCartney, J.S, and Henry, K.S. 2014. “Impact of horizontal run-out length on the thermal response of full-scale energy foundations. GeoCongress 2014. Atlanta, GA, 10 pg.

Murphy, K.D. 2013. Thermal and Thermo-mechanical Behavior of Full Scale Energy Foundations. M.S. Thesis. University of Colorado Boulder.

Nassar, I. N. and Horton, R., 1997. “Heat, water, and solute transfer in unsaturated porous media: I. Theory development and transport coefficient evaluation.” Transport in Porous Media, 27, 17-38.

Nield, D.A. 1982. “Onset of convection in a porous layer saturated by an ideal gas.”, Int. J. Heat Mass Transfer, 25, 1605–1606

Philip, J.R. and deVries, D.A. 1957. “Moisture movement in porous material under temperature gradients.” American Geophysical Union Transactions. Vol 38, Issue 2.

Pruess, K. 1991. TOUGH2: A General-purpose Numerical Simulator for Multiphase Fluid and Heat Flow. Lawrence Berkeley Laboratory, LBL-29400, Berkeley, CA.

Pruess, K., Oldenburg, C. and Moridis, G. 1999. TOUGH2 User’s Guide, Version 2.0. Lawrence Berkeley National Laboratory Report LBNL-43134, Berkeley, CA.

Sakaguchi, I., Momose, T., and Kasubuchi, T., 2007. “Decrease in thermal conductivity with increasing temperature in nearly dry sandy soil.” Eur. J. Soil Sci. 58:92–97. doi:10.1111/j.1365-2389.2006.00803.x

Salomone, L.A., Kovacs, W.D., and Kusuda, T., 1984. “Thermal performance of fine-grained soils. Journal of Geotechnical Engineering.” Vol. 110 (3), 359-374.

Sibbitt, B., Onno, T., McClenahan, D., Thornton, J., Brunger, J., Wong, B. 2007. “The Drake Landing solar community project – early results.” Canadian Solar Buildings Conference, Calgary, June 10-14.

Smits, K.M., Sakaki, S.T., Howington, S.E., Peters, J.F., and Illangasekare, T.H. 2012. "Temperature dependence of thermal properties of sands across a wide range of temperatures (30-70 °C)." Vadose Zone Journal, doi: 10.2136/vzj2012.0033.

Smits, K.M., Sakaki, S.T., Howington, S.E., Peters, J.F., and Illangasekare, T.H. 2010. "Thermal conductivity of sands under varying moisture and porosity in drainage–wetting cycles." Vadose Zone Journal 9:1-9, doi: 10.2136/vzj2009.0095.

Stewart, M.E. 2012. Centrifuge Modeling of Strain Distributions in Energy Foundations. MS Thesis. University of Colorado Boulder.

Vega, A. 2012. Impact of Temperature Cycles on the Thermal Consolidation of Silt Under Different Stress States. MS Thesis. University of Colorado Boulder.

Smith, W.O. 1943. Thermal transfer of moisture in soils, Trans. Am. Geophys, Union 24 pg 511-523

Woodside, W. and Kuzmak, J.M. 1958. Effect of temperature distribution on moisture flow in porous materials, Trans. Am. Geophys, Union 39 676-680.

Zhang, R., Lu, N., and Wu, Y-S. (2012). "Efficiency of a community-scale borehole thermal energy storage technique for solar thermal energy." In Proceedings of ASCE Geo-Institute Annual Conference, Oakland, CA.